IA - 1486



# RESEARCH LABORATORIES ANNUAL REPORT 1993

Israel Atomic Energy Commission

# FOREWORD

I am pleased to introduce the 1993 Annual Report of the Israel Atomic Energy Commission. Like its predecessors in the long, uninterrupted series of reports begun in 1960, the report presents, in a brief and concise form, recent results and achievements of the well established program of basic and applied research carried out by the scientists and engineers of the IAEC often in collaboration with colleagues at other institutions in Israel and abroad.

In terms of contents, the report presents the usual combination of topical basic and applied research. Like in previous years, much of the work has been published or submitted for publication in international scientific or technical literature.

I would like to use this opportunity to congratulate the staff of the IAEC Research Laboratories on their efforts and wish them another fruitful and productive year.

August 1994.

Gideon Frank
G. Frank
Director General
Israel AEC

# CONTENTS


| | | |
|---|---|---|
| I | THEORETICAL PHYSICS AND THEORETICAL CHEMISTRY | 1 |
| II | OPTICS AND LASERS | 15 |
| III | SOLID STATE AND NUCLEAR PHYSICS | 45 |
| IV | MATERIALS SCIENCES | 65 |
| V | CHEMISTRY | 91 |
| VI | ENVIRONMENTAL STUDIES AND RADIOPHARMACEUTICALS | 107 |
| VII | RADIATION EFFECTS, DOSIMETRY AND PROTECTION | 121 |
| VIII | INSTRUMENTATION AND TECHNIQUES | 143 |
| IX | DOCUMENTATION | 163 |
| X | AUTHOR INDEX | 201 |


# I

# THEORETICAL PHYSICS AND THEORETICAL CHEMISTRY

## Computation of Droplets Distribution in Nozzle and Plume Flows[1]

L. Genkin, M. Baer and J. Falcovitz*

A simple entertainment model is used to estimate droplet streamlines, velocity and mass flux in rocket exhaust plumes. Since droplets mass flux constitutes only about 1% of the exhaust mass flux, the effect of droplets entrainment on the gas flow is neglected. Distribution within the nozzle is obtained by assuming a small random velocity component for droplets at the throat, their average velocity being evaluated from uniaxial acceleration. Gas flow in the nozzle is approximated as supersonic plus a correction for the boundary layer. The computed distribution of droplet mass flux was found to be in good agreement with experimental data obtained by Hoffman *et al.*[2].

*References*

[1] L. Genkin, M. Baer and J. Falcovitz, *Am. Inst. Aeronaut. Astronaut. J.* (1994, in press).

[2] R.J. Hoffman, A. Kawanaki, A. Trinks, I. Bindemann and W. Ewering, *AIAA 20th Thermophysics Conf.* (Williamsburg, VA, USA, June 1985), paper 85-0928.

## Three-Dimensional Quantum Mechanical Study of Exothermic Reactive Systems ($F+H_2$; $Ar+H_2^+$) Employing Negative Imaginary Arrangement Decoupling Potentials[1]§

M. Gilibert**, I. Last, A. Baram and M. Baer

In this work we consider two highly exothermic systems: $F+H_2(v=0,j)\rightarrow HF(v,j')+H$ and $Ar+H_2^+(v=0,j)\rightarrow AH^+(v',j')+H$. Reactive probabilities were calculated for J=0 only. The main findings are as follows:

- The $F+H_2$ system is characterized by forming products with inverted vibrational distribution. In the case of $Ar+H_2^+$, the production vibrational distribution is even.
- The initial rotational quantum number j has a strong effect on the reactivity of the reactions; in both cases the reaction probabilities drop significantly as j increases.

*Reference*

[1] M. Gilibert, I. Last and M. Baer, Submitted to *Chem. Phys. Lett.*

---

*Technion–Israel Institute of Technology, Haifa.

§This work was supported by the German-Israel Foundation (GIF) and by a grant (BE92/285) from the regional Catalonian Government (CIRIT), Spain.

**Dept. of Physical Chemistry, University of Barcelona, Barcelona, Spain.

## Quantum Mechanical Cross Sections for the $D+H_2$ and $H+D_2$ Reactive Systems: Application of the Negative Imaginary Potentials within the $j_z$ Approximation[1]§

A. Baram, I. Last and M. Baer

We considered a new quantum mechanical approximation to calculate atom-diatom exchange state-to-state cross sections. The method is based on the coupling of the $j_z$ approximation with negative imaginary potentials (NIPs). The NIPs produce absorbing boundary conditions which permit the application of $L^2$ basis sets expressed in terms of Jacobi coordinates of a single arrangement channel. The method is applied to two systems, namely, the $D+H_2 \rightarrow HD+H$ and $H+D_2 \rightarrow HD+D$ reactions. Good agreement with exact quantum mechanical integral cross sections was obtained.

*Reference*

[1] A. Baram, I. Last and M. Baer, *Chem. Phys. Lett.* 212: 649 (1993).

## Integral and Differential Cross Sections for the $Li+HF \rightarrow LiF+H$ Process: A Comparison between $j_z$ Quantum Mechanical and Experimental Results[1]

M. Baer, H.J. Loesch*, H.J. Werner** and I. Last

We conducted a detailed quantum mechanical study of the $Li+HF(v=0,j) \rightarrow LiF(v',j')+H$ reaction in the low energy region $0.001 \leq E_{tr} \leq 0.15$ eV. The theoretical–numerical treatment was carried out within the inelastic $j_z$ approximation coupled with negative imaginary potentials (to form absorbing boundary conditions) to account for the reactivity of the system. Integral and differential state-to-stage cross sections were calculated and compared with experiment and other calculations. As for the experiments, *(a)* the theoretical treatment approximately reproduced the laboratory measured differential cross sections and *(b)* they produced integral cross sections in the range $0.30 \leq \sigma \leq 0.65$ Å$^2$ which overlap rather well with the measured value (at $E_{tr} = 0.13$ eV) of $\sigma = 0.6 \pm 0.30$Å$^2$.

*Reference*

[1] M. Baer, H.J. Loesch, H.J. Werner and I. Last, *Phys. Lett.* (1994, in press).

---

§This work was supported by the U.S.-Israel Binational Science Foundation and the Israel Academy of Sciences and Humanities, Jerusalem.

*Dept. of Physics and **Dept. of Chemistry, Bielefeld University, Bielefeld, Germany.

## Application of Toeplitz Matrices to Scattering Problems[1]

M. Gilibert*, A. Baram, I. Last, H. Szichman and M. Baer

This work describes a new approach to treating quantum mechanical scattering problems. It is based on expanding the wave function in terms of an infinite set of localized Gaussian functions and employing the features of a Toeplitz matrix.

*Reference*

[1] M. Gilibert, A. Baram, I. Last, H. Szichman and M. Baer, *J. Chem. Phys.* 99: 3503 (1993).

## Three-Dimensional Study of Reactive Diatom-Diatom Systems: Quantum Mechanical State-to-State Cross Sections for the $H_2+OX \rightarrow H+XOH$; X=H,D Reactions[1]§

H. Szichman, I. Last and M. Baer

A detailed quantum mechanical study was made of the three-dimensional tetra-atom systems: $H_2(\upsilon_H)+OX(\upsilon_o) \rightarrow XOH(v',j,v) + H$; X = H,D. The study was limited to the case where the overall final rotational state K, of the product XOH molecules, is zero. The calculations were carried out using the negative imaginary arrangement decoupling potentials. The quasi-breathing-sphere approximation was employed for the reagents arrangement and the $j_z$ approximation for the products arrangements. State-to-state and state-selected cross sections were calculated for the (translational) energy range (0.1 – 0.7 eV).

*Reference*

[1] H. Szichman, I. Last and M. Baer, *J. Phys. Chem.* 98: 828 (1994).

*Dept. of Physical Chemistry, University of Barcelona, Barcelona, Spain.

§This work was supported by the U.S.-Israel Binational Science Foundation and the Israel Academy of Sciences and Humanities, Jerusalem.

# Applications of Square Integrable Basis Functions for Scattering Problems: A Comparison between Approaches Based on Toeplitz Matrices and Negative Imaginary Potentials[1]

S. Ron, E. Eisenberg, M. Gilibert* and M. Baer

Two quantum mechanical approaches to treat a single coordinate-Eckart-type-potential scattering process were considered (Fig. 1). One approach is based on the application of Toeplitz matrices and the other on the application of negative imaginary (absorbing) potentials (NIPs). It was found that for this type of 'reactive' process, the method based on the Toeplitz matrices performs better.

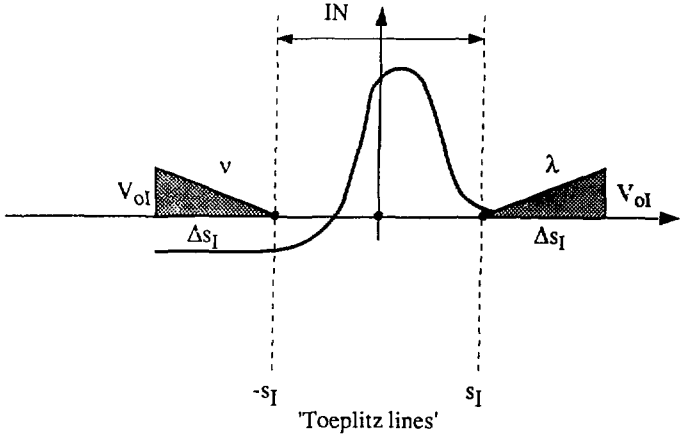


Fig. 1: The single coordinate reaction system. The two "Toeplitz lines" are border lines for the reagents (λ) region, the interaction (IN) region and the products (ν) region. Also shown are the two NIPs: one in the λ region and the other in the ν region.

*Reference*

[1] S. Ron, E. Eisenberg, M. Gilibert and M. Baer, *Phys. Rev.*, *A* (1994, in press).

*Dept. of Physical Chemistry, University of Barcelona, Barcelona, Spain.

## Three-Dimensional Reactive Quantum Mechanical Study for the $H+X_2$ (X=H,D,T) Systems: Application of Negative Imaginary Arrangement Decoupling Potentials[1]§

I. Last, A. Baram, H. Szichman and M. Baer

A three-dimensional quantum mechanical study was carried out of three hydrogenic reactions, namely, $H+X_2 \rightarrow HX + X$ (X = H,D,T) employing a newly developed approach based on negative imaginary arrangement decoupling potentials. Reactive vibrational-state selected cross sections were obtained from the accurate calculated $J = 0$ probabilities by employing a $J$ shifting procedure. The studied (total) energy interval was from threshold to 1.3 eV. Detailed comparisons were made with previous available quantum mechanical results and with quasi-classical trajectory results.

*Reference*

[1] I. Last, A. Baram, H. Szichman and M. Baer, *J. Phys. Chem.* 97: 7040 (1993).

## Onsager-Molecule Approach to Screening Potentials in Strongly Coupled Plasmas[1]

Y. Rosenfeld

The solution of the exact integral equation for the liquid pair-structure in the asymptotic strong coupling limit for the plasma, as mapped on the Onsager charge-smearing optimization for the energy lower bound, features 'Onsager atoms' and 'Onsager molecules'. The universal properties of this asymptotic limit make it a natural reference starting point for an asymptotic strong coupling expansion for the fluid structure and thermodynamics, playing the role of an 'ideal liquid' state. In particular, the leading strong coupling terms for the potential energy, direct correlation functions, and screening potentials for the Coulomb and Yukawa mixtures (corresponding to classical plasmas and electron-screened classical plasmas), with full thermodynamic consistency, are presented. These are in complete agreement with the Alastuey-Jancovici analysis of early simulations data by Hansen in strong coupling, and with recently highly accurate simulations data of Ogata, Iyetomi, and Ichimaru. Data analysis errors lead Ogata, Iyetomi, and Ichimaru to incorrect results for the short-range screening

§This work was supported by the U.S.-Israel Binational Science Foundation and the Israel Academy of Sciences and Humanities, Jerusalem, Israel; and by ITAMP at the Harvard Smithsonian Center for Astrophysics, Cambridge, MA, USA.

potentials in strong coupling. Their calculations for the short-range screening potentials, bridge functions, and enhancement factors for nuclear reaction rates in strongly coupled plasmas, should be revised.

*Reference*

[1] Y. Rosenfeld, *IAU Colloquium #147* (Saint Malo, France, June 1993). G. Chabrier and E. Schatzmann [Eds.] (Cambridge, UK: Cambridge University Press, 1994, in press).

## Adiabatic Pair Potential for Charged Particulates in Plasmas and Electrolytes[1]

Y. Rosenfeld

A treatment of the linear screening approximation for the adiabatic interaction between charged 'heavy' particles (particulates, macroions) is presented, which highlights the common points and the different points in its application to disparate physical systems like plasmas and colloidal suspensions.

*Reference*

[1] Y. Rosenfeld, *Phys. Rev., E* 43: (1994, in press).

## A Forced Bonhoeffer – van der Pol System in Its Excited Mode

A. Rabinovitch*, R. Thieberger and M. Friedman

The information passage through an axon can be modelled by a set of nonlinear differential equations. A simple approximation is a set of two equations, the Bonhoeffer – van de Pol system[1]. In this work this system was analyzed in the range of parameters where the attractor is a focus. The system's responses to a single pulse stimulus applied at different points along a 'hidden' structure are used to construct an ID map from which the system's responses to pulse train stimulations are obtained.

*Reference*

[1] S. Yasin, M. Friedman, S. Goshen, A. Rabinovitch and R. Thieberger, *J. Theor. Biol.* 160: 179 (1993).

*Ben-Gurion University of the Negev, Beer-Sheva.

## Simple Model of Biological Excitable Systems[1]

R. Thieberger, M. Friedman and A. Rabinovitch*

An effort was made to study nerve conduction. An important feature of such a system is its 'excitability': One perturbs the system at rest in the right direction (small input signal) and it will make a 'detour' before returning to the rest position. There are two possible outcomes of a simple pulse input: a large phase space loop (large output signal) and a small loop (for pulses below a minimal strength). There is a line (the separatrix) dividing between these two cases. A simple 'idealized model' has been used for the forced 'limit cycle' case[2], called a 'Poincare oscillator'. Such a simple model was developed here for a spiral approach to a focus in an excitable system.

A separatrix was defined and the time resetting curves were calculated. This model is applicable to the information passage in a squid giant axon.

*References*

[1] R. Thieberger, M. Friedman and A. Rabinovitch, *2nd Experimental Chaos Conference* (Arlington, VA, USA, Oct. 1993).

[2] L. Glass and M.C. Mackey, *From Clocks to Chaos.* (Princeton, NJ, USA: Princeton University Press, 1988).

## Critical Dynamics of the $d = 1$ Kinetic Ising Model[1]

B.W. Southern** and Y. Achiam

The critical dynamics of the $d = 1$ alternating bond Glauber-Ising model and related models was studied. There are two contributions to the critical slowing down. One is due to the long-range fluctuations near the critical point. It is characterized by the dynamic exponent $z = 2$. The other contribution is a temperature dependence of the bare time scale, which is a result of short-range phenomena. In contrast to previous studies, it was shown that all these models belong to one universality class.

*Reference*

[1] B.W. Southern and Y. Achiam, *J. Phys., A Math Gen.* 26: 2505 (1993).

*Ben-Gurion University of the Negev, Beer-Sheva.

**Dept. of Physics, University of Manitoba and Winnipeg Institute for Theoretical Physics, Winnipeg, Manitoba, Canada.

## Critical Dynamics and Universality in Kinetic Ising Models without Translational Invariance[1]

B.W. Southern* and Y. Achiam

The critical dynamics of the Glauber-Ising model on non-translationally invariant lattices was studied. Both a quasi-periodic and a fractal geometry were considered. The distribution of inverse relaxation times $\rho(1/\tau)$ was calculated using a generating function method. The distribution consists of bands with an internal self-similar structure. In the limit $1/\tau \to 0$, $\rho(1/\tau)$ diverges with a universal exponent related to the dynamic critical exponent $z$. The width of the lowest frequency band is determined by a non-universal bare time scale, which is related to the presence of metastable states.

*Reference*

[1] B.W. Southern and Y. Achiam, *J. Phys., A Math. Gen.* 26: 2519 (1993).

## Critical Dynamics of the Alternating Bond Kinetic Ising Model[1]

Y. Achiam and B.W. Southern*

The critical dynamics of the alternating bond kinetic Ising model on a chain was examined. It was shown that previous non-universal results for the dynamic critical exponent $z$ for single spin flip dynamics should be reinterpreted. The critical slowing down is due to two distinct contributions which, when separated, indicate that the value of $z$ is universal. The exponent remains universal even when two spin flip dynamics are considered.

*Reference*

[1] Y. Achiam and B.W. Southern, *J. Phys., A Math. Gen.* 25: L769 (1992).

*Dept. of Physics, University of Manitoba and Winnipeg Institute for Theoretical Physics, Winnipeg, Manitoba, Canada

## Stresses in Mixture Theory[1]

E. Taragan

Mixture theory is the branch in continuum mechanics that describes the mechanics of diffusion. In this work we present the mixture theory and the existence of stresses on the basis of the geometrical approach. This approach is based on a general definition of a force in continuum mechanics as a linear function on the space of virtual displacement of a body.

An attempt was made to formalize Truesdell's third principle and the notion of total stress. Total stress seems to have meaning only in some limited cases. For example, if we have a vessel filled with a mixture of gases, we expect the traction on the walls to be that induced by the sum of the partial stress. However, if some of the gases can diffuse through the walls of the vessel, the traction on the walls will be different from that induced by the 'total stress'.

In this work, rather than assuming that the mixture behaves as a simple body, we introduced a simple body model of a mixture and a model function that relates the configuration of the mixture to that of the model.

*Reference*

[1] E. Taragan, M.Sc. thesis, Ben-Gurion University of the Negev, Beer-Sheva (1992).

## Large-Scale Periodicity: A Generic Consequence of Adiabatic Gravitational Clumping[1]

R. Zamir

It was shown that small, adiabatically time-varying perturbations imposed on an homogeneous background generically create an oscillatory structure of voids and overdense spherical shells. The length-scale of these perturbations was found to be consistent with the $\sim 128\ h^{-1}$ Mpc period recently reported. The evolution of such an oscillatory structure in an expanding universe was considered, and it was shown that overdense shells contract whereas voids expand, so that if the overdense regions are ~ 5 Mpc wide, then the voids must be of the order of ~ 100 Mpc, and *vice versa*. If such a model is to be trusted, then the formation epoch of this large-scale structure is much later than recombination time. Thus, no contradiction with the observed homogeneity and isotropy of the microwave background radiation arises.

*Reference*

[1] R. Zamir, Submitted to *J. Phys., A*.

## Theoretical Studies of Surface Diffusion and Photo-Induced Surface Processes[1]

Y. Zeiri

The results of theoretical calculation associated with three different types of processes in an adsorbate–substrate system were considered. The goal in the first study is to shed light on the mechanism of surface diffusion of large adsorbates. The conventional random-walk-type motion along the surface, associated with small adsorbates, has to be largely modified when the description of the motion of large adsorbates is desired. The results of these calculations show good qualitative agreement when compared with experimental data. In the second study, the branching ratio between desorption and dissociation for large model adsorbates on a laser-heated substrate was examined. This quantity was found to be very sensitive to the adsorbate size, its adsorption geometry and the relative strength of the adsorbate-surface bond and the intramolecular bond which is broken during the dissociation process. The last group of calculations was aimed at investigating the dynamics associated with photodissociation products and its relation to the orientation and alignment of the adsorbates on the solid surface. The calculations were carried out for the HBr/LiF (001) system. The results show a marked dependence of the photoreaction probability as well as the angular and energy distributions of the scattered photofragment on the initial alignment of the adsorbate. In addition, the quantum nature of the H photoproduct was examined by a 2-D model quantum mechanical method. It was shown that for some systems the angular distribution of the scattered H-atom may exhibit a complicated diffraction pattern which can be related to the structure of the interface between the adsorbate layer and the substrate.

*Reference*

[1] Y. Zeiri, *Comput. Phys. Commun.* 80: 200 (1994).

## Molecular Dynamics Study of the Surface Diffusion of Large Adsorbates: III. Role of Adsorbate Shape[1]

Y. Zeiri

An investigation was conducted of the relationship between the surface diffusion mechanism of large adsorbates and the adsorbate shape. Three different shapes of model adsorbates were examined: linear chains, branched chains and cyclic molecules. The surface diffusion mechanism of linear and branched chain adsorbates was found to be quite similar,

while a markedly different diffusion mechanism was observed for cyclic adsorbates. For all types of adsorbates, the temperature dependence of the diffusion coefficient was found to obey an Arrhenius expression. The results of the simulations showed good qualitative agreement with the available experimental data.

*Reference*

[1] Y. Zeiri, *Can. J. Chem.* 72: (1994, in press).

## Radiation Transport and Coherence in Amplifying Refractive Systems[1]

G. Hazak and O. Zahavi*

A statistical-wave theoretical derivation of the radiative transfer equation for systems of stochastic radiators distributed in an amplifying refractive medium was developed. The connection between the specific intensity and the degree of spatial coherence in these systems was analyzed.

*Reference*

[1] G. Hazak and O. Zahavi, Submitted to *J. Opt. Soc. Am.*

## Study of Amplified Spontaneous Emission Systems by the Ray-Tracing Technique[1]

O. Zahavi*, G. Hazak and Z. Zinamon*

An implementation of the ray-tracing method for the study of radiation properties, such as intensity and spatial coherence, of an amplified spontaneous emission system was developed. Simple relations that express the controlling effect of the refraction on the output radiation properties are derived. We use analytical expressions, along with detailed numerical calculations, to analyze the intensity and the spatial coherence of the output radiation measured in X-ray laser experiments.

*Reference*

[1] O. Zahavi, G. Hazak and Z. Zinamon, *J. Opt. Soc. Am., B: Opt. Phys.* 10: 271 (1993).

---

*Weizmann Institute of Science, Rehovot.

## Generalized Van Cittert Zernike Theorem in Curved Spacetime[1]

G. Hazak and R. Zamir

A generalized form of the *Van Cittert Zernike* theorem which gives a simple relation between the measured coherence of the radiation and the characteristics of the emitting correlated source in curved spacetime is derived. The theorem is applied to the study of distortions in the measured spectrum of a quasar upon propagation through a gravitational lens.

*Reference*

[1] G. Hazak and R. Zamir, Submitted to *Astrophys. J.*

## The Wolf Effect in Spherically Symmetric Systems[1]

G. Hazak and R. Zamir

Explicit solutions for the cross-spectral density, the spectrum and the flux emitted by a partially coherent isotropically distributed primary source are derived. It was shown that the modification of the spectrum (Wolf effect) in the isotropic case is not due to radiation propagation, but rather to the emission mechanism itself. Consequently, the radiated spectrum *everywhere* is different from the spectrum of the source.

*Reference*

[1] G. Hazak and R. Zamir, *J. Mod. Opt.* (1994, in press).

# II

# OPTICS AND LASERS

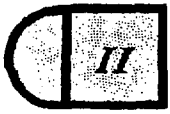

# Very High Efficiency of Frequency Doubling in QPM Waveguides of KTP[1]

D. Eger, M. Oron, M. Katz and A. Zussman

Frequency doubling of infrared diode laser light by nonlinear QPM waveguides has become one of the leading techniques for developing compact blue light sources. A critical measure of the doubler quality is the normalized efficiency defined as:

$$\eta_{NOR} = \frac{P_{2\omega}}{P_{\omega}^2 L^2} \cdot 100 \ [\% \ W^{-1} \ cm^{-2}] \qquad (1)$$

where L is the waveguide length, $P_{\omega}$ and $P_{2\omega}$ are the powers of the fundamental and second harmonic waves measured usually at the end face of the waveguide. Considerable effort is invested by many research groups to increase the efficiency of QPM doublers in order to meet the power levels required by the industry. Normalized efficiency of 220% $W^{-1}cm^{-2}$ has been reported for $LiTaO_3$ [2], over 400% $W^{-1}cm^{-2}$ for KTP[3] and 600% $W^{-1}cm^{-2}$ for $LiNbO_3$ [4].

In this work we present results of normalized efficiency values between 700% $W^{-1}$ $cm^{-2}$ and 800% $W^{-1}$ $cm^{-2}$. To the best of our knowledge, these are the highest values given in the literature for any QPM waveguide. Periodically segmented waveguides were fabricated on the $z^-$ surface of flux grown KTP wafers by an improved ion exchange process in a $Rb(Ba)NO_3$ salt bath. The length of the waveguides was 3.8 mm and the basic period length 4.0 μm. The optical measurement setup includes a Ti/sapphire laser beam, the intensity of which is controlled by a variable density filter and is end-face coupled into the waveguide. The output light is split into the infrared and blue components, which are measured simultaneously. Extra care was taken in calibrating the power readings, using two different power meters which agreed within ± 2%. In order to minimize heating and mechanical drift effects, the power scan time was relatively short.

Results of the blue light output as a function of the fundamental power for two power scans are shown in Figure 1. The results for one scan (triangles) correspond to $\eta_{NOR}$ = 800% $W^{-1}$ $cm^{-2}$ for IR power up to 30 mW. For higher power the efficiency is reduced, probably due to heating effects which alter the QPM conditions. The other scan (rectangles) was taken after a slight change in the optical alignment, resulting in an efficiency of 700% $W^{-1}$ $cm^{-2}$ over a wide range of intensities. At high power, the results start to deviate from the quadratic dependence with an apparent increase in the efficiency toward 800 $W^{-1}$ $cm^{-2}$. This deviation is partly due to the loss in infrared power which is converted into blue light. This effect is demonstrated in Figure 2, which shows the transmitted infrared and generated blue light intensities as a function of wavelength.

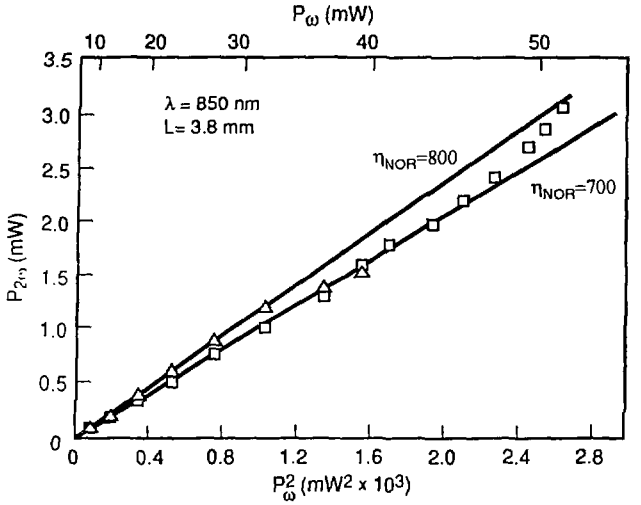


Fig. 1: Generated second harmonic power *vs* input fundamental power.

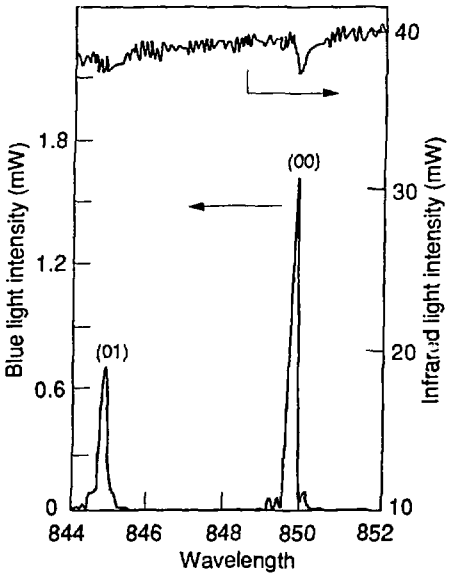


Fig. 2: Generated second harmonic power and transmitted fundamental power *vs* fundamental wavelength.

The normalized efficiency values, predicted by the theory for these waveguides, were calculated using waveguide parameters determined from the optical measurements and the equivalent waveguide model[5]. For $d_{33}$ = 13.6 pm/V, the conventional value for the optical nonlinear coefficient of KTP, we obtained $\eta_{NOR}$ = 340% $W^{-1}$ $cm^{-2}$. However, if we use $d_{33}$ = 21 pm/V, the higher value suggested recently[3], $\eta_{NOR}$ comes to 800% $W^{-1}$ $cm^{-2}$, similar to our best measured values. Thus, we may regard these results as a confirmation of the higher $d_{33}$ value for KTP.

*References*


[1] D. Eger, M. Oron, M. Katz and A. Zussman, Submitted to *OSA Topical Meeting on Compact Blue-Green Lasers* (Salt Lake City, UT, USA, Feb. 1994).

[2] K. Yamamoto, K. Mizuuchi, Y. Kitaoka and M. Kato, *OSA Topical Meeting on Compact Blue-Green Lasers* (New Orleans, LA, USA, Feb. 1993).

[3] J.D. Bierlein, *OSA Topical Meeting on Compact Blue-Green Lasers* (Santa Fe, NM, USA, Feb. 1992).

[4] M. Yamada, N. Nada, M. Saitoh and K. Watanabe, *Appl. Phys. Lett.* 62: 435 (1993).

[5] D. Eger, M. Oron and M. Katz, *J. Appl. Phys.* 74: 4298 (1993).


## *Highly Efficient Blue Light Generation in KTP Waveguides*[1]


D. Eger, M. Oron, M. Katz and A. Zussman



Very high normalized efficiency, up to 800% $W^{-1}$ $cm^{-2}$ for infrared to blue light conversion, was obtained in quasi phase matched waveguides to $KTiOPO_4$. This is the highest value reported for nonlinear waveguides. The effective nonlinear coefficient of the waveguide was found to be considerably larger than that of the host crystal.


*Reference*


[1] D. Eger, M. Oron, M. Katz and A. Zussman, Submitted to *Appl. Phys. Lett.*


## A Miniature Magnetic Bottle Confined by Circularly Polarized Laser Light[1]


E. Kolka, S. Eliezer and Y. Paiss



A new concept of hot plasma confinement in a miniature magnetic bottle induced by circularly polarized laser light is suggested in this work. Magnetic fields generated by circularly polarized laser light may be of the order of megagauss. In this configuration the

circularly polarized light is used to achieve confinement of a plasma contained in a good conductor vessel. The poloidal magnetic field induced by the circularly polarized laser and the efficiency of laser absorption by the plasma are calculated in this work. The confinement in this scheme is supported by the magnetic forces and the Lawson criterion for a DT plasma can be achieved for number density $n \approx 5 \cdot 10^{21}$ cm$^{-3}$ and confinement time $\tau = 20$ nsec. The laser and plasma parameters required to get an energetic gain are calculated.

*Reference*

[1] E. Kolka, S. Eliezer and Y. Paiss, *Phys. Lett. A* 180: 132 (1993).

## Generation of a Poloidal Magnetic Field by Circularly Polarized Laser Light[1]

S. Eliezer, Y. Paiss and H. Strauss*

Circularly polarized laser light can be used to produce a poloidal magnetic field in laser-produced inertially confined plasmas. The poloidal field combined with the naturally occurring toroidal field, gives a spheromak-like magnetic field, which could be beneficial as a thermal insulator.

*Reference*

[1] S. Eliezer, Y. Paiss and H. Strauss, *Phys. Lett., A* 164: 416 (1992).

## A Stochastic Substitute for Coupled Rate Equations in the Modeling of Highly Ionized Transient Plasmas[1]

S. Eliezer, R. Falquina** and E. Mínguez**

Plasmas produced by intense laser pulses incident on solid targets often do not satisfy the conditions for local thermodynamic equilibrium, and so cannot be modeled by transport equations relying on equations of state. A proper description involves an excessively large number of coupled rate equations connecting many quantum states of numerous species having different degrees of ionization. Here we pursue a recent suggestion to model the plasma by a few dominant stages perturbed by a stochastic driving force. The driving force is

*New York University, New York, NY, USA.

**Institute of Nuclear Fusion, Polytechnic University of Madrid, Madrid, Spain.

taken to be a Poisson impulse process, giving a Langevin equation which is equivalent to the Fokker-Planck equation for the probability density governing the distribution of electron density. An approximate solution to the Langevin equation permits calculation of the characteristic relaxation rate. An exact stationary solution to the Fokker-Planck equation is given as a function of the strength of the stochastic driving force. This stationary solution is used, along with a Laplace transform, to convert the Fokker-Planck equation to one of the Schrödinger type. We consider using the classical Hamiltonian formalism and the WKB method to obtain the time-dependent solution.

*Reference*

[1] S. Eliezer, F. Falquina and E. Mínguez, *Phys. Rev., E.* (1994, in press).

## Numerical and Theoretical Studies of the Ignition of ICF Plasmas Driven by Ion Beams[1]

J.M. Martínez-Val*, S. Eliezer, G. Velarde*, H. Hora**, J.J. Honrubia*, M. Piera*, P. Velarde*, J.M. Perlado*, E. Mínguez* and J.M. Aragonés*

Deuterium-tritium plasma inertially confined can undergo fusion ignition if some requirements are met. The final temperature of the plasma at the end of the implosion process has to be high enough to produce overheating of the plasma by energy deposition of the fusion products. Fusion reactivity begins to be relevant above 1 keV ($10^{-20}$ $cm^3/s$), but radiation losses must be taken into account as a cooling mechanism. Theoretical analysis and numerical simulation point out that the losses can be minimized if the plasma is optically thick (before the fusion burst) and ignition can be triggered at moderate temperatures. Stagnation-free targets produced by optimized pusherless implosions can reach high energy gains if certain criteria, established in this work, are met.

*Reference*

[1] J.M. Martínez-Val, S. Eliezer, G. Velarde, H. Hora, J.J. Honrubia, M. Piera, P. Velarde, J.M. Perlado, E. Mínguez and J.M. Aragonés, Submitted to *Nuovo Cimento, A.*

*Institute of Nuclear Fusion, Polytechnic University of Madrid, Madrid, Spain.

**CERN, Geneva, Switzerland.

## How Double Layers Accelerate Charged Particles[1]

S. Eliezer, H. Hora*, E. Kolka, F. Green** and H. Szichman

After the theory of dynamic double layers in laser-produced plasmas led to several significant results in agreement with measurements, including particle acceleration, a clarification is given to the paper by Bryant *et al.*[2] negating such acceleration. The discrepancy seems to be in the definition of static double layers in contradiction to dynamic double layers that are created in laser-induced plasma. We present new results on the acceleration of electrons in a laser irradiated plasma by double layer mechanisms.

*References*

[1] S. Eliezer, H. Hora, E. Kolka, F. Green and H. Szichman, Submitted to *Nuovo Cimento, A.*

[2] D.A. Bryant, R. Bingham and U. de Angelis, *Phys. Rev. Lett.* 68: 37 (1992).

## Melting Phenomenon in Laser-Induced Shock Waves[1]

Z. Henis and S. Eliezer

The melting fraction in laser-induced shock waves in aluminum was estimated as a function of the shock pressure. The results show that partial melting can begin during the relaxation of a shock pressure of 680 kbar. It is suggested that for very short laser pulses (femtoseconds), a supercooling phenomenon may occur without melting during the rarefaction wave.

*Reference*

[1] Z. Henis and S. Eliezer, *Phys. Rev., E* 48: 2094 (1993).

## Increase of Multilayer X-ray Reflectivity Induced by Pulsed Laser Heating[1]

A. Zigler***, M. Fraenkel***, Z. Henis, E. Kolka and S. Eliezer

The reflectivity of tungsten-carbon multilayers exposed to 7 nanosecond Nd-YAG laser

*CERN, Geneva, Switzerland.

**CSIRO, Division of Applied Physics, NSW, Australia.

***Hebrew University of Jerusalem, Jerusalem.

heating, was measured using X-ray diffraction of soft X-ray radiation at 4.4 nm. The reflectivity permanently increased and the Bragg angle decreased after heating the multilayer at fluences of 0.3 J/cm$^2$. The reflectivity increase was achieved in a narrow domain of heating fluences.

A quantitative model based on laser absorption and heat transport was developed. It explains the melting phenomenon of tungsten and the heating to a temperature where graphitization is possible in the carbon layers. The increase in X-ray reflectivity and in expansion of the multilayer mirror can be explained by the laser heating. The improvement in reflectivity is caused by the smoothening of the tungsten layers due to melting, while the change in the spacing is attributed to the carbon phase transition (graphitization).

*Reference*

[1] A. Zigler, M. Fraenkel, Z. Henis, E. Kolka and S. Eliezer, *J. Appl. Phys.* (1994, in press).

## Secondary Ion Mass Spectrometry Analysis of Hypervelocity Microparticle Impact Sites on LDEF Surfaces[1]

C.G. Simon*, A.J. Buonaquisti**, D.A. Batchelor**, J.L. Hunter**, D.P. Griffis**, V. Misra**, D.R. Ricks**, J.J. Wortman**, D.E. Brownlee+, S.R. Best++, M.S. Crumpler++, B. Arad, S. Eliezer, E. Moshe, S. Maman and I. Gilath

Two-dimensional elemental ion maps have been recorded for hundreds of microparticle impact sites and contamination features on LDEF surfaces. Since the majority of the analyzed surfaces were metal-oxide-silicon impact detectors from the Interplanetary Dust Experiment, a series of 'standard' and 'blank' analyses are included. Hypervelocity impacts of forsterite olivine microparticles on activated flight sensors served as standards, while stylus and pulsed laser simulated 'impacts' served as analytical blanks.

Results showed that despite serious contamination issues, impactor residues can be identified in ~ one-third of the impact sites. While aluminum oxide particles cannot be detected on the aluminum surface, remnants of manmade debris impactors consisting of paint chips and bits of metal have been identified on surfaces from LDEF Rows 3 (west or trailing side), 6 (south), 9 (ram or leading side), 12 (north) and the space end. Higher than expected ratios of manmade microparticle impacts to total microparticle impacts have been identified on the space end and the trailing side.

*Inst. for Space Science and Technology, Gainesville, FL, USA.

**North Carolina State University, Raleigh, NC, USA.

+Astronomy Department, University of Washington, Seattle, WA, USA.

++Space Power Institute, Auburn University, Auburn, AL, USA.

Large numbers of contamination interferences were identified and their effects on impactor debris identification were mitigated during the course of this study. These interferences include pre-, post- and in-flight deposited surface contaminants as well as indigenous heterogeneous material contaminants. Non-flight contaminations traced to human origins, including spittle and skin oils, contributed significant levels of alkali-rich carbonaceous interferences. A ubiquitous layer of in-flight deposited silicaceous contamination varied in thickness with location on LDEF and proximity to active electrical fields even on a micro scale. In-flight deposited (low velocity) contaminants include urine droplets and bits of metal film from eroded thermal blankets.

*Reference*

[1] C.G. Simon, A.J. Bernaquisti, D.A. Batchelor, J.L. Hunter, D.P. Griffis, V. Misra, D.R. Ricks, J.J. Wortman, D.E. Brownlee, S.R. Best, M.S. Crumpler, B. Arad, S. Eliezer, E. Moshe, S. Maman and I. Gilath, *Third LDEF Post-Retrieval Symp.* (Williamsburg, VA, USA, Nov. 1993).

## Impulsive Loading of Materials Using Laser-Induced Shock Waves[1]

I. Gilath and S. Eliezer

There are different impact methods to study the dynamic fracture of materials: ballistics, high explosives and pulsed high irradiance lasers. In these methods, shock waves are produced on the front of the target by intense short-time energy deposition. When reaching the back free surface they are reflected as rarefaction waves. Rarefaction waves start also from the front when the impact load is finished. The interaction of the rarefaction waves induces tension in the target. If the magnitude and duration of this tensile stress are greater than the dynamic strength of the material, fracture or spall occurs.

The advantage of short pulsed laser-produced shock waves lies in the possibility of studying the dynamic fracture of materials at hypervelocity impact conditions in controlled small-scale laboratory experiments. Absorption of the laser radiation by the target takes place within a very thin layer near the irradiated surface. The rapid temperature increase causes ablation and plasma ejection into the vacuum. This expansion drives a strong shock wave into the target. Megabar pressures are easily obtained on the impact site. One-dimensional (1-D) impact geometry can be obtained when the laser spot is greater than sample thickness, or spherical shock waves for focused beam. Shock wave attenuation was measured experimentally using the effect of spall for different target widths[2]. This pressure decay in 1-D geometry, dP/dx, leads to a dependence of the threshold ablation pressure to produce incipient spall on target width, while the fracture stress is constant. For 1-D impact geometry,

a linear dependence was found between the threshold ablation pressure and target width for different materials. The slope represents the pressure gradient dP/dx, and the spall strength is obtained by extrapolating to zero target width. For spherical shock waves, the shock pressure attenuation is proportional to the squared distance from the impact site[3].

The controlled stepwise increase in laser energies allowed the stages of damage evolution to be found from threshold conditions up to sample perforation. The threshold or incipient spall appears as small internal voids or cracks in the spall plane. The spall plane is well defined and perpendicular to the shock propagation with no lateral dispersion. For increased energy deposition, the voids or cracks coalesce to form the spall layer as a result of internal fracture. For higher energies the spall layer is detached and then the sample is perforated. Spall behavior of different materials was studied: metals, composites, ceramics and multilayered assemblies[4].

The effect of spall was used to estimate the maximum elongation at fracture for metals. The results are in very good agreement with that obtained by the expanding ring method[5].

A simple damage criterion was included in the numerical simulation of the spall development. Also the strain rate was obtained from the simulation[6]. This strain rate, of the order of $10^7$ $sec^{-1}$, is the highest obtained in the laboratory, enabling the study of dynamic properties of materials in different shock impact configurations.

*References*


[1] I. Gilath and S. Eliezer, *Abstracts IUTAM Symp. on Impact Dynamics* (Beijing, P.R. China, Oct. 1993).

[2] S. Eliezer, Y. Gazit and I. Gilath, *J. Appl. Phys.* 68: 356 (1990).

[3] I. Gilath, S. Eliezer and T. Bar-Noy, *Laser Part. Beams* 11: 221 (1993).

[4] I. Gilath, S. Eliezer, T. Bar-Noy, R. Englman and Z. Jaeger, *Int. J. Impact Eng.* 14: 279 (1993).

[5] I. Gilath, S. Eliezer, M.P. Dariel and L. Kornblith, *J. Mater. Sci. Lett.* 7: 915 (1988).

[6] S. Eliezer, I. Gilath and T. Bar-Noy, *J. Appl. Phys.* 67: 715 (1990).


## Hemispherical Shock Wave Decay in Laser-Matter Interaction[1]


I. Gilath, S. Eliezer and T. Bar-Noy



A high-irradiance short-pulsed laser was used to generate hemispherical shock waves in planar targets. A linear relationship was obtained between the laser energy for threshold spall conditions ($E_l$) and the cubic target thickness ($d$):$E_L = 45.3d^3 + 4.9$, where $E_L$ is in J and $d$ is in mm. It was found that the laser-induced ablation pressure decays with the distance to a power slightly greater than 2.


*Reference*


[1] I. Gilath, S. Eliezer and T. Bar-Noy, *Laser Part. Beams* 11: 221 (1993).

## Two-Dimensional Effects of Laser-Induced Shock Waves in Aluminum[1]

M. Werdiger, E. Moshe, B. Arad, Y. Gazit [deceased], S. Eliezer and S. Maman

The time development of laser shock waves in aluminum targets was measured by laser backlighting for different foil thicknesses. The diagnostic laser is a continuous He-Ne of approximately 5 mW. The laser backlighting is significantly reduced when the shock wave reaches the rear surface. The shock wave geometry changes from one-dimensional (1D) to two-dimensional (2D) with increasing foil thickness. Experimental measurements were made with Nd laser (1.06 μm) irradiances of $7 \cdot 10^{13}$ W/cm$^2$ and a pulse duration of 7 nsec. The aluminum foil thicknesses ranged between 40 μm and 1000 μm. The laser focal spot diameter was 180 μm and therefore 2D effects were analyzed for the thicker targets. The experimental results are described, to a very good approximation, by a shock wave pressure profile $P=C/X^n$, where X is the foil thickness, C is a constant related to the ablation pressure, and $0<n<3$. For large X (X>300 μm), n=3, while for 80 μm<X<200 μm, n=1 is a good approximation. The $X-t$ measurements (t is the shock wave time of arrival at the rear surface of the foil) satisfy the differential equation:

$$P=C/X^n=A(dX/dt)+B(dX/dt)^2$$

where dX/dt is the shockwave velocity and A,B are equation-of-state constants, the same as derived by 1D shock wave experiments.

*Reference*

[1] M. Werdiger, E. Moshe, B. Arad, Y. Gazit, S. Eliezer and S. Maman, *Abstracts Int. Summer School and Workshop on Nuclear Fusion and Plasma Physics* (Hefei, P.R. China, Oct. 1993).

## Remote Spectroscopic Analysis with Optical Fibers§

A. Bornstein, Y. Friedman, R. Herman, E. Nir, A. Peled,
I. Tugendhaft, Y. Yarimi, Y. Weissman and S. Lowry*

Infra-red spectroscopy is a well known method for obtaining chemical information on a wide range of materials. It has numerous applications in research, development and industry.

Spectroscopic analysis is performed by dedicated instruments – spectrometers. In order to analyze a material, a sample must be prepared, mounted on a sampling device, and inserted

§This work was partially financed by the BIRD Foundation.

*Nicolet Corporation, Madison, WI, USA.

into a special compartment in the spectrometer. This procedure limits the application range to off-line and *ex situ* measurements.

Quality control and optimization of resource utilization are important characteristics of modern industrial processes. On-line spectroscopic monitoring can fulfill both requirements. Recent studies revealed that infra-red spectroscopy can serve as a medical diagnosis tool[1]. *In situ* spectroscopic sampling opens the exciting possibility of 'optical biopsy'.

Soreq developed a line of products which give a remote sampling capability to commercial spectrometers. These products are based on special fibers, which are transparent in the infra-red. The fibers are used to deliver the infra-red light to the tested material, and to return the spectral signature back to the instrument for analysis. The sampling device itself has the shape of a needle, and can yield highly localized spectroscopic information. With the Soreq kit, any commercial spectrometer can be used for on-line and *in situ* measurements.

These new products will be available soon through a major distributor worldwide.

*Reference*

[1] P.T.T. Wong, R.K. Wong, T.A. Caputo, T.A. Godwin and B. Rigas, *Proc. Natl. Acad. Sci. U.S.A.* 88: 10988 (1991).

## The Response of Faraday-Effect Fiber-Optic Current Sensors to Noncentered Currents[1]

E. Shafir, N. Shaked, A. Ben-Kish* and M. Tur*

Experimental evidence and theoretical investigations (based on the presence of linear birefringence) are presented for the dependence of the output of a Faraday-rotation fiber-optic current sensor on the location of the electrical conductor. Such sensors were demonstrated to have some unique advantages over conventional technologies in high electrical current measurements [2,3]. In these devices the polarization of the light rotates as it propagates down the fiber loops encircling the current-carrying conductor. The magnitude of the current flowing in the conductor can then be deduced from a measurement of the state of polarization of the light at the fiber output. The ability of these devices to measure the current directly (rather than its time derivative), their wide temporal bandwidth and high dynamic range, as well as their inherent EMI immunity and lack of saturation effects, make them very good candidates for the new generation of high current sensors.

*Tel-Aviv University, Tel Aviv.

Ideally, the device should have a response which is independent of the exact location of the electrical conductor *within* the fiber loop, the zero response for conductors outside the loop. However, location-dependent response can be observed [4] for very fast currents which change in a time scale comparable to the time-of-flight of the photons in the fiber loop.

It is well known [5] that linear birefringence (either intrinsic or externally introduced when the fiber is bent to form the sensor loop) severely limits the sensitivity of Faraday-effect fiber-optic current sensors [6]. We obtained experimental evidence and analyzed theoretically that the presence of linear birefringence introduces a significant dependence of the response on the conductor location even for low frequency and DC currents. Moreover, external conductors produce a nonzero response. This dependence of the sensor response on offset current distribution was mentioned but found to be negligible in a previous publication [7], describing a current sensor made of a fiber with a very strong twist circular birefringence bias.

*References*


[1] E. Shafir, N. Shaked, A. Ben-Kish and M. Tur, *Proc. 9th Optical Fiber Sensors Conf.* (Florence, Italy, May 1993), pp. 435-438.

[2] G.W. Day and A.H. Rose, *Proc. SPIE* 985: 138 (1988).

[3] G.W. Day, *Proc. 6th Optical Fiber Sensors Conf.* (1989) pp. 250-254.

[4] R.W. Cernosek, *Proc. 8th Optical Fiber Sensors Conf.* (1992) pp. 398-401.

[5] A. Ben-Kish, N. Konforti, M. Tur and E. Shafir, *Proc. 7th Optical Fiber Sensors Conf.* (1990) pp. 97-100.

[6] A. Ben-Kish, M. Tur and E. Shafir, *Opt. Lett.* 16: 687 (1991).

[7] P.R. Roman and F.C. Jahoda, *Appl. Opt.* 27: 3088 (1988).


## Faraday-Rotation Fiber-Optic Current Sensor: Response to Different Locations of the Conductor[1]


M. Tur*, A. Ben-Kish*, E. Shafir and N. Shaked



Faraday-rotation fiber-optic current sensors were demonstrated to have some unique advantages over conventional technologies in high electrical current measurements. In these devices the linear polarization of the light rotates as it propagates along the fiber loops which encircle the current-carrying conductor. This polarization rotation can in turn be evaluated at the fiber output, thereby giving a measure of the current flowing in the conductor. The ability of these devices to measure directly the current (rather than its time derivative), their natural high bandwidth and high dynamic range, as well as their inherent EMI (Electro-Magnetic Interference) immunity and lack of saturation effects, render them very good candidates for next generation high current sensors.



*Tel-Aviv University, Tel Aviv.

It has long been realized that the linear birefringence exhibited by the sensing fiber, due mainly to the bending it undergoes in forming the sensor loop, may cause severe degradation of the performance of these devices. The major effect of this birefringence is to decrease the magnitude of the device scale factor, and thus its sensitivity. In addition, the scale-factor, being dependent on this birefrigence, becomes quite sensitive to a variety of environmental effects.

We claim that this birefrigence is responsible for still another effect. It may introduce a dependence of the device output on the location of the conductor *within* the loop and may generate non-zero signals for currents flowing *outside* the loop. Numerical calculations show a signal variation of up to ~10% as the conductor is moved around the circumference of the loop.

*Reference*

[1] M. Tur, A. Ben-Kish, E. Shafir and N. Shaked, *Proc. SPIE* 1972:324.

## Nonlinear Transmission Characteristics of Carbon-Black Suspensions[1]

A. Fein, Z. Kotler, J. Bar-Sagi, S. Jackel, P. Shaier and B. Zinger

We have measured the threshold energy for the onset of nonlinear opacity in suspensions consisting of carbon-black particles in various solvents. The threshold energies are found to depend strongly on the solvent. Measurements of nonlinear scattering exhibit a very strong correlation between the scattering threshold and the opacity threshold. Fluorescence measurements reveal, in contrast, that the threshold for plasma formation associated with optical breakdown is nearly uniform and almost independent of the solvent. The opacity threshold is attributed in most cases to enhanced scattering caused by micro-bubbles that are formed around the particles at incident energies below the plasma threshold. This is consistent with calculations of the heat flow from a carbon-black particle to the surrounding medium. Calculations made of the scattering cross-section of the particle surrounded by a bubble showed an increase when the bubble radius was equal to or larger than the particle radius.

*Reference*

[1] A. Fein, Z. Kotler, J. Bar-Sagi, S. Jackel, P. Shaier and B. Zinger, *3rd French-Israeli Symp. on Nonlinear Optics* (The Dead Sea, Israel, Feb. 1994).

## Gamma Radiation Effects on Some Optical Glasses[1]

M.J. Liepmann*, L. Boehm and Z. Vagish

A study was made of the effects of $^{60}Co$ gamma irradiation on the transmission and index of refraction of several optical glass types. The glasses have indices (nd) in the range of 1.486 to 1.581. They are multicomponent glasses from different families. UV-transmitting glasses having lower impurity levels are compared with the standard optical glasses. Transmission spectra in the range of 190-820 nm were recorded after exposure to various doses of radiation up to 725 krad. In all samples, the UV transmission edge shifted towards longer wavelengths and the visible transmission decreased. Differences in transmission spectra were observed depending on the glass composition and impurity levels. Fading curves of some glasses irradiated with different doses of gamma radiation were studied at room temperature and after heat treatment of 400°C or 500°C. At room temperature a slight recovery with time was observed. One fluorophosphate glass type recovered nearly completely after heating for a few hours. The effect of impurities on recovery was considered.

*Reference*

[1] M.J. Liepmann, L. Boehm and Z. Vagish, *Proc. SPIE* 1761: 284 (1993).

## Optical Spectroscopy of $Cr^{4+}:Y_2SiO_5$[1]

C. Deka**, M. Bass, B.H.T. Chai** and Y. Shimony

Spectroscopic data on the absorption and the fluorescence spectra and fluorescence lifetimes are presented for $Cr^{4+}:Y_2SiO_5$, the newest $Cr^{4+}$-doped laser crystal. The fluorescence measurements were conducted at temperatures ranging from 10 to 310 K, and the absorption spectra were measured at room temperature and 77 K. Spectroscopic analysis of the absorption and the emission spectra is performed on the basis of a distorted tetrahedral symmetry for the $Cr^{4+}$ site, namely $C_{3v}$. The tetravalent chromium substitutes for $Si^{4+}$ in this crystal, and there is no evidence for the presence of chromium in any other valence state. The $Cr^{4+}$ site is characterized by strong crystal field parameters. We have tentatively assigned the sharp line at 1146 nm in the low-temperature fluorescence spectrum (excited by 1064-nm radiation) to the spin-forbidden singlet-to-triplet transition $^1E$–$^3A_2$, and the broad band with the peak at 1225 nm to the spin-allowed $^3T_2$–$^3A_2$ transition. Excitation at 532 nm results in

*Schott Glass Technologies Inc., Duryea, PA, USA.

**Center for Research in Electro-Optics and Lasers, University of Central Florida, Orlando, FL, USA.

an additional type of emission in the near infrared. A similar dependence of the lasing wavelength on the pump wavelength was observed in the laser operation of the crystal at 77 K[2].

*References*


[1] C. Deka, M. Bass, B.H.T. Chai and Y. Shimony, *J. Opt. Soc. Am., B: Opt. Phys.* 10: 1499 (1993).

[2] B.H.T. Chai, Y. Shimony, C. Deka, X.X. Zhang, E. Munin and M. Bass, in: *Advanced Solid-State Lasers*. L.L. Chase and A.A. Pinto [Eds.] (Washington, DC: Optical Society of America, 1992), p. 28.


## Symmetry Lowering Due to Site-Occupation Disorder in Vibrational Spectra of Gehlenite, $Ca_2(AlSi)AlO_7$[1]


Z. Burshtein, Y. Shimony, S. Morgan*, D.O. Henderson*, R. Mu* and E. Silberman*



Raman scattering and infrared reflectance spectra of a gehlenite crystal, $Ca_2(AlSi)AlO_7$, were measured. The data indicate clearly a lowering of the crystal symmetry from $D_{2d}$ to $S_4$ due to occupation disorder in one of the $C_s$ sites, which statistically accommodates either a Si or an Al ion. Forty of the 51 theoretically expected Raman active bands, and 21 of the 35 expected i.r. bands have been resolved and assigned.


*Reference*


[1] Z. Burshtein, Y. Shimony, S. Morgan, D.O. Henderson, R. Mu and E. Silberman, *J. Phys. Chem. Solids* 54: 1043 (1993).


## Refractive-Index Anisotropy and Dispersion in Gehlenite, $Ca_2Al_2SiO_7$, between 308 and 1064 nm[1]


Z. Burshtein, Y. Shimony and I. Levy



Refractive-index anisotropy and dispersion were measured in a tetragonal gehlenite ($Ca_2Al_2SiO_7$) single crystal between 308 and 1064 nm at room temperature. Use was made of the bireflectance effect in an oriented single-crystal prism for obtaining an accurate measurement of the anisotropy. At the wavelength $\lambda$ =632.8 nm, the ordinary and the extraordinary refractive indices $n_o$ and $n_e$ were $n_o = 1.663 \pm 0.0015$ and



*Dept. of Physics, Fisk University, Nashville, TN, USA

$n_e = n_o - 0.0085 \pm 0.0002$, respectively. The dispersion was fitted to a Sellmeier function $n^2 = 1 + A\lambda^2/(\lambda^2 - B)$, with $A_o = 1.712 \pm 0.004$, $A_e = A_o - (25 \pm 1) \times 10^{-3}$, $B_o = (1.196 \pm 0.005) \times 10^{-2}$ $(\mu m)^2$, and $B_e = (1.133 \pm 0.005) \times 10^{-2}$ $(\mu m)^2$.

*Reference*

[1] Z. Burshtein, Y. Shimony and I. Levy *J. Opt. Soc. Am., Part A Opt. Image Sci.* 10: 2246 (1993).

## Photon Flux Optimization in Three-Color Multiphoton Ionization of Uranium Atoms[1]

D. Levron, A. Bar-Shalom, Z. Burshtein, R. David,
G. Hazak, J. Ivry, L.A. Levin, J. Oreg and M. Strauss

Ionization probability in three-color excitation of uranium atoms depends on the photon flux which drives the transition to an autoionizing level. For a proper choice of the flux ratio, the ionization probability is insensitive of the actual fluxes over a considerable range (Table 1). Thus, the laser intensities used may be lower by a factor of approximately 3 as compared with values predicted on the basis of cross-sections of the individual transitions. A quantum-mechanical model (see Fig. 1), based on a detailed calculation of population dynamics of the levels in the ionization scheme, predicts the ionization probability as a function of the three-laser intensities. Ionization saturation measurements provide parameters for the model. The theoretical calculations were partially consistent with the experimental results (see Fig. 2). Ionization probabilities as high as 93% are achievable.

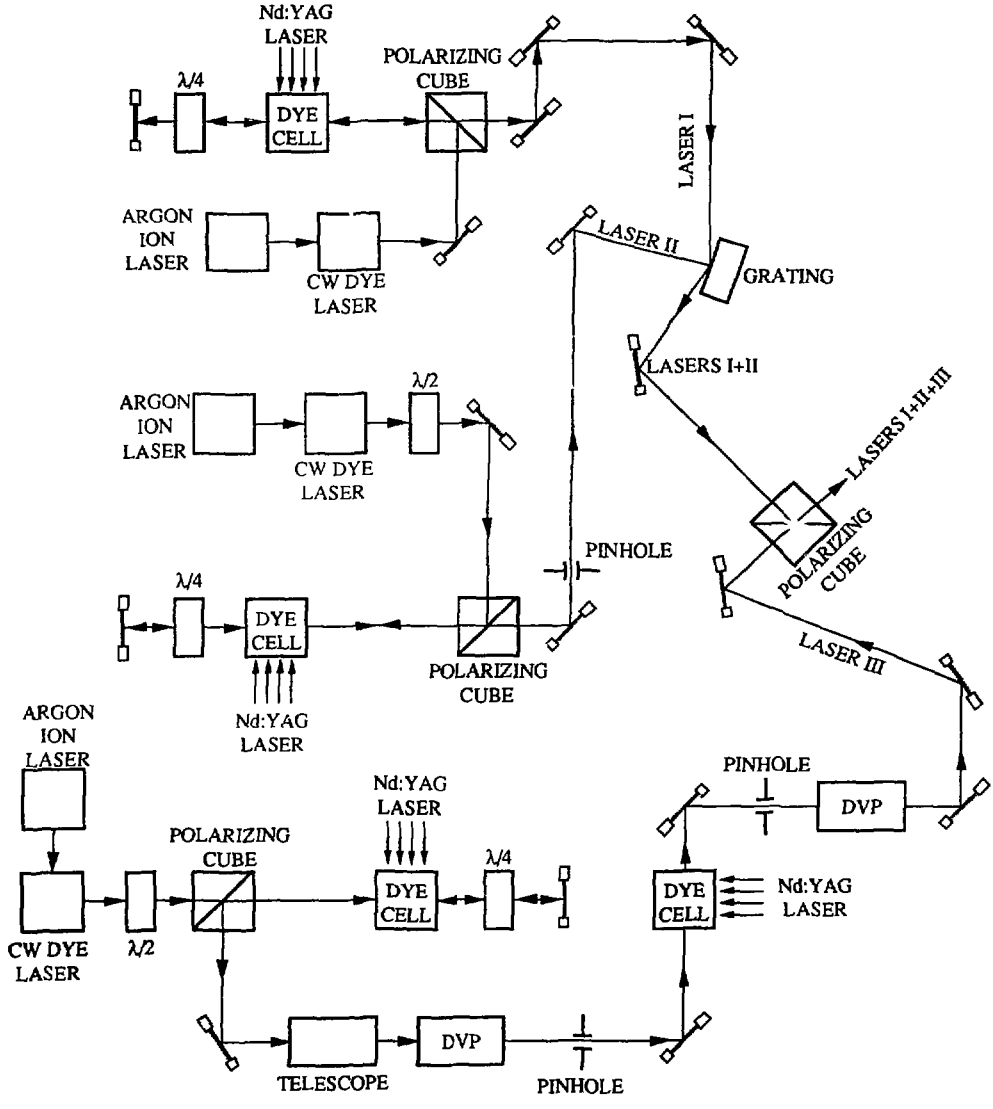


Fig. 1: Block diagram of the three-color laser beam system.

Table 1

**$^{238}$U Ionization probability P for various intensities of the three lasers $I_1$, $I_2$ and $I_3$ (units of mJ/cm$^2$ per 20 ns long pulse)**

| $I_1$ | $I_2$ | $I_3$ | P |
|---|---|---|---|
| 0.05 | 0.5 | 4.0 | 0.89 |
| 0.1 | 0.5 | 4.0 | 0.93 |
| 0.2 | 0.5 | 4.0 | 0.93 |
| 0.15 | 0.5 | 4.0 | 0.93 |
| 0.15 | 0.6 | 4.8 | 0.94 |
| 0.15 | 0.4 | 3.2 | 0.92 |
| 0.5 | 0.5 | 4.0 | 0.89 |
| 1.0 | 0.5 | 4.0 | 0.82 |
| 0.15 | 0.4 | 4.0 | 0.93 |
| 0.15 | 0.6 | 4.0 | 0.93 |
| 0.15 | 0.3 | 4.0 | 0.92 |
| 2.0 | 0.5 | 4.0 | 0.69 |
| 0.02 | 0.5 | 4.0 | 0.77 |
| 0.01 | 0.5 | 4.0 | 0.63 |
| 0.005 | 0.5 | 4.0 | 0.45 |
| 4.0 | 0.5 | 4.0 | 0.43 |
| 0.3 | 1.0 | 8.0 | 0.91 |
| 8.0 | 1.0 | 8.0 | 0.51 |
| 0.01 | 1.0 | 8.0 | 0.63 |

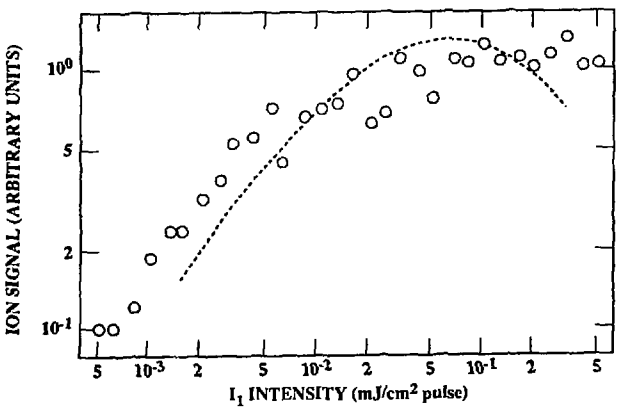


Fig. 2: $^{238}$U ion signal as a function of $I_1$ for $I_2 = 0.12$ mJ/cm$^2$, and $I_3 = 0.25$ mJ/cm$^2$. Circles – experimental results; dashed line - theoretical calculations.

*Reference*

[1] D. Levron, A. Bar-Shalom, Z. Burshtein, R. David, G. Hazak, J. Ivry, L.A. Levin, J. Oreg and M. Strauss, *Proc. SPIE* 1859: 69 (1993).

## $Cr^{4+}$ Solid State Passive Q-Switch for Pulsed Nd:YAG Laser[1]

Y. Kalisky and Y. Shimony

$Cr^{4+}$ doped garnets are emerging as novel, simple, efficient and photochemically stable saturable absorbers for 1.06 μm emission of $Nd^{3+}$ lasers. This is due to the tetrahedral $Cr^{4+}$ absorption band in the 0.95-1.25 μm spectral regime. In particular, using $Cr^{4+}$:YAG as a passive Q-switch for a pulsed Nd:YAG laser yielded a suppression of the relaxation oscillations and the appearance of short (FWHM of 28 ns) multispike lasing having an intensity peak up to 30 times greater than the free running spikes. These results, combined with the simplicity as well as the good optical, thermal and mechanical properties of the YAG host, indicate the potential of $Cr^{4+}$ doped YAG passive Q-switch for extracting high average or high peak power from small-size laser systems.

*Reference*

[1] Y. Kalisky and Y. Shimony, *Bull. Isr. Phys. Soc.* 39: 142 (1993).

## Efficient Copper-Vapor Laser Pumped Ti:Sapphire Laser[1]

A. Ben-Amar, J. Kagan, M. Lando, E. Miron, A. Cohen and M. Nahmani

A high-average-power, efficient Ti:Sapphire laser, pumped by an oscillator-amplifier configured copper-vapor laser, is reported. The ϕ 9 x 15 mm Ti:Sapphire rod was made out of a boule grown by the Czochralski method using the Cambridge Instruments Autox machine and annealed in a home-made annealing furnace. The Ti:Sapphire-measured slope efficiency was 38% and the total efficiency was 25% at 3 W broad band output. To the best of our knowledge these are the highest figures reported for both slope and total efficiencies for a copper-vapor laser pumped Ti:Sapphire laser. The polarized pump beam diameter was 28 mm and its full divergence angle, including spatial dither, was 0.26 mRad. Ti:Sapphire laser beam divergence was 2.7 mRad ($M^2 = 7$). The Ti:Sapphire laser pulse buildup time was 25 ns and its pulse width was 8 ns FWHM.

*Reference*

[1] A. Ben-Amar, J. Kagan, M. Lando, E. Miron, A. Cohen and M. Nahmani, *Bull. Isr. Phys. Soc.* 39: 135 (1993).

## Electromagnetic Modeling of a Coaxial, Large-Bore Copper-Vapor Laser[1]

P. Blau

The copper-vapor laser is a pulsed-electric-discharge pumped laser. Modeling of the electric field is essential both for optimization of the pumping process and for development of the excitation circuit. Analysis has shown[2] that the laser impedance cannot be characterized by constant resistance and inductance; however, constant conductivity can be assumed if the temporal dependence of the current density profile is taken into account.

In the model, the temporally and spatially resolved electric field is calculated considering skin effect and transmission-line effect. The plasma conductivity is calculated using estimated electron temperature and measured[3], radially resolved electron density and gas temperature. The current density profile and total current are obtained. Very good agreement exists between calculated and measured laser current in a 100 W, 8-cm-diameter copper-vapor laser.

*References*

[1] P. Blau, *Bull. Isr. Phys. Soc.* 39: 146 (1993).
[2] P. Blau, *IEEE J. Quantum Electron* (1994, in press).
[3] P. Blau, I. Smilanski, S. Gabay and S. Rosenwaks, *CLEO* (1993).

## Penta Prism Laser Polarizer[1]

H. Lotem and K. Rabinovitch*

A novel type of laser prism polarizer is proposed. The polarizer is characterized by high transmission efficiency, a high optical damage threshold, and a high extinction ratio. It is shaped like a regular penta prism and, thus, it is a constant deviation angle device. Polarization effects occur upon the two internal cascade reflections in the prism. Anisotropic and isotropic types of the polarizer were considered. The isotropic polarizer is a prism made of a high-refractive-index glass coated by multilayer polarization-type dielectric coatings. Efficient *s*-state polarization is obtained because of *p*-state leakage upon the two internal cascade reflections. The anisotropic polarizer is made of a birefringent crystal in which angular polarization splitting is obtained by the bireflectance (double-reflection) effect (see Fig. 1). Fanning of a laser beam into up to eight polarized beams is possible in a prism made of a biaxial crystal.

*El-Op, Rehovot.

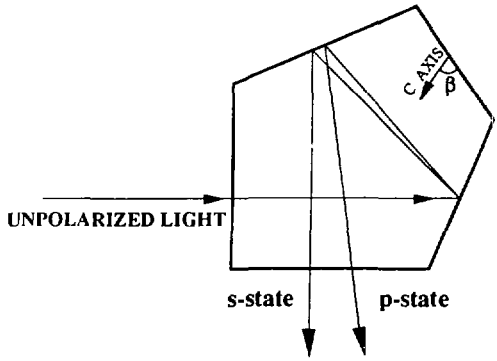


Fig. 1: Schematic description of a penta prism polarizer made of a uniaxial crystal. Splitting of the unpolarized input into just two polarized beams is obtained when the optic axis is in the reflection plane. The maximum splitting angle corresponds to the optic axis alignment with $\beta = 90°$. With a biaxial crystal prism, splitting into eight polarized beams is possible when the crystal axes are not parallel to the reflection plane.

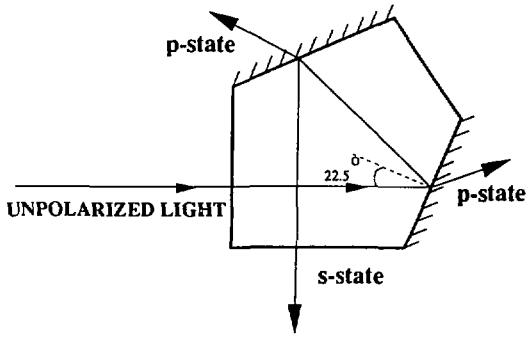


Fig. 2: Schematic description of an isotropic penta prism polarizer. The reflected *s* state is polarized because of a leakage of the *p*-state component on the cascade reflection from the two polarization-type thin-film coatings.

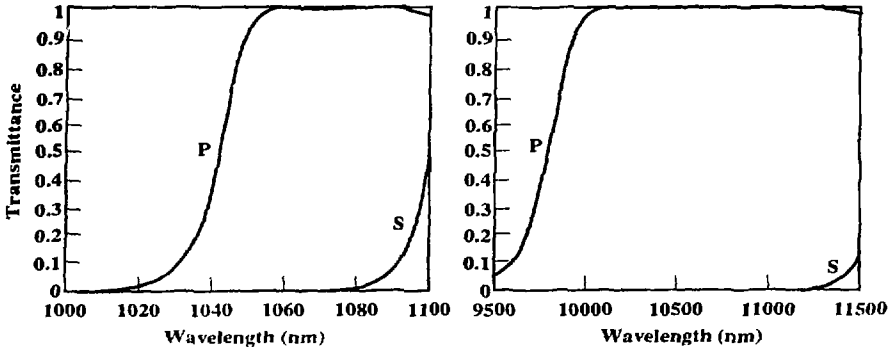


Fig. 3: Theoretical *s*- and *p*-state transmissions for a single polarization-type coating at a 22.5° angle of incidence (left) at $\lambda \sim 1.06$ μm for a bulk with a refractive index of 1.8 and (right) at $\lambda \sim 10.6$ μm for a bulk with a refractive index of 2.4. The isotropic polarizer extinction ratio is proportional to the square of the *s*- to *p*-state reflection ratio.

*Reference*

[1] H. Lotem and K. Rabinovitch, *Appl. Opt.* 32: 2017 (1993).

## Tunable External Cavity Diode Laser that Incorporates a Polarization Half-Wave Plate[1]

H. Lotem, Z. Pan* and M. Dagenais*

The threshold current and spectral properties of a grating tuned external cavity semiconductor laser are improved by utilizing an intracavity half-wave plate to optimize the grating feedback. The external grating cavity is shown in Figure 1.

*Dept. of Electrical Engineering, University of Maryland, College Park, MD, USA.

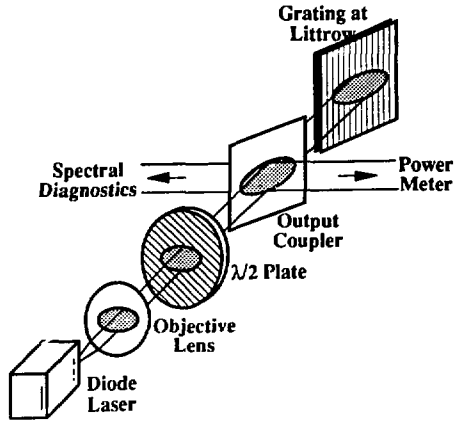


Fig. 1: Schematic description of the external cavity laser. The half-wave plate enhances feedback by matching the diode laser polarization to the high-reflection mode of the grating. The half-wave plate may also control the amount of output coupling by means of an intracavity splitter or the grating zero-order reflection.

*Reference*

[1] H. Lotem, Z. Pan and M. Dagenais, *Appl. Opt.* 31: 7530 (1992).

## Tunable Dual-Wavelength Continuous-Wave Diode Laser Operated at 830 nm[1]

H. Lotem, Z. Pan* and M. Dagenais*

An external grating cavity semiconductor diode laser is made to operate simultaneously at two separately adjustable wavelengths. Lasing is restricted to the vicinity of the solitary laser étalon resonances. Figure 1 shows the external cavity where a single grating controls a dual-wavelength lasing.

*Dept. of Electrical Engineering, University of Maryland, College Park, MD, USA.

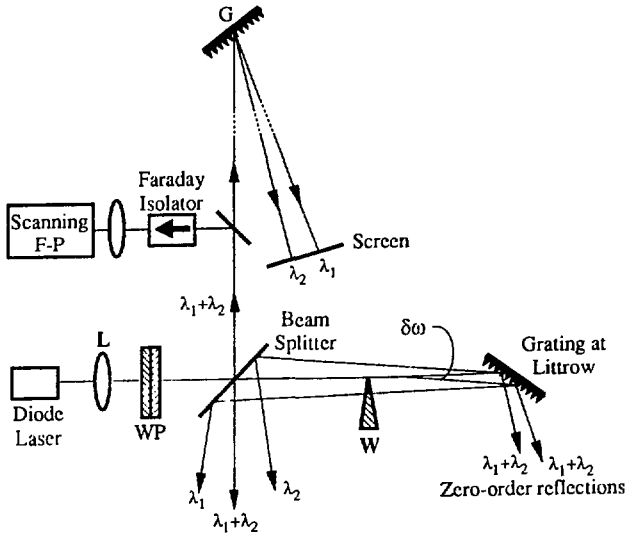


Fig. 1: Schematic description of external-cavity dual-wavelength laser. The grating feedback is enhanced because of polarization rotation by a half wave plate (WP) The wedge (W) deflects approximately one half of the laser beam in the grating-diffraction plane and thus forces lasing at a second wavelength. The scheme corresponds to a case where $\lambda_2 > \lambda_1$.
The top of the figure shows the spectral analysis means. G, high-dispersion grating.

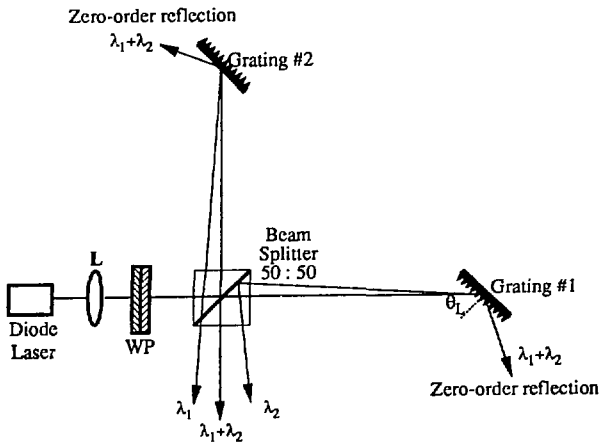


Fig. 2: Dual-wavelength external-cavity scheme in which two independent-grating tuners are optically coupled by a nonpolarized cube beam splitter. The figure corresponds to a case where $\lambda_2 > \lambda_1$. Better control of the two cavity branches is possible by addition of a half-wave plate (WP) in front of each grating and replacement of the beam splitter with a polarized one.

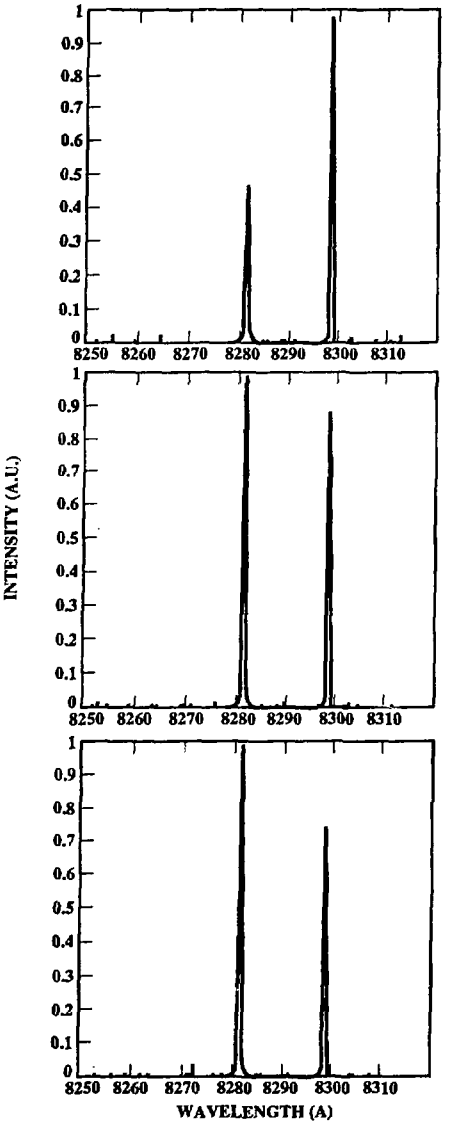


Fig. 3: Dual-wavelength output obtained in the second laser scheme at different injection currents, as resolved by a 0.5-m Spex spectrometer with approximately 0.05 nm resolution. The corresponding diode currents are 84.3, 83.6 and 82.6 mA for the top, middle and bottom spectra, respectively.

## *Reference*

[1] H. Lotem, Z. Pan and M. Dagenais, *Appl. Opt.* 32: 5270 (1993).

# Radially and Temporally Resolved Measurements of Electron Density and Gas Temperature in a Copper-Vapor Laser[1]

P. Blau, I. Smilanski, S. Gabay and S. Rosenwaks*

Accurate measurements of gas temperature and electron density in the plasma of a copper-vapor laser (CVL), under identical conditions, are presented. These parameters are deduced from the emission profiles of the first four atomic hydrogen Balmer lines. Doppler and Stark broadening are the main line broadening mechanisms under the laser operating conditions. The dependence of hydrogen line broadening on gas temperature and electron density is well established. The CVL used is a 100 W, 5.5 KHz repetition rate laser[2]. This laser demonstrates very stable operation for a long period and therefore enables reliable measurements. Atomic hydrogen emission lines from residual hydrogen are detectable both during the pulse and in the afterglow.

The measurement system is described in Figure 1. The line profile is scanned with a Fabry-Pérot Interferometer (FPI). The radiation reaches the FPI through a folding mirror and a spatial filter allows only parallel light to pass through. This setup, combined with an iris, chooses the line of sight (parallel to the laser axis) and the diameter of the sampled zone. By moving the folding mirror perpendicular to the laser axis, different radial zones are sampled. The light exiting the FPI is collected with a lens into a monochromator which serves as a bandpass filter selecting the scanned line. The light is detected by a photomultiplier (P.M.). A digitizing oscilloscope displays the light intensity *versus* the FPI scan voltage, which is proportional to the wavelength. A boxcar integrator, synchronized with the laser, is used to gate the signal for temporal resolution. A HeNe laser beam passing along the CVL axis is utilized to align the optical system and to adjust the FPI finesse. The Free Spectral Range (FSR) of the FPI is adjusted (between 100 and 400 GHz) so that the line profile is well resolved. FSR and line width calibration is done by inserting a fixed gap étalon in the beam path. This étalon modulates the line profile at known intervals, permitting evaluation of the line width.

The analysis of the Doppler and Stark broadening involves evaluation of all other line-broadening mechanisms, including natural, pressure (Van-der-Waals and resonance), instrumental, self-absorption and fine structure splitting. The final profile is thus a Voigt profile. Under our conditions, Doppler broadening dominates for $H_\alpha$ while Stark broadening dominates for the higher Balmer lines. In the deconvolution procedure, interpolation of Voigt function tables was utilized. An iterative algorithm was employed to find the temperature and electron density for which total calculated FWHM matched the measured one for both $H_\alpha$ and one of the following lines: $H_\beta$, $H_\gamma$ or $H_\delta$. Finally, we checked the results by calculating the full line profile and comparing it with the measured one.

*Ben-Gurion University of the Negev, Beer-Sheva.

Recently we reported time-averaged measurements of those parameters along the laser axis[3]. Radially and temporally resolved measurements with enhanced accuracy were achieved here for the first time.

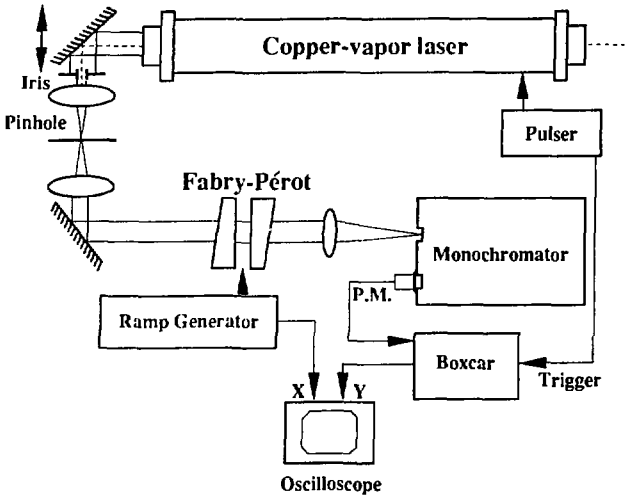


Fig. 1: The experimental setup. The line profile is scanned with a Fabry-Pérot Interferometer. The monochromator serves as a bandpass filter. The boxcar gates the signal, for temporal resolution. The spatial filter determines the sampled zone, for radial resolution.

*References*


[1] P. Blau, I. Smilanski, S. Gabay and S. Rosenwaks, *Conf. on Lasers and Electro-Optics, OSA Technical Digest Series* 11: 456 (1993).

[2] S. Gabay, P. Blau, M. Lando, I. Druckman, Z. Horvitz, I. Yfrah, I. Hen, E. Miron and I. Smilanski, *Opt. Quantum Electron.* 23: S485 (1991).

[3] P. Blau, I. Smilanski and S. Rosenwaks, *J. Appl. Phys.* 72: 849 (1992).


## New Optical Technique for Corneal Refractive Surgery[1]


S. Gabay


The 193 nm wavelength produced by an Argon-Fluoride Excimer laser was found to make a sharp edge cut when the laser beam is focused on corneal tissue[2]. This interaction ablates the tissue and does not cause any thermal damage in the nearby area. Therefore, the

straightforward step was to adjust this technique for surface corneal tissue removal in order to reshape the anterior surface of the cornea to reduce myopia, hyperopia and astigmatism. However, this specific use is more delicate and needs a precise control means to form the original rectangular 'hot spots' laser beam into a circular cross-section intensity profile matched to perform the desirable refractive correction.

The commercial laser corneal sculpting systems include mechanical means[3] such as rotating beam prism, aperture wheels, ablated masks, etc., to achieve the right laser beam profile interacting with the cornea. These techniques cannot guarantee the predicted beam profile due to diffraction and scattering processes, and may leave the corneal surface with undesirable concentric graded zones.

At present, a new technique called 'adaptive optics' is being developed and seems to be promising in this area to overcome the disadvantages of the mechanical means. An adaptive mirror is a mirror attached to a matrix (or any other arrangement) of piezoelectric discs and controlling electrodes. Such a mirror is used to reflect the laser beam towards the cornea and the electrodes are actuated in such a combination to form any desired intensity distribution on the cornea. This technique has the potential to achieve precisely the predicted correction, leaving the corneal surface smooth and clean.

*References*

[1] S. Gabay, *10th Congr. Int. Soc. for Laser Surgery and Medicine* (Bangkok, Thailand, Nov. 1993).

[2] S.L. Trokel, R. Srinivasen and B. Braven, *Am. J. Ophthalmol.* 96: 710 (1983).

[3] P.R. Yoder, Jr., *Proc. SPIE* 1442: 162 (1990).

# III

# SOLID STATE AND NUCLEAR PHYSICS

## Investigation of P-p CdTe/HgCdTe Heterojunctions by Capacitance–Voltage Profiling[1]

V. Ariel*, V. Garber*, G. Bahir*, A. Sher and G. Cinader

In this study we used capacitance–voltage (CV) profiling techniques to study properties of isotype P-p CdTe/HgCdTe heterojunctions grown by the metal organic chemical vapor deposition (MOCVD) technique. A theoretical model suitable for analysis of graded heterojunctions was developed based on numerical solution of Poisson's equation. The model includes an approximate description of energy band nonparabolicity and carrier degeneracy. Also, a variable dielectric permitivity was included in the calculation of the valence band offset and the interface charge density. We employed procedures in crystal growth and device fabrication for both Schottky barrier and metal insulator semiconductor (MIS) structures. We demonstrated that the valence band discontinuity $\delta E_v \approx 0.15$eV and the fixed interface carrier density $\sigma_1 \approx (2\text{–}4)\cdot 10^{10}$ cm$^{-2}$. Also, we showed that carrier inversion is present at the CdTe/HgCdTe interface; this follows from both MIS and Schottky barrier device measurements and from a numerical simulation of the energy band structure. It seems that the inversion is responsible for the observed dependence of the CV measurements on temperature and frequency.

*Reference*

[1] V. Ariel, V. Garber, G. Bahir, A. Sher and G. Cinader, *Abstracts U.S. Workshop on the Physics and Chemistry of Mercury Cadmium Telluride and Other Materials* (Seattle, WA, USA, Oct. 1993).

## Stripe Structure CdTe-CdZnTe-CdTe in a Bulk Single Crystal[1]

M. Azoulay, M. Sinvani, M. Mizrachi and H. Feldstein

Both CdTe and CdZnTe single crystals exhibit high transmittance in the infrared region 1–30 μm, but differ significantly in their index of refraction. Thus, a stripe structure CdTe-CdZnTe-CdTe may be used as a light waveguide in the infrared region. An attempt was made to perform a selective diffusion of Zn into CdTe. A single crystal CdTe wafer was fabricated into a 'teeth-like' structure which was further subjected to high temperature annealing in the presence of Zn vapors. The sample was then cut parallel to the diffusion direction and a Zn concentration analysis was performed, using an electron microprobe analyzer. As expected, the stripe structure CdTe-CdZnTe-CdTe was confirmed. The Zn distribution profiles were

*Technion–Israel Institute of Technology, Haifa.

fitted to a modified diffusion model, suggesting a bulk diffusion mechanism coupled with a surface reaction. A practical implementation of this stripe structure for infrared light waveguide is being evaluated.

*Reference*

[1] M. Azoulay, M. Sinvani, M. Mizrachi and H. Feldstein, *J. Cryst. Growth* (1994, in press).

## An Observation of Nanotwin Lamellae in $Cd_{0.6}Mn_{0.4}Te$ Crystal by Atomic Force Microscopy[1]

M.A. George*, M. Azoulay, W.E. Collins*, A. Burger* and E. Silberman*

Atomic force microscopy (AFM) is used to examine the structure of freshly cleaved $Cd_{0.6}Mn_{0.4}Te$ surfaces. The present report complements previous results obtained with X-ray diffraction and optical microscopy which showed the existence of microtwins. The AFM analysis was performed under ambient conditions and yielded nanometer scale resolution images of single twin lamellae that ranged between 20 and 100 nm in width. This is a first observation using AFM of such a substructure, which we interpret as evidence for the presence of nanotwins.

*Reference*

[1] M.A. George, M. Azoulay, W.E. Collins, A. Burger and E. Silberman, *J. Cryst. Growth* 130: 313 (1993).

## Micromorphology Study of Mercuric Iodide Crystals by Atomic Force Microscopy[1]

M. Azoulay, M.A. George*, H.N. Jayatirtha*, Y. Biao*, A. Burger*, E. Silberman* and D. Nason**

Atomic force microscopy was used to study the surfaces of mercuric iodide crystals at ambient. Various surface conditions were examined, including as-grown (001), (110), and (013) faces, and cleaved, chemically etched, vacuum etched, and aged (001) surfaces. As-grown (001) faces show a terraced structure and are smoother than as-grown (110) faces.

*Center for Photonic Materials and Devices, Dept. of Physics, Fisk University, Nashville, TN, USA.
**EG&G Energy Measurements Inc., Santa Barbara Operations, Goleta, CA, USA.

Freshly cleaved surfaces exhibit a terraced structure, with riser heights corresponding to multiples of the *c*-lattice constant. All surfaces become progressively pitted and rougher by vacuum treatment or chemical etching. Defects identified as pits or hillocks with dimensions of the order of 100 nanometers were also observed, and surface roughness values were obtained for quantitative characterization of the various treatments.

*Reference*

[1] M. Azoulay, M.A. George, H.N. Jayatirtha, Y. Biao, A. Burger, E. Silberman and D. Nason, *J. Vac. Sci. Technol., B* 11: 1782 (1993).

## Surface Morphology Study of CdZnTe Single Crystals by Atomic Force Microscopy[1]

M. Azoulay, M.A. George*, A. Burger*, W.E. Collins* and E. Silberman*

The study of the crystal surface morphology of CdZnTe is important for the understanding of the fundamentals of crystal growth in order to improve the crystal quality which is essential in applications such as substrates for epitaxy or performance of devices, *i.e.*, room temperature nuclear spectrometers. We present here a first atomic force microscopy study of CdZnTe. Cleaved (110) surfaces were imaged in the ambient and an atomic layer step structure was revealed. The effects of thermal annealing on the atomic steps together with Te precipitation along these steps were considered in terms of deformation due to stress relief and the diffusion of tellurium precipitates.

*Reference*

[1] M. Azoulay, M.A. George, A. Burger, W.E. Collins and E. Silberman, *J. Vac. Sci. Technol., B* 11: 148 (1993).

*Center for Photonic Materials and Devices, Dept. of Physics, Fisk University, Nashville, TN, USA.

## Optical Properties and Surface Morphology Studies of Palladium Contacts on Mercuric Iodide Single Crystals[1]

M.A. George*, M. Azoulay, A. Burger*, Y. Biao*, E. Silberman* and D. Nason**

Palladium is chemically suitable for electric contacts on mercuric iodide detectors for photon and nuclear radiation, and therefore an understanding of palladium contacts is important for fundamental and practical scientific purposes. A study has been conducted of the surface morphology of evaporated contacts using Atomic Force Microscopy (AFM) and optical transmission and reflection. Evaporated palladium coatings are typically nonuniform and may deposit selectively on mercuric iodide surface defects. Reflection measurements show that coating thickness and the surface treatment affect the intensity, position and shape of a reflected peak characteristic of the mercuric iodide structure. Results indicate that the band gap energy at the surface of the mercuric iodide is reduced for palladium contacts.

*Reference*

[1] M.A. George, M. Azoulay, A. Burger, Y. Biao, E. Silberman and D. Nason, *Thin Solid Films* (1994, in press).

## Atomic Force Microscopy of Lead Iodide Crystal Surfaces[1]

M.A. George*, M. Azoulay, H.N. Jayatirtha*, Y. Biao*, A. Burger* and E. Silberman*

Atomic force microscopy (AFM) was used to characterize the surface of lead iodide crystals. The high vapor pressure of lead iodide prohibits the use of traditional high resolution surface study techniques that require high vacuum conditions. AFM was used to image numerous insulating surfaces in various ambients, with very little sample preparation needed. Freshly cleaved and modified surfaces, including chemical and vacuum etched, and air-aged surfaces, were examined. Both intrinsic and induced defects were imaged with high resolution. The results were compared with those from a similar AFM study of mercuric iodide crystal surfaces and it was found that, at ambient conditions, lead iodide is significantly more stable than mercuric iodide.

*Reference*

[1] M.A. George, M. Azoulay, H.N. Jayatirtha, Y. Biao, A. Burger and E. Silberman, *J. Cryst. Growth* (1994, in press).

---

*Center for Photonic Materials and Devices, Dept. of Physics, Fisk University, Nashville, TN, USA.
**EG&G Energy Measurements Inc., Santa Barbara Operations, Goleta, CA, USA.

## X-Ray Photoelectron Spectroscopy and Atomic Force Microscopy Characterization of the Effects of Etching $Zn_xCd_{1-x}Te$ Surfaces[1]

M.A. George*, M. Azoulay, H.N. Jayatirtha*, A. Burger*,
W.E. Collins* and E. Silberman*

X-ray photoelectron spectroscopy (XPS) was used to characterize the chemical composition of surfaces of $Zn_xCd_{1-x}Te$ single crystal and the chemical modifications resulting from etching them in bromine methanol. Variations observed in the XPS peaks indicated an increase of the tellurium and a depletion of the cadmium concentrations upon etching. Furthermore, it was observed that higher x values were correlated with a decrease in residual bromine left on the surface. High resolution images of these surfaces, obtained by atomic force microscopy, showed that cleaved $Zn_xCd_{1-x}Te$ surfaces were atomically flat while polished samples appeared to be rougher, indicating the formation of an amorphous layer. Etching of the cleaved samples revealed the formation of pronounced Te inclusions. Cut and polished samples had higher oxide concentrations and increased bromination of the surface than cleaved samples.

*Reference*

[1] M.A. George, M. Azoulay, H.N. Jayatirtha, A. Burger, W.E. Collins and E. Silberman, *Surf. Sci.* (1994, in press).

## Growth and Characterization of Pure Cr; Cr,Er and Cr,*Ho Codoped* $Y_2SiO_5$[1]

G.B. Loutts**, S. Hirnak**, T.T. Basiev***, M.E. Doroshenko***, V.B. Sigachev***,
Y. Shimony, C. Deka**, X.Y. Zhang**, A.B. Villaverde**, M.A. Bass** and B.H.T. Chai

The Czochralski crystal growth of pure Cr, Er and Ho doped as well as Cr,Er and Cr,Ho codoped yttrium silicate $Y_2SiO_5$ (YSO) is reported. The growth conditions for producing the inclusion free single crystals of high optical quality were defined. Spectroscopic properties of the singly doped and codoped material at room temperature were compared. Energy transfer

*Center for Photonic Materials and Devices, Dept. of Physics, Fisk University, Nashville, TN, USA.
**Center for Research in Electro-Optics and Lasers, University of Central Florida, Orlando, FL, USA.
***General Physics Institute, Russian Academy of Sciences, Moscow, Russia.

processes from $Cr^{4+}$ ions to $Ho^{3+}$ and $Er^{3+}$ ions in YSO host were demonstrated for the first time.

*Reference*

[1] G.B. Loutts, S. Hirnak, T.T. Basiev, M.E. Doroshenko, V.B. Sigachev, Y. Shimony, C. Deka, X.X. Zhang, A.B. Villaverde, M.A. Bass and B.H.T. Chai, *Proc. SPIE* 1863: 70 (1993).

## $UCoNiGe_2$, Nonmagnetic Solid Solution of the *Antiferromagnets* $UCo_2Ge_2$ and $UNi_2Ge_2$[1]

M. Kuznietz, F. Bourée*, H. Pinto and M. Melamud

The compounds $UCo_2Ge_2$ and $UNi_2Ge_2$ crystallize in the body-centered tetragonal $ThCr_2Si_2$-type structure (space group I4/mmm) (Fig. 1a). Both order in the AF-I antiferromagnetic structure [with a wavevector k = (0,0,1)], with uranium moments along the tetragonal axis[2,3]. Two polycrystalline samples of $UCoNiGe_2$, an intermediate solid solution of these compounds, have been prepared under identical conditions and studied by X-ray and neutron diffraction. Both samples of $UCoNiGe_2$ crystallize in the lower-symmetry primitive tetragonal $CaBe_2Ge_2$-type structure (space group P4/nmm) (Fig. 1b). The cobalt/nickel distribution in the M = (Co,Ni) planes in both $UCoNiGe_2$ samples is not random, with Co:Ni ratios of 36:64 in the M2 planes, close to the U planes, and 64:36 in the doubly dense and distant M1 planes. The absence of magnetic order in $UCoNiGe_2$ down to ~10 K, is associated with its lower symmetry.

*Laboratoire Léon Brillouin (CEA-CNRS), Centre d'Etudes de Saclay, Gif-sur-Yvette Cedex, France.

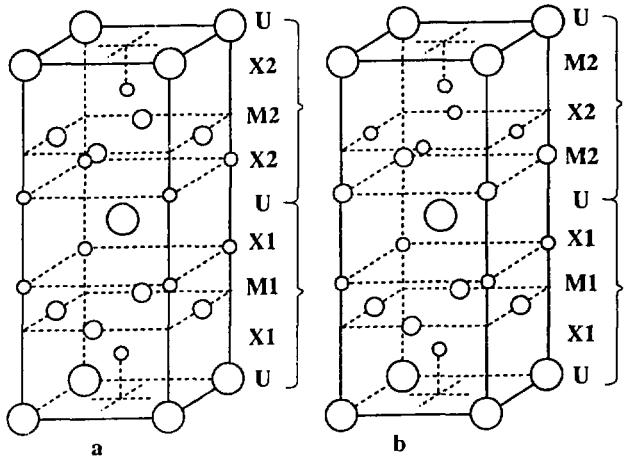


Fig. 1: Crystallographic unit cells of the $UM_2X_2$ compounds and solid solutions, with the 1 and 2 notation referring to identical atoms in the lower and upper half of the cell, respectively: (a) $ThCr_2Si_2$-type structure, space group I4/mmm, the most common in these materials (origin at 0 0 0); (b) $CaBe_2Ge_2$-type structure, space group P4/nmm, observed in the solid solution $UCoNiGe_2$ [origin of 1/4 1/4 3/4, to compare with (a)]. Planes marked 1 and 2 are crystallographically equivalent in (a) and nonequivalent in (b).

*References*

[1] M. Kuznietz, F. Bourée, H. Pinto and M. Melamud, *Solid State Commun.* 90: 93 (1994).
[2] M. Kuznietz, H. Pinto, H. Ettedgui and M. Melamud, *Phys. Rev., B* 40: 7328 (1989).
[3] M. Kuznietz, H. Pinto, H. Ettedgui and M. Melamud, *Phys. Rev., B* 48: 3183 (1993).

## Magnetic Ordering in $(U_{0.5}Tb_{0.5})Co_2Ge_2$, Studied by AC-Susceptibility and Neutron-Diffraction Measurements

M. Kuznietz, H. Pinto, H. Ettedgui and M. Melamud

The ternary compounds $TbCo_2Ge_2$ and $UCo_2Ge_2$ crystallize in the body-centered tetragonal $ThCr_2Si_2$-type structure. Both order antiferromagnetically, with the AF-I (+ - + -) structure [with a wavevector k = (0,0,1)] and (Tb or U) ordered magnetic moments along the tetragonal axis, below $T_N$ = 31 K for $TbCo_2Ge_2$ [1] and 175 K for $UCo_2Ge_2$ [2].

A polycrystalline sample of the intermediate solid solution of these compounds, namely $(U_{0.5}Tb_{0.5})Co_2Ge_2$, was prepared and found by X-ray and neutron diffraction also to have the $ThCr_2Si_2$-type structure with lattice parameters a = 3.998±0.010 Å, c = 10.014±0.020 Å, intermediate to those in $TbCo_2Ge_2$ and $UCo_2Ge_2$.

An ac-susceptibility study at 20-295 K yields effective paramagnetic moment $\mu_{eff} = 7.3\pm0.5\ \mu_B$ (including probable cobalt contribution) and paramagnetic Curie temperature $\theta = -50\pm15$ K, and indicates two magnetic transitions at 80±10 K and 50±10 K.

Neutron diffraction measurements indicate random distribution of Tb and U atoms in the (U,Tb) sites (or planes). The magnetic structure observed by neutron diffraction at low temperatures is the AF-I, characterized by (U,Tb) planes stacked antiferromagnetically, with ordered magnetic moments along the tetragonal axis, as found in the $TbCo_2Ge_2$ and $UCo_2Ge_2$. The calculated average ordered magnetic moment (at T ~ 10 K) per (U,Tb) atom in $(U_{0.5}Tb_{0.5})Co_2Ge_2$ is $4.05\pm0.03\ \mu_B$. Comparing this moment with the ordered moments $8.8\pm0.1\ \mu_B$, of terbium in $TbCo_2Ge_2$, and $1.50\pm0.2\ \mu_B$, of uranium in $UCo_2Ge_2$, ferrimagnetic (U,Tb) planes due to antiferromagnetic coupling of Tb and U moments are proposed, leading to the average moment observed. This model is to be studied further with other $(U,Tb)Co_2Ge_2$ solid solutions.

*References*


[1] H. Pinto, M. Melamud and H. Shaked, in: *Neutron Scattering - 1981*. AIP Conf. Proc. 89. J. Faber [Ed.] (New York, NY: AIP, 1982), p. 315.

[2] M. Kuznietz, H. Pinto, H. Ettedgui and M. Melamud, *Phys. Rev., B* 40: 7328 (1989).


## Magnetic Properties of $U(Ni_{1-x}Cu_x)_2Si_2$ Solid Solutions in the Vicinity of x = 0.50 Studied by Neutron Diffraction and AC-Susceptibility[1]


M. Kuznietz, G. André*, F. Bourée*, H. Pinto, H. Ettedgui and M. Melamud


The magnetic properties of two $U(Ni_{1-x}Cu_x)_2Si_2$ solid solutions in the vicinity of x = 0.50 (denoted I and II) have been studied by neutron diffraction and ac-susceptibility. Both materials have $ThCr_2Si_2$-type crystallographic structure. AC-susceptibility measurements showed antiferromagnetic transitions at $T_N = 150\pm5$ K in $UNiCuSi_2$ (I) and 155±5 K in $UNiCuSi_2$(II), followed by several transitions with ferro/ferrimagnetic (F) character at lower temperatures. Apart from the transitions to AF-I structure (+ - + -) at $T_N$ (150±1 K and 152±2 K, respectively), none of the F transitions is observed by neutron diffraction. Short-range magnetic order, involving several consecutive ferromagnetic planes or ferrimagnetic


*Laboratoire Léon Brillouin (CEA-CNRS), Centre d'Etudes de Saclay, Gif-sur-Yvette Cedex, France.

groups of planes in the AF-I phase, detected by ac-susceptibility and not by neutron diffraction in both materials and therefore significant to x ~ 0.50, is proposed to explain the unusual susceptibility.

*Reference*

[1] M. Kuznietz, G. André, F. Bourée, H. Pinto, H. Ettedgui and M. Melamud, *Solid State Commun.* 87: 689 (1993).

## Note on the Magnetism of $UCu_2Ge_2$[1]

M. Kuznietz, H. Pinto and M. Melamud

The results of a recent study and explanation of the magnetism of $UCu_2Ge_2$[2] do not agree with some previous results, notably neutron diffraction data[3,4]. The absence or appearance of a a low-temperature antiferromagnetic phase in this ferromagnet is ascribed to different annealing conditions that may give variations in stoichiometry, a view supported by neutron-diffraction studies of magnetic phase diagram of the $U(Ni_{1-x}Cu_x)_2Ge_2$ solid solutions[4,5].

*References*

[1] M. Kuznietz, H. Pinto and M. Melamud, *Philos. Mag. B* 68: 195 (1993).
[2] S.B. Roy and B.R. Coles, *Philos. Mag. B* 68: 195 (1991).
[3] M. Kuznietz, H. Pinto and M. Melamud, *J. Magn. Magn. Mater.* 83: 321 (1990).
[4] M. Kuznietz, H. Pinto, H. Ettedgui and M. Melamud, *Physica B* 180&181: 55 (1992).
[5] M. Kuznietz, H. Pinto, H. Ettedgui and M. Melamud, *Phys. Rev., B* 48: 3183 (1993).

## Neutron-Diffraction and AC-Susceptibility Studies of the $U(Ni_{1-x}Cu_x)_2Si_2$ System

M. Kuznietz, G. André*, F. Bourée*, H. Pinto, H. Ettedgui and M. Melamud

Polycrystalline $U(Ni_{1-x}Cu_x)_2Si_2$ solid solutions have the body-centered tetragonal $ThCr_2Si_2$-type crystallographic structure. Antiferromagnetic (AF) transitions, observed by ac-susceptibility for x = 0.10, 0.25, and 0.50, were confirmed by neutron diffraction. The AF structures were of type-I (+ - + -) with k = (0,0,1) below $T_o$ = 108±5 K for x = 0.10 (with a possible incommensurate phase at 108-135 K), $T_N$ = 151±3 K for x=0.25, and $T_N$ = 150±2 K

*Laboratoire Léon Brillouin (CEA-CNRS), Centre d'Etudes de Saclay, Gif-sur-Yvette Cedex, France.

for x=0.50. The ferrimagnetic transition observed by ac-susceptibility for x=0.75 arises from the coexistence of three magnetic phases: AF-I, ferrimagnetic (+ + -), AF-IA (+ + - -), with k = (0,0,1), (0,0,2/3), (0,0,1/2), and $T_N$ = 120±2, 115±4, 110±3 K, respectively. Including previous neutron results on $UNi_2Si_2$ single crystal[1] and powdered $UCu_2Si_2$ [2], the magnetic phase diagram of the $U(Ni_{1-x}Cu_x)_2Si_2$ system is proposed (Fig. 1).

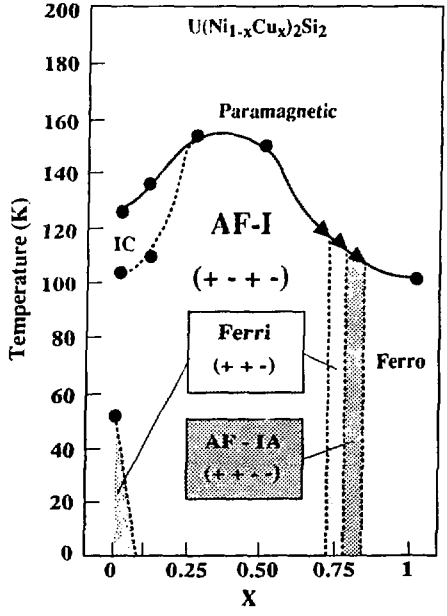


Fig. 1: The magnetic phase diagram (temperature *vs* composition, in zero applied magnetic field) proposed for the $U(Ni_{1-x}Cu_x)_2Si_2$ system. Most of the diagram is AF-I. The ferrimagnetic (+ + -) structure appears at two different regions. The IC phase at x = 0.10 is still to be confirmed. The exact x ranges of the phases (the transitions to which are denoted by arrowheads) for the material with nominal x = 0.75 are yet unknown.

*References*


[1] H. Lin, L. Rebelsky, M.F. Collins, J.D. Garrett and W.J.L. Buyers, *Phys. Rev., B* 43: 13232 (1991).

[2] L. Chelmicki, J. Leciejewicz and A. Zygmunt, *J. Phys. Chem. Solids* 46: 529 (1985).

# Coexistence of Three Commensurate Magnetic Phases in the Solid Solution $U(Ni_{0.25}Cu_{0.75})_2Si_2$, Observed by Neutron Diffraction

M. Kuznietz, G. André*, F. Bourée*, H. Pinto, H. Ettedgui and M. Melamud

A polycrystalline sample of the solid solution $U(Ni_{0.25}Cu_{0.75})_2Si_2$ was prepared and found to have the body-centered tetragonal $ThCr_2Si_2$-type crystallographic structure. The observation of a ferrimagnetic transition at 112±5 K by ac-susceptibility measurements, is confirmed by the neutron-diffraction observation, which also indicates the coexistence of three commensurate magnetic phases (Fig. 1). Two phases (40% each) are antiferromagnetic

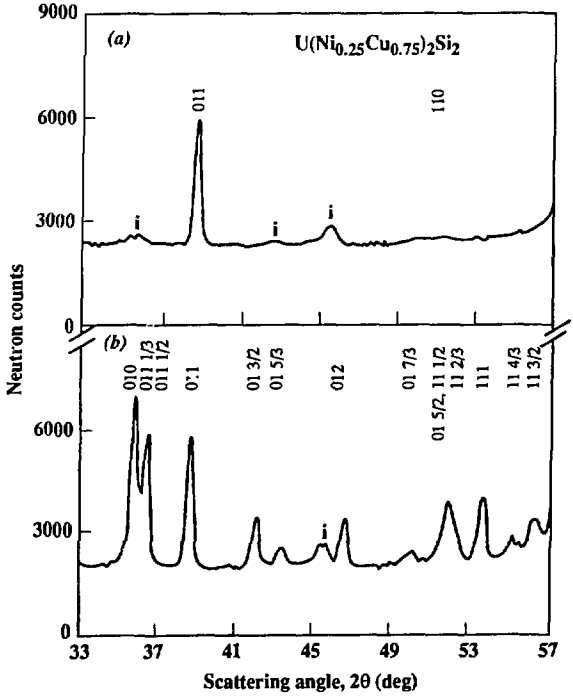


Fig. 1: Partial neutron ($\lambda$ = 2.444 Å at LLB) diffraction patterns ($2\theta$ = 33-57°) of a polycrystalline sample of $U(Ni_{0.25}Cu_{0.75})_2Si_2$: (a) at 130 K - depicting the {011} and {110} reflections of the $ThCr_2Si_2$-type major phase and three small impurity-phase reflections (denoted by 'i'); (b) at 1.5 K - showing additional magnetic reflections which can be classified into three sets:

1. {010}, {012}, {111};
2. {01(1/3)}, {01(5/3)}, {01(7/3)}, {11(2/3)}, {11(4/3)};
3. {01(1/2)}, {01(3/2)}, {01(5/2)}, {11(1/2)}, {11(3/2)};

pertaining to the coexisting AF-I, ferrimagnetic and AF-IA structures, respectively.

*Laboratoire Léon Brillouin (CEA-CNRS), Centre d'Etudes de Saclay, Gif-sur-Yvette Cedex, France.

(AF), and one is ferrimagnetic, 20% in volume: AF-I (+ - + -), ferrimagnetic (+ + -), and AF-IA (+ + - -), with wavevectors k = (0,0,1), (0,0,2/3) and (0,0,1/2), and $T_N$ = 120±2, 115±4 and 110±3 K, respectively. The temperature variation of the first magnetic reflection, combined from the first magnetic reflections of the three phases (Fig. 2), shows the different variation of these phases, with different $T_N$ values. The uranium ordered magnetic moments (2.2±0.1 μB at 1.5 K) are along the tetragonal axis in all three phases. These phases fit well into the proposed magnetic phase diagram of the $U(Ni_{1-x}Cu_x)_2Si_2$ system (see page 56) and are compared with the corresponding solid solutions in the parallel $U(Ni_{1-x}Cu_x)_2Ge_2$ system.

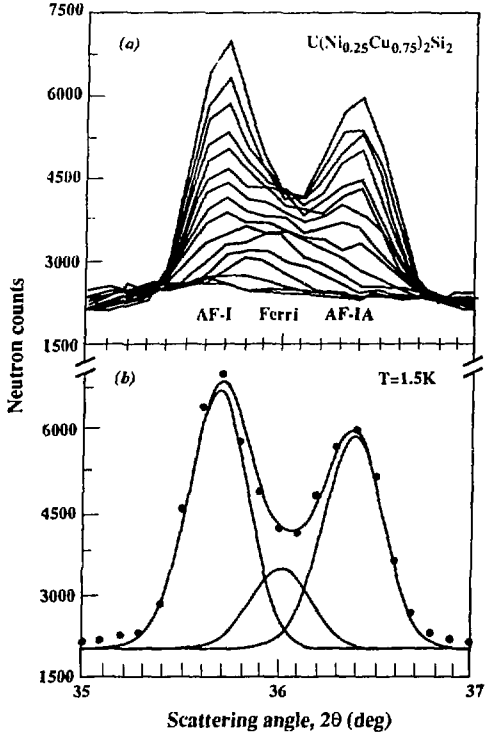


Fig. 2: The first combined magnetic reflection of the neutron (λ = 2.444 A) diffractogram (2θ = 35-37°) of $U(Ni_{0.25}Cu_{0.75})_2Si_2$: (a) at 1.5 K (top curve) and in the temperature range 71-130 K (curves decreasing, background rising with temperature), indicating different variations for the AF-I (+ - + -), ferrimagnetic (+ + -) and AF-IA (+ + - -) phases, the last one disappearing at $T_N$ = 110±3 K and the others – at higher temperatures, with a possible relative increase in the ferrimagnetic phase. (b) at 1.5 K, with the deconvoluted reflections.

## Defect Structure and Superconducting Properties of $La_{1.8}Sr_xCa_{1.2-x}Cu_2O_{6-\delta}$[1]

H. Shaked, J.D. Jorgensen*, B.A. Hunter*, R.L. Hitterman*,
K. Kinoshita**, F. Izumi+ and T. Kamiyama++

The relationship between structural defects and superconductivity in $La_{1.8}Sr_xCa_{1.2-x}Cu_2O_{6-\delta}$ ($0 \le x \le 0.8$) was studied. The samples were prepared by synthesis under different oxygen pressures $P(O_2) = 50$, 250, and 400 atm. Six of the seven samples were found to be superconducting with $22 \le T_c \le 58$ K. The structural properties were determined by powder neutron diffraction. The inter-$CuO_2$-plane spacing, $d_{Cu-Cu}$, increases as Ca on the M(1) site between these planes is replaced by the larger Sr and La ions. The metal-site ordering is influenced by the oxygen pressure during synthesis. The inter-$CuO_2$-plane spacing, the neutron-diffraction measurements of the scattering from the metal sites, and the chemical constraints were used to determine the occupancies of La, Sr and Ca at the M(1) site. For the same overall composition, higher oxygen pressure leads to a larger fraction of La on the M(1) site. Oxygen occupancy of the vacant O(3) site in the M(1) plane increases sharply when $d_{Cu-Cu}$ exceeds 3.5 Å. The superconducting transition $T_c$ decreases systematically as the occupancy of O(3) increases for samples that would otherwise be expected to be superconducting.

*Reference*

[1] H. Shaked, J.D. Jorgensen, B.A. Hunter, R.L. Hitterman, K. Kinoshita, F. Izumi and T. Kamiyama, *Phys. Rev., B* 48: 12941 (1993).

## New Analysis of Elastic Photon Scattering from $^{209}Bi$

S. Kahane

The experimental data of Dale *et al.*[1] on elastic photon scattering from $^{209}Bi$ were reanalyzed in view of a deficiency found in the original paper. A new set of GDR parameters was obtained for this nucleus. No evidence was found supporting larger than usual meson exchange currents in $^{209}Bi$, as was claimed by Nolte *et al.*[2,3]. The results are shown in Figure 1.

*Materials Science Division, Argonne National Laboratory, Argonne, IL, USA.
**Nippon Telegraph and Telephone Corp., Basic Research Laboratories, Musashino, Tokyo, Japan.
+National Institute for Research in Inorganic Materials, Tsukuba, Ibaraki, Japan.
++Institute for Materials Science, University of Tsukuba, Tsukuba, Ibaraki, Japan.

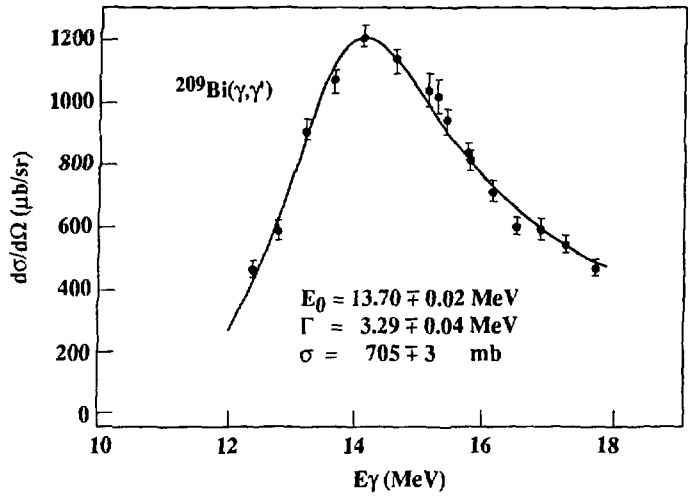


Fig. 1: Lorentzian fit to the experimental data of Dale *et al.*[1]. The new GDR parameters are given in the inset.

*References*


[1] D.S. Dale, A.M. Nathan, F.J. Federspiel, S.D. Hoblit, J. Hughes and D. Wells, *Phys. Lett., B* 214: 329 (1988).

[2] R. Nolte, A. Baumann, K.W. Rose and M. Schumacher, *Phys. Lett., B* 173: 388 (1986).

[3] R. Nolte, F. Schröder, A. Baumann, K.W. Rose, K. Fuhrberg, M. Schumacher, P. Fettweis and R. Carchon, *Phys. Rev., C* 40: 1175 (1989).


## Elastic Scattering Cross-Sections of 11.4 MeV Photons from $^{206,207,208}$Pb, $^{209}$Bi and $^{181}$Ta


S. Kahane and R. Moreh



Monoenergetic photons at 11.4 MeV, originating from the Ni(n,γ) reaction, were elastically scattered from three enriched isotopic lead targets, a $^{209}$Bi target and a $^{181}$Ta target. Cross-sections for the lead isotopes differ significantly from predictions based on known GDR parameters showing marked structures in this region of energy. The cross-sections for $^{209}$Bi and $^{181}$Ta are in agreement with a previous measurement. The $^{181}$Ta cross-

section is the only case where agreement is found with calculations based on known GDR parameters. The results are summarized in Table 1.

**Table 1**

**Summary of the present measurements (Elastic and Raman cross-sections in μb/sr)**

| Energy (MeV) | | Target | 140° | 90° |
|---|---|---|---|---|
| | | Based on natural Pb | | |
| | | $^{208}$Pb | 442±9% | |
| 11.4 | | $^{207}$Pb | 275±11% | |
| | | $^{206}$Pb | 254±11% | |
| | | Based on U standard | | |
| | | $^{208}$Pb | 459±13% | 289±14% |
| | | $^{207}$Pb | 286±13% | 179±14% |
| 11.4 | | $^{206}$Pb | 264±13% | 166±14% |
| | Elastic | $^{181}$Ta | 125±15% | 79[a] |
| | Raman to 9/2$^+$ | $^{181}$Ta | 27±32% | 26[b] |
| | | $^{209}$Bi | 230±13% | 145[a] |
| 10.05[c] | | $^{208}$Pb | 691±19% | |
| 10.05[d] | | $^{208}$Pb | 621±14% | |
| | | $^{208}$Pb | 22±22% | |
| | | $^{207}$Pb | 42±15% | |
| 9.0 | | $^{206}$Pb | | |
| | Elastic | $^{181}$Ta | 2.2±35% | |
| | | $^{209}$Bi | 9.7±16% | |

[a] Inferred from the value at 140° assuming $E1$ angular dependence: $1 + (\cos\theta)^2$.

[b] Inferred from the value at 140° assuming the angular dependence: $13 + (\cos\theta)^2$.

[c] Based on present $^{208}$Pb spectrum. Cross-section extracted relative to the 11.4 MeV result.

[d] Result taken from the work of Berant *et al.*[2]; reanalyzed in view of the present $^{209}$Bi cross-section and corrected to 140°.

*References*


[1] S. Kahane and R. Moreh, Submitted to *Phys. Rev., C.*

[2] Z. Berant, S. Kahane, R. Moreh and O. Shahal, *Phys. Rev., C* 31: 1533 (1985).


## Neutron Diffraction and Nuclear-Resonance Photon-Scattering Study of the $C_{24}K + N_2$ System[1]


*R. Moreh, H. Pinto, M. Melamud and H. Shaked*


$N_2$ gas physintercalated into $C_{24}K$ prepared from highly oriented pyrolytic graphite and the properties of the system were studied by neutron diffraction and nuclear-resonance photon

scattering. The identity period was determined before and after gas intercalation. The mosaicity of the system was destroyed by repeated intercalation and deintercalation of the gas.

*Reference*

[1] R. Morch, H. Pinto, M. Melamud and H. Shaked, *Mol. Cryst. Liq. Cryst.* (1994, in press).

## Evidence for Phase Transitional Behavior of Even-Even Nuclei from Differential Observables

A. Wolf, R.F. Casten*, N.V. Zamfir*,**,*** and D.S. Brenner**

Following recent discussions[1] of critical phase transitional behavior in nuclei, additional data were collected and used to test if there is further evidence to support such phenomena. Data from nuclear masses, radii, and E2 transition rates are used to construct differential observables. Inspection of these for the rare earth region shows that they exhibit the characteristic phase transitional behavior found in condensed matter and thermodynamic systems, namely, nearly constant values before the critical point, and a sharp change in the critical region, followed by a different (and, in general, varying) set of values after the critical point.

*Reference*

[1] R.F. Casten, N.V. Zamfir and D.S. Brenner, *Phys. Rev. Lett.* 71: 227 (1993).

## g-Factor of the $3/2^+$ 93.6 keV Level of $^{91}$Sr[1]

A. Wolf, R.L. Gill*, D.S. Brenner**, Z. Berant,
R.B. Schuhmann*,** and N.V. Zamfir*,**,***

The g-factor of the first excited, $3/2^+$, 93.6 keV level of $^{91}$Sr was measured using a beam of separated fission products and the time-differential perturbed angular correlation method in an external magnetic field of 3.85 T. The result, $g(3/2^+) = -0.231(11)$, is in good agreement

*Brookhaven National Laboratory, Upton, NY, USA.
**Clark University, Worcester, MA, USA.
***Institute of Atomic Physics, Magurele, Bucharest, Romania.

with the systematics of N=53-57 isotones, and with the predictions of the core-excitation model.

*Reference*

[1] A. Wolf, R.L. Gill, D.S. Brenner, Z. Berant, R.B. Schuhmann and N.V. Zamfir, *Phys. Rev., C* 48: 562 (1993).

## F-Spin Purity of $2_1^+$ States in Even-Even Nuclei[1]

A. Wolf, O. Scholten* and R.F. Casten**

The purity of nuclear states with respect to valence proton-neutron symmetry, expressed algebraically in terms of F-spin, has been the subject of several recent investigations. In general, it is widely believed that low-lying nuclear states have nearly maximal F-spin, $F_{max} = (N_p+N_n)/4$, *i.e.*, they are essentially symmetric with respect to valence protons and neutrons. However, some studies have indicated that deviations from this symmetry may exist. We present a procedure by which we can obtain estimates of the F-spin purity of $2_1^+$ states in even-even nuclei from the experimentally known g-factors of these states. The basic assumption we make is that the deviations of the experimental $g(2_1^+)$ values from theoretical predictions for completely symmetric states (which use 'bare' proton, neutron g-factors of 1 and 0), are due to $F < F_{max}$ admixtures in the $2_1^+$ states. With this assumption, the admixtures deduced in this work can be regarded as upper limits. IBA-2 numerical calculations were performed for 16 isotopes in the range Z=46-78. We found that the difference between neutron and proton boson energies considerably affects the calculated $g(2_1^+)$ values and the F-spin purity of the states, while not changing too much the energy level positions and the transition probabilities. For each isotope, we estimated the percentage of $F < F_{max}$ admixture required in the $2_1^+$ state in order to obtain agreement with the experimental $g(2_1^+)$. The results show a clear structure, which is related to the effective charges of protons and neutrons in the same isotopes.

*Reference*

[1] A. Wolf, O. Scholten and R.F. Casten, *Phys. Lett., B* 12: 372 (1993).

*Kernfysisch Versneller Instituut, Groningen, the Netherlands.

**Brookhaven National Laboratory, Upton, NY, USA.

# *IV*

# *MATERIALS SCIENCES*

## Analysis of Carbon Film Growth from Low Energy Ion Beams Using Dynamic Trajectory Simulations and Auger Electron Spectroscopy[1]

Y. Lifshitz, C.D. Roux*, K. Boyd*, W. Eckstein** and J.W. Rabalais*

Carbon film growth from low energy $C^+$ ions has been investigated by classical trajectory simulations using the dynamic TRIM code and by *in situ* surface analysis of the evolving layers using Auger electron spectroscopy. The calculations were performed for 30–300 eV $C^+$ ions impinging on Li, Si, Ni, and Au and experimental data for 150 eV $C^+$ ions on Ni are used for comparison. The simulations provide (i) concentration profiles of the carbon film, (ii) backscattering coefficients and sticking probabilities for the impinging $C^+$ ions, and (iii) sputtering yields of the composite films during deposition. The results of these simulations are in good agreement with the experimental profiles of the C and Ni concentrations as a function of $C^+$ fluence. The film growth mechanism which is in accord with these results is that of 'subplantation', in which the $C^+$ ions are deposited in subsurface layers and the outermost layer of substrate atoms is sputtered and diluted by successive impinging $C^+$ ions. The agreement between the experimental and calculated results supports the validity of the TRIM code and the binary collision approximation for 150 eV ions.

*Reference*

[1] Y. Lifshitz, C.D. Roux, K. Boyd, W. Eckstein and J.W. Rabalais, *Nucl. Instrum. Methods Phys. Res. B* 83: 351 (1993).

## Electron Energy Loss Spectroscopy of Mass Selected Ion Beam Deposited Diamond-Like Carbon[1]§

J. Kulik*, Y. Lifshitz, G.D. Lempert, J.W. Rabalais* and D. Marton*

Amorphous diamond-like carbon (DLC) films grown by low energy mass selected ion beam deposition were examined by electron energy loss spectroscopy (EELS). Films grown using deposition energies of 50, 120 and 300 eV were studied. For these deposition energies all films exhibit similar EELS characteristics, indicating a very high degree of $sp^3$ bonding. The bulk plasmon resonance is intermediate between that of graphite and that of diamond, but

*Dept. of Chemistry, University of Houston, Houston, TX, USA.

**Max-Planck-Institut für Plasmaphysik, Garching bei Munchen, Germany.

§This work was supported by ARPA MDA 972-90-J-001, the State of Texas through the Texas Center for Superconductivity at the University of Houston, Houston, TX, USA, National Science Foundation Grant DMR-8914608, USA, and U.S.–Israel Binational Science Foundation Grant 89-134, Israel.

the properties of the low energy loss spectra of the DLC films are more similar to those of diamond. The near K-edge carbon EELS data from the films exhibit a $\pi^*$ feature which is much smaller than that of graphite or evaporated carbon. The use of previously proposed computational methods on the near K-edge EELS data indicates that over 80% of the carbon atoms at $sp^3$ bonded. The size of the $\pi^*$ feature is larger for smaller plasmon energies, as expected. The present data are in accord with other analyses of similar films that indicate a broad (~ 30–300 eV) energy window for diamond-like film formation.

*Reference*

[1] J. Kulik, Y. Lifshitz, G.D. Lempert, J.W. Rabalais and D. Marton, *Submitted to J. Appl. Phys.*

## The Effect of Ion Energy on the Diamond-Like/Graphitic ($sp^3/sp^2$) Nature of Carbon Films Deposited by Ion Beams[1]

Y. Lifshitz, G.D. Lempert, S. Rotter, I. Avigal*, C. Uzan-Saguy*, R. Kalish*, J. Kulik**, D. Marton** and J.W. Rabalais**

Ion energy is known to be a crucial parameter in the determination of properties of films deposited by ion beams. Contradictory results regarding the optimal C ion energy for the deposition of diamond-like ($sp^3$-rich) carbon films have been reported: (i) about 20–40 eV by McKenzie *et al.*; (ii) about 100–200 eV by Ishikawa *et al.*; and (iii) about 100–700 eV by Hirvonen *et al.* These data are important both for establishing models of carbon film growth from ion beams and for practical film depositions.

In the present work pure carbon films were deposited at room temperature on Si using mass-selected $C^+$ ions covering the energy region 10–300 eV. Diamond-like properties were found for the entire energy region 30–300 eV. A transition to graphitic properties was observed for ion energies lower than 30 eV.

*Reference*

[1] J. Lifshitz, G.D. Lempert, S. Rotter, I. Avigal, C. Uzan-Saguy, R. Kalish, J. Kulik, D. Marton and J.W. Rabalais, *Diamond Related Mater.* (1994, in press).

*Technion–Israel Institute of Technology, Haifa.

**Dept. of Chemistry, University of Houston, Houston, TX, USA.

## Impact of Fiber Composite Laminate Plates: A Percolation View of Perforation and Spallation[1]

Z. Jaeger, M. Anholt and A.H. Mayer*

In a series of impact experiments on composite plates which were aimed at testing the conjecture that the perforation threshold represented a critical phenomenon and that Percolation Theory could eventually provide an adequate description of the spallation or fragmentation process accompanying the perforation of anisotropic layered materials, the fragments emerging from a 0/90 layup fiber epoxy plate target were collected and photographed. Image analysis techniques were used to deduce the size distribution of the backside fragments. It was found that the number N of fragments having area S may be represented as a power law $N \sim 1 / S^J$. The average exponent for the experiments which were performed at nine different values of impact velocity over the range from 300 to 6000 fps, had the value $J = 2.17 \pm 18\%$, which lies between the previously predicted theoretical values for Percolation Theory of J(2D) = 2.05 and J(3D) = 2.2. For the velocity $V_1 = 397$ fps, which is close to the perforation threshold velocity, J had the value 2.03, which is surprisingly close to the two-dimensional Critical Percolation Limit.

*Reference*

[1] Z. Jaeger, M. Anholt and A.H. Mayer, *Army Research Office Workshop on Dynamic Response of Composite Structures* (New Orleans, LA, USA, Aug.-Sept. 1993).

## Degradation of Polymers by Hyperthermal Atomic Oxygen

R. Vered, S. Matlis, G. Nahor [deceased], G.D. Lempert, E. Grossman, G. Marom** and Y. Lifshitz

Degradation of polymers by hyperthermal species (*e.g.* atomic oxygen [ATOX]) occurs in a variety of practical systems including external surfaces of spacecraft in low earth orbits, for which the impact with the residual ATOX (impact energy 3-7 eV) results in significant erosion. In the present work the effects of hyperthermal species on two polymers commonly used for space applications (Kapton H and Teflon FEP) were investigated. The polymers were exposed to 30 eV $O^+$ and $Ne^+$ fluences of $10^{15} - 10^{19}$ ions/cm$^2$. The phenomena investigated included total mass loss and changes of surface morphology (SEM and AFM) and surface

*Wright Laboratory, Flight Dynamics Lab., Wright-Patterson Air Force Base, OH, USA.

**Hebrew University of Jerusalem, Jerusalem.

chemical composition (XPS). The relative significance of the collisional and chemical degradation processes was evaluated by comparing the effects of $O^+$ and $Ne^+$ bombardment. AFM analysis was found to be very powerful in studying the damage from its initial atomic scale (roughness ~ 1 nm) to its final macroscopic scale (roughness > 1 μm).

## Structure of Grafted Polymeric Brushes in Solvents of Varying Quality: A Molecular Dynamics Study[1]

G.S. Grest* and M. Murat

A molecular dynamics simulation of polymeric brushes in solvents of varying quality was done. The resulting equilibrium structures were compared with those predicted by self-consistent field (SCF) analysis. The scaling of the brush height was found to agree with the SCF predictions at temperatures $T>T_\theta$, where $T_\theta$ is the θ temperature of the solvent. The agreement at $T<T_\theta$ is poor, probably resulting from the separation of the brush into monomer-rich and monomer-poor phases. This phase separation disappears with increasing grafting density and chain length. Good agreement is found with the SCF predictions for the density profile of the monomers and of the free ends of the chains and for the structure factor under good solvent conditions. The agreement of these properties with the SCF predictions at and below $T_\theta$ is not as good. Even the scaling behavior of the profiles with respect to the chain length and the grafting density was inconsistent with the SCF analysis. The effect of a small attractive surface interaction on the structure of the brush was also studied.

*Reference*

[1] G.S. Grest and M. Murat, *Macromolecules* 26: 3108 (1993).

## Radiation and High-Field-Induced Interface State Generation in MOS Structures with Modified Nitrided Oxide[1]

J. Shappir**, T. Roter** and J. Levinson

The incorporation of a controlled amount of nitrogen at the $Si–SiO_2$ interface for the purpose of increasing the gate oxide endurance to tunneling and hot electron injection has been the subject of many studies. In our work we obtained initial results on a novel structure

*Corporate Research Science Laboratories, Exxon Research and Engineering Company, Annandale, NJ, USA.
**Hebrew University of Jerusalem, Jerusalem.

of gate oxide with incorporated nitrogen at the interface, showing clear improvement as compared with standard thermal oxide both under tunneling electron injection as well as under exposure to ionizing radiation. Also studied was the combined effect of ionizing radiation following by tunneling injection. This may be of great importance for the use of non-volatile memories for space applications where they undergo programming and erase cycles after being exposed to ionizing radiation.

*Reference*

[1] J. Shappir, T. Roter and J. Levinson, *Microelectron. Eng.* 22: 219 (1993).

## Characteristics of Secondary Electron Emission from CsI Induced by X Rays with Energies up to 100 keV[1]

A. Gibrekhterman*, A. Akkerman, A. Breskin* and R. Chechik*

A microscopic model for low energy electron interaction in alkali halides was used to simulate secondary electron emission from CsI induced by X rays with energies up to 100 keV. The integral 'current' and 'pulse' yields were calculated as functions of the X-ray energy, CsI convertor thickness, and angle of incidence. We observed a decrease in true low energy (<50 eV) secondary electron yields at increasing X-ray energies and considered the effectiveness of CsI convertors coupled to gaseous electron multipliers developed for fast, high resolution X-ray imaging.

*Reference*

[1] A. Gibrekhterman, A. Akkerman, A. Breskin and R. Chechik, *J. Appl. Phys.* 74: 7506 (1993).

## New Insight into Proton-Induced Latchup: Experiment and Modeling[1]

J. Levinson, A. Akkerman, M. Victoria**, M. Hass*,
D. Ilberg, M. Alurralde***, R. Henneck** and Y. Lifshitz

A combination of irradiation experiments (using energetic protons and heavy ions) and a theoretical analysis was used, for the first time, to study proton-induced single event latchup

*Weizmann Institute of Science, Rehovot.
**Paul Scherrer Institute, Villigen PSI, Switzerland.
***Comision Nacional de Energia Atomica, Buenos Aires, Argentina.

(SEL) in electronic devices. A significant difference between SEL and single event upset (SEU) was found. For SEU the device sensitivity can be predicted by a model assuming the collection of the majority of the charge carriers generated in the sensitive volume by the nuclear fragments of the (*p*,Si) reactions. For SEL, the measured sensitivities are much lower than predicted by prompt charge collection. Recombination of charge carriers (generated by the heavier fragments) due to a track electric field reasonably explains the SEL data.

*Reference*

[1] J. Levinson, A. Akkerman, M. Victoria, M. Hass, D. Ilberg, M. Alurralde, R. Henneck and Y. Lifshitz, *Appl. Phys. Lett.* 63: 2952 (1993).

## *Track Effects and Their Influence on Heavy Ion Energy Losses in Semiconductor Devices*[1]

A. Akkerman, J. Levinson, D. Ilberg and Y. Lifshitz

The linear energy transfer (LET) concept is widely used in the context of single event phenomena (SEP) in electronic devices induced by energetic heavy particles and protons in space missions. Very recently several experimental results have shown that the LET concept may not be adequate for a quantitative evaluation of a variety of SEP. Stapor *et al.*[2] showed that different charge collection values in specially designed electron devices were obtained for ions having the same LET but different energies. At two recent conferences, Stassinopoulos[3] gave a critical analysis for the validity of the LET concept in SEP while Sigmund[4] discussed the relevance of the LET concept for secondary electron emission. There are also some indications of the failure of using LET as a measure in radiobiological investigations.

All these facts encourage attempts to understand the observed failures of the LET concept.

*References*

[1] A. Akkerman, J. Levinson, D. Ilberg and Y. Lifshitz, in: *Ionization of Solids by Heavy Particles*, R.A. Baragiola [Ed.] (New York, NY: Plenum Press, 1993), p. 431.

[2] W.J. Stapor, P.T. MacDonald, A.R. Knudson, A.B. Campbell and B.G. Glagola, *IEEE Trans. Nucl. Sci.* 35: 1585 (1988).

[3] E.G. Stassinopoulos and G.J. Brucker, *Proc. of RADECS 91* (Montpelier, France), 15: 3 (1991).

[4] P. Sigmund, in: *Ionization of Solids by Heavy Particles*. R.A. Baragiola [Ed.] (New York, NY: Plenum Press, 1993), p. 59.

## Changes in Surface Topography of FCC Metals Due to Helium Ions Bombardment[1]

D. Moreno, E. Abramov and D. Eliezer*

The interaction of energetic helium ions with solids, and possible consequent surface deformation, has been studied extensively due to its importance for the design of the first wall of fusion reactors. Studies of the buildup of surface damage on flat surfaces under helium irradiation reveal the development of a stochastic roughness due to the non-uniform removal of subtract materials by sputtering. The atomic collisions processes' response to surface layer sputtering may include mechanisms such as channeling and surface collision sequences.

The surface topography observed by a scanning electron microscope for copper and nickel bombarded with helium ions at different energies and doses was described, for both polycrystalline and single-crystal materials. Different topographic characterizations (symmetrical pyramid, rectangular-like roughness, etc.) were observed for the different samples. The correlation between the crystallographic orientation during irradiation and topographic characterization was considered.

For high irradiation doses, the effect of blisters' formation and surface flaking and exfoliation became dominant. Blisters' formation and growth were shown to depend on irradiation energy and dose, crystallographic orientation, and subtract materials properties. Irradiation temperature and post-irradiation thermal cycling were also found to affect surface topography.

*Reference*

[1] D. Moreno, E. Abramov and D. Eliezer, Submitted to *11th Int. Conf. on Plasma Surface Interactions in Controlled Fusion Devices* (Ibaraki-ken, Japan, May 1994).

## Synergistic Effect of Helium and Hydrogen on Copper Single Crystal[1]

D. Moreno and D. Eliezer*

The most suitable reaction in the nuclear fusion for energy production occurs between the two heavy isotopes of hydrogen, deuterium and tritium. Temperatures in excess of 100 million $^{o}$C will be needed in a reactor. At these temperatures the fuel is changed from a gas to a plasma. The products of the fusion reaction deuterium–tritium are helium-4, neutron and

*Ben-Gurion University of the Negev, Beer-Sheva.

energy. Structural materials in fusion reactors will be exposed to helium implantation over a broad range of energy, and to hydrogen isotopes (ions) in the plasma. The deformation and partial exfoliation of surface layers due to hydrogen and helium contribute to the total erosion of the first wall. For this reason, one of the most important factors in the choice of materials for the first wall of fusion reactors is the materials' resistance to damage. Helium clusters created by the fusion products are unable to escape from the nearest plasma surface and grow to dispersed bubbles, interconnected bubbles and finely formed blisters on the surface.

The plasma environment and the helium implanted in the vessel wall cause deterioration of the surface due to the synergistic effect. Recent advances in developing nuclear fusion reactors revealed that efficient heat removal from plasma-facing components is very important. Copper and copper alloys are considered an attractive choice for transporting such a high heat flux without thermal damage as they have high thermal conductivity.

In the present study of the effect of implanted helium and hydrogen charging, the following conclusions were drawn: *(a)* Surface oxides contamination, probably occurring during production, causes pitting on the surface by hydrogen charging, which is observed mainly on <111> preferred orientation surfaces; *(b)* He bombardment reduces the surface oxides and also the effect of hydrogen attack; and *(c)* the synergistic effect of hydrogen charging on He pre-implanted metals, significantly degrades the surface.

*Reference*

[1] D. Moreno and D. Eliezer, Submitted to *Scr. Metall.*

## The Source of Fringe Contrast Observed in the Interface between Helium Bubbles and a CuBe Alloy Matrix[1]

D. Moreno and D. Eliezer*

The implantation of helium in metals causes the formation of helium bubbles and creates an ordered array called a bubble superlattice. This phenomenon has been investigated widely, with the most extensive studies of the structural nature of the gas bubbles superlattice conducted for copper[2–4]. At low implantation temperatures, vacancies have only limited mobility. In this case, the bubbles are overpressurized and grow by an athermal process such as dislocation punching. The lattices of the arranged bubbles and the matrix of the host metal are oriented for diffraction along common planes but there is little understanding of the helium structure inside the bubbles. In theoretical studies, the calculated helium pressure reaches values that are consistent with solid state helium. As a result of the typical size of these implanted bubbles, there is no technique available to prove this statement.

*Ben-Gurion University of the Negev, Beer-Sheva.

The present work reports the observed contrast features at interphase interfaces by high resolution transmission electron microscopy. The principal features are interfacial dislocations by means of $\Delta\omega$ fringes[5]. $\Delta\omega$ fringes generally arise at interfaces having correlated lattices which are oriented for diffraction by common planes such that the deviation parameter $\omega$ is different for each crystal structure. The finite value of $\Delta\omega$ arises from a misfit between the host metal lattice around the bubbles and the helium structure. This misfit increases by the strain field created in the interface as a result of the bubbles' growth and displacement of the bubble interface. The observes $\Delta\omega$ fringes around the bubbles raise the possibility that the helium atoms are arranged in a specific structure, since the $\Delta\omega$ fringes are usually obtained by the interaction of two lattices at the interface.

*References*


[1] D. Moreno and D. Eliezer, *Sixth Israel Materials Engineering Conf.* (The Dead Sea, Israel, Feb. 1993).

[2] P.B. Johnson, A.L. Malcolm and D.J. Mazey, *Nature* 329: 316 (1987).

[3] P.B. Johnson, A.L. Malcolm and D.J. Mazey, *J. Nucl. Mater.* 152: 69 (1988).

[4] P.B. Johnson, A.L. Diprose (née Malcolm) and D.J. Mazey, *J. Nucl. Mater.* 158: 108 (1988).

[5] R.C. Pond, *J. Microsc. (Oxford)* 135: 213 (1984).


## $LaNi_5$ in a Copper Matrix


D. Moreno and I.R. Harris*


$LaNi_5$-based alloy absorbs and desorbs a large amount of hydrogen, either in a gaseous environment as a hydrogen storage or in an alkaline solution as a reversible hydrogen battery electrode[1–3].

Certain changes occur by exposition of $LaNi_5$ to hydrogen. The $\alpha/\beta$ transition by hydrogen absorption causes a 24% expansion in volume which leads to decrepitation of the metal into powder. Fine powder reaction beds have poor heat and mass transfer characteristics in addition to their unstable and incoherent structure. Proper processing can combine the useful properties of $LaNi_5$ compound metal with a matrix into one system, due to improvement of the formability of such a compound metal. However, powder metallurgy processes are not in thermodynamic equilibrium during initial fabrication of the powder, production of the compound, and sintering. Interdiffusion and reaction processes can create an interface reaction which seriously affects the $LaNi_5$ properties.

The reaction of $LaNi_5$ with Cu powder during sintering at high temperature was examined in order to obtain better conductivity and ductility. The $LaNi_5$ was sifted to 45 μm and mixed mechanically with 75 μm electrolyte copper powder to 10%, 30% and 50% $LaNi_5$


*School of Metallurgy and Materials, University of Birmingham, UK.

composition. The Cu–$LaNi_5$ mixed powder was induced to 2 bar hydrogenation at room temperature for a few hours and then heated at 240°C for 3 h to reduce the copper oxide by hydrogen reaction and recover the copper powder. The mixed powder was cold-pressed at 1000 MPA into pellets of cylindrical shape, approximately 1/2" diam. x 5.5 mm. Some of the pellets were forged at high energy for high density and reduced to 22" diam. x 1.6 mm coins, approximately. The forged and pressurized samples were heat-treated at 900°C for sintering and to improve the ductility of the samples. The samples were investigated by optical metallography, DTA (differential thermal analysis), XRD (X-ray diffractometry), TEM (transmission electron microscopy) and Micro-Probe analysis.

The pressurized and forged copper–10% $LaNi_5$ pellet was obtained with good integrity and without cracks, as opposed to the pellets containing 30% or 50% $LaNi_5$, which disintegrated partially during forging. Hydrogen absorption in the copper 10% $LaNi_5$ pellet was carried out at 10 bar and the capacity was examined by means of pressure changes in a calibrated volume chamber. The absorption obtained was approximately 80% of the calculated full capacity of the total amount of $LaNi_5$. The experiment was carried out for three consecutive cycles and most of the pellet was pulverized.

Pressurized and/or forged Cu–$LaNi_5$ with a higher concentration than 10% $LaNi_5$ is very brittle and cracks were obtained during the formation process. The need for heat treatment after pressuring and/or forging is vital to obtain a good diffusion bond of the copper particles and to improve the material strength. No interactions of La, Ni and Cu were observed after heating at 900°C but a very stable $La_2O_3$ phase was created around the $LaNi_5$ particles, especially for those containing more than 10% $LaNi_5$. Rolling up to 85% reduction showed good ductility.

*References*


[1] E.H. Kisi, C.E. Buckley and E.M. Gray, *J. Alloys Compounds* 185: 369 (1992).

[2] T. Sakai, K. Oguro, H. Miyamura, N. Kuriyama, A. Kato and H. Ishikawa, *J. Less-Common Met.* 161: 193 (1990).

[3] T. Sakai, H. Miyamura, N. Kuriyama, A. Kato, K. Oguro and H. Ishikawa, *J. Electrochem. Soc.* 137: 795 (1990).

# Blister Model Based on the Near-Surface Helium Concentration on Implanted Metals[1]

D. Moreno and D. Eliezer*

Blister formation due to the buildup of induced gas in the metal was investigated widely in diverse metals and alloys. However, there is no consensus as to the driving mechanism behind this phenomenon[2]. A new approach to blister formation has been discussed by means of the mathematical solution on a uniformly loaded circular plate with clamped edges[3,4]. It is generally accepted that blister formation depends strongly on the metal surface temperature, crystallographic orientation, and implantation parameters. In the present investigation we found that blister formation depends on the mechanical properties of the material and the near surface concentration of the implanted gas by means of the implanted atom stopping power.

Sample groups of copper polycrystal, single crystal in the principal directions <001>, <101> and <111>, and Cu-2Be-0.2Co after thermo-mechanical treatments in order to obtain different mechanical properties of the implanted metal. The surface morphology was analyzed by scanning electron microscope. Representative histograms were drawn up of the blister size distribution, based on a large number of micrographs. In almost all models, blister initiation starts from the excessive growth of large gas bubbles either by the agglomeration of clusters or by the coalescence of large gas bubbles and dislocation loop glide toward the surface. The present model is based on the fact that at certain depths from the surface, the pressure in the cavities approaches the yield stress of the metal and blistering starts. The thickness of the film depends on the mechanical properties of the specific metal. Once the blister cavity is formed, the deformation of the thin film into a blister cap depends on the buildup of the pressure in the cavity, which in turn depends on the implanted dose. In the present model, the thickness of the blister cap cannot be correlated with the projected range of the implantation as assumed by previous models. The helium concentration needed to build up a pressure to create a blister to a depth which is close to the projected range, is higher than the implanted helium concentration and the calculated critical pressure. Experimental results, such as that *(a)* the blisters burst at the edge of the circular skin, where the maximum stresses developed; and *(b)* at high implantation energy (large projected range) the bursting of the blisters occurs by multi-layer caps, support the present model.

*References*

[1] D. Moreno and D. Eliezer, Submitted to *Mater. Sci. Eng.*

[2] B.M.U. Scherzer, *Top. Appl. Phys.* 52: 271 (1983).

[3] D. Moreno, E. Abramov and D. Eliezer, *Scr. Metall. Mat.* 26: 277 (1992).

[4] D. Moreno, E. Abramov and D. Eliezer, *Scr. Metall. Mat.* 27: 1039 (1992).

*Ben-Gurion University of the Negev, Beer-Sheva.

## Surface Behavior of First-Wall Materials Due to the Synergistic Effect of Helium and Hydrogen Isotopes[1]

E. Abramov, D. Moreno, G. Solovioff* and D. Eliezer*

Scanning electron microscopy was used to investigate changes in surface morphology due to helium implantation and hydrogen charging. Pure polycrystalline nickel, OFHC copper and Cu-1.8Be-0.2Co (CAD 172) alloy were studied. The influence of helium implantation parameters on blister information and growth was investigated. Hydrogen charging (cathodic or thermal-gas) was found to lower the helium content needed for blistering and surface exfoliation. The effect of heating, carried out after hydrogen charging, was also studied.

For the copper samples, hydrogen damage was produced by oxide reduction at the oxide–metal interface. This damage was found to be lower when the sputtering due to helium implantation increased. The CuBe alloy showed a greater hydrogen resistance due to the stability of the surface BeO.

*Reference*

[1] E. Abramov, D. Moreno, G. Solovioff and D. Eliezer, *J. Nucl. Mater.* (1994, in press).

## Hydrogen Trapping in Nickel Pre-Implanted with Helium[1]

E. Abramov, G. Solovioff* and D. Eliezer*

The interaction of hydrogen isotope atoms with plasma facing components plays an important role in the fuel recycling of future thermonuclear fusion reactors. This paper summarizes earlier works that were conducted to study trapping and release of hydrogen isotopes in nickel pre-implanted with helium. Thermal desorption measurement analyzed by the simulation computer code DIFFER was used to evaluate trapping characteristics, *i.e.*, effective trapping energy and trapping efficiency. Emphasis was placed on the effect of helium content and post-implantation annealing on trapping behavior. The mechanism responsible for trapping of hydrogen isotopes atoms at or near helium bubbles was discussed.

*Reference*

[1] E. Abramov, G. Solovioff and D. Eliezer, *J. Nucl. Mater.* (1994, in press).

*Ben-Gurion University of the Negev, Beer-Sheva.

# The Influence of Preferred Crystallographic Orientation on Blister Size Distribution in Helium-Implanted Surfaces[1]

S. Zalkind, G.D. Lempert and D. Moreno

Blister formation by ion implantation has been attributed recently to the near-surface gas concentration and mechanical properties of the metal[2,3]. At a critical level of near-surface concentration, blisters are created with a typical range of diameter size for the specific material and specific implantation ion energy. Single crystal implantation with high near-surface He concentration has shown different typical blister sizes due to the crystallographic directions. Also, good correlation between experimental results on He ion implantation into Cu single crystal and blister formation explained by the Firsov model has been reported[2].

In the present work we report studies of blister formation in rolled and annealed aluminum and a Cu-1.8Be-0.2Co (CAD 172) alloy. Both rolled and annealed samples were implanted with 10 keV He ions for each of the selected doses. The Al samples were implanted with nominal doses of $3x10^{17}$, $4x10^{17}$, $5.5x10^{17}$ and $7x10^{17}$ ions/cm$^2$. The Cu-Be samples were implanted to a dose of $4x10^{17}$ ions/cm$^2$. The average implantation current density was 70 $\mu$A/cm$^2$. The implanted samples were analyzed by a scanning electron microscope and the blisters' size distribution was extracted from the micrographs.

X-ray diffractions performed before implantation show that the rolled Al has a <100> preferred orientation, while the annealed Al has mainly a <110> preferred orientation. The rolled Cu-Be has a <111> preferred orientation compared with the annealed Cu-Be, which has no preferred orientation at all. Comparison of the micrographs and especially the blister size distribution histograms shows a different blister formation behavior between the Al and the Cu-Be. It is clear that the blister diameters for the rolled Al samples are larger than those for the annealed Al ones, while the rolled Cu-Be blisters are smaller than the annealed Cu-Be blisters. It can be assumed that this behavior is related to the difference in the stopping power for different preferred crystallographic orientations of the grains. The stopping power of the implanted He ions was calculated using the Firsov model[4]. The data regarding the targets' properties and the blister size distribution are summarized in Table 1.

Table 1 shows that blister behavior depends strongly on the preferred orientation of the target and less on the mechanical properties. In both alloys, the rolled samples have a higher yield stress (compared with the annealed ones) but the blister size distribution behaves differently in both cases. In the aluminum, the blisters that were formed on the annealed samples were smaller than those that were formed on the rolled samples, while in the Cu-Be the smaller blisters were formed on the rolled ones. These results suggest that the blisters' behavior depends strongly on the stopping power which influences the near-surface gas concentration and on the ion implantation characteristics, and less upon the mechanical properties of the implanted metal.

Table 1
Samples' properties and blister size distribution for Al and Cu-Be

| Sample | Yield stress (MPa) | Preferred orientation | Stopping power (eV/Å | Main blister diameter (μm) |
|---|---|---|---|---|
| Rolled Al | 125 | <110> | 6.49 | 4.2 |
| Annealed Al | 28 | <100> | 6.72 | 3.7 |
| Rolled Cu-Be | 240 | <111> | 24.46[z] | 0.37 |
| Annealed Cu-Be | 190 | - | 19.64[y] | 0.45 |

[z] For Cu in the <111> direction.

[y] Calculated average value for the three main crystallographic orientations of Cu, given in ref. [2].

*References*


[1] S. Zalkind, G.D. Lempert and D. Moreno, *Scr. Metall.* (1994, in press).

[2] D. Moreno, E. Abramov and D. Eliezer, *Scr. Metall.* 26: 277 (1992).

[3] D. Moreno, E. Abramov and D. Eliezer, *Scr. Metall.* 27: 1039 (1992).

[4] O.B. Firsov, *Soviet Physics JETP* 36: 1076 (1959).


## An Electron Microscope Study of the Hydrogen Effects in Al–Ti/$SiC_p$ Metal Matrix Composites[1]


G. Solovioff*, E.J. Lavernia**, E. Abramov and D. Eliezer*


Al–Ti alloys are being studied as potential candidate matrix materials in metal matrix composites (MMCs) in an effort to increase further the alloys' modulus and strength. The extreme reactivity related to high additions of Ti, and the difficulties associated with the processing of MMCs, have prompted the development of alternate synthesis approaches. One such approach, spray atomization and deposition, is being studied as a result of its ability to rapidly quench, reinforce and consolidate in a single step, thus avoiding the difficulties associated with the handling of fine, reactive particulates. More detailed descriptions of the experimental apparatus and the processing parameters are described elsewhere. In the present study, spray-atomized, co-deposited and extruded Al–Ti/$SiC_p$ MMCs Transmission Electron Microscopy (TEM) was carried out on uncharged and charged samples in order to identify precisely the composition of the precipitates and to study the hydrogen effects on the morphology. The matrix and the precipitates were identified by a TEM-SAD pattern analysis. The Al matrix is composed of small (0.3–1.5 μm) equiaxed grains that surround the elongated $Al_3Ti$ precipitates.


*Ben-Gurion University of the Negev, Beer-Sheva.

**University of California, Irvine, CA, USA.

The results show that under severe conditions, such as exposure to NaCl solutions at cathodic charging conditions, initial crack propagation in Al–Ti/$SiC_p$ MMCs occurs without any applied stress. The matrix and the precipitates were identified by a TEM-SAD pattern analysis. Two classes of particulates were found in the specimen: 1-μm-wide and 3- to 5-μm-long acicular particles and 3 μm irregular SiCp. The SiCp are few in number. There are many more $Al_3Ti$ particulates, but both types are dispersed homogeneously.

In all of the samples investigated, hydrogen-induced cracks and voids at the reinforcement-matrix interface were present on the charged specimens. In comparison, these voids were never observed in uncharged specimens. A more detailed description of the experimental results was given in a previous study.

Therefore, it may be concluded that even in the absence of hydride formation, it is possible that local increased concentrations of hydrogen exist and assist in crack initiation and growth. It would appear that for the composite, there is always the possibility of preferential hydrogen accumulation at the large number of incoherent interfaces between the reinforcement particulates and the matrix.

*Reference*

[1] G. Solovioff, E.J. Lavernia, E. Abramov and D. Eliezer, *Proc. European Congr. on Electron Microscopy, EUREM 92* (Granada, Spain, Sep. 1992), vol. 2, p. 329.

## Characterization and Development of Foamy Rigid Polyurethane

M. Baruch

Polyurethane is a polymeric substance with a wide range of physical and mechanical properties which render it useful for many applications. The substance is produced from two liquid components, a base component (Polyol) and a catalyst component (Polyoscyanate), that are mixed to produce a solid substance. The product's characters are determined by the mixing ratio of the two components, the composition of the base component and the special additions to it, the homogeneity of the mixture, and the ambient temperature.

The solidification of the substance is rapid, with a rate between 30 and 180 seconds (depending on the ambient temperature). The solidification process is accompanied by emission of heat and gases.

This work was conducted, over the course of a year, to develop two types of rigid polyurethane. The achievements included the following developments:

- Production process in which stable characters of the polymeric substances are obtained;
- Production method for the substances;
- Production plant;

- Casting method of the liquid mixture into the casting mold.

It was necessary to develop at least two types of a polymeric foamy rigid substance. The characters of the developed substances agreed with the requirements and were tested according to the test standards specified in Table 1. The tests were conducted partly in our laboratories and partly in external laboratories.

**Table 1**
**Characters of the two substances developed**

| Substance characters | Substance A | Substance B | Test standard |
|---|---|---|---|
| Density ($kg/m^3$) | 60 | 106 | ASTM D1622 |
| Static strength parallel to the swelling (psi) | 68 | 150 | ASTM D1624 |
| Dynamic strength (psi) | 100 | 200 | |
| Elastic strength parallel to the swelling (psi) | 50 | 120 | ASTM D1623 |
| Gluing to metal strength (psi) | 50 | 120 | ASTM D1623 Method D |
| Fire resistance | 2 s to self-extinguishing, 30 mm burning length | 2 s to self-extinguishing, 30 mm burning length | FAR 25.853 |
| Bending strength perpendicular to foam swelling direction (psi) | 88.5 | 167.9 | ASTM D790 Method D |
| Thermal conductivity | 0.216 $\frac{BTU/h/ft^2}{°F \cdot in}$ | 0.266 | ASTM C518 |

The substance was developed with the help of an external plant and numerous tests were conducted until the required composition was achieved. There is a direct dependence between substance density and its bending and stress strength, as shown in Figure 1.

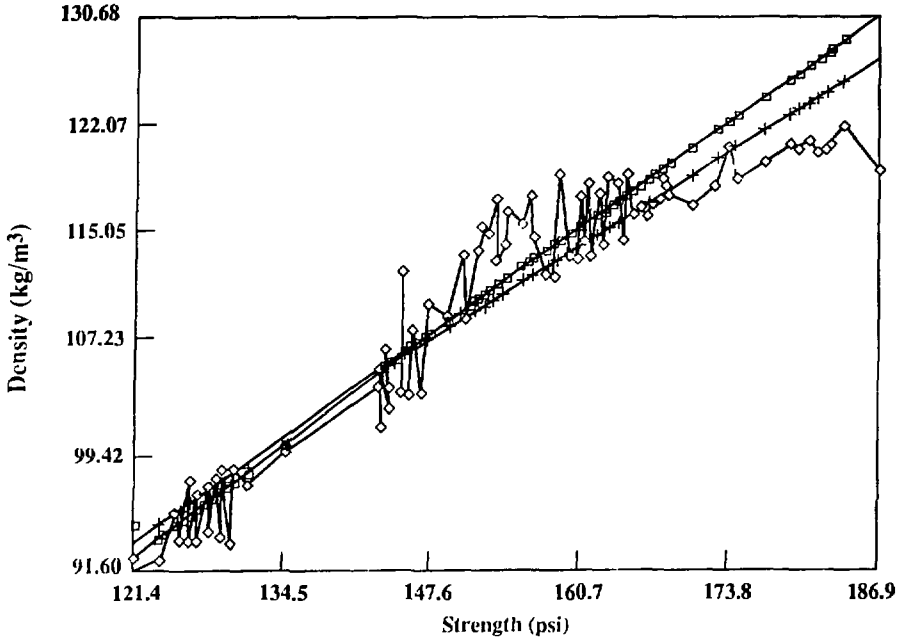


Fig. 1: Dependence between substance density and its strength.

## Etching of a-C:H Films by an Atomic Oxygen Beam[1]

E.B.D. Bourdon*, A. Raveh, S.C. Gujrathi** and L. Martinu**

Hydrogenerated amorphous carbon (a-C:H) films are considered for real-time monitoring of atomic oxygen in Low Earth Orbit, and during plasma etching processes. A-C:H layers were deposited onto quartz crystal microbalances (QCM) in a dual microwave/radio frequency (MW/RF) plasma in methane and methane/argon mixtures. The QCMs were exposed to a neutral atomic oxygen beam in a system simulating the space environment, using a flux of ~$10^{16}$ atoms/cm$^2$s at 2.5 eV average incident energy. The etch rate, $E_R$, was determined from the mass loss by *in situ* measurement of frequency shift of the QCM oscillator. The $E_R$ values, ranging from 1 ng/cm$^2$s to 20 ng/cm$^2$s, were found to increase with the hydrogen concentration in the films, and to decrease with increasing film density.

*Dept. of Physics and Astronomy, York University, North York, Ontario, Canada.
**Groupe des Couches Minces (GCM) and Dept. of Engineering Physics, Ecole Polytechnique, Montreal, Quebec, Canada.

Systematically higher $E_R$ values were found for a-C:H with a polymer-like character and for very hard diamond-like films with bonded hydrogen, in contrast to films with predominantly unbonded hydrogen. For comparison, $E_R$ values for crystalline CVD diamond and for several commercial polymers were also measured, and found to be ~0.5 and ~50 ng/cm$^2$s, respectively.

*Reference*

[1] E.B.D. Bourdon, A. Raveh, S.C. Gujrathi and L. Martinu, *J. Vac. Sci. Technol., A* 11:2530 (1993).

## Properties and Stability of Diamond-Like Carbon Films Related to Bonded and Unbonded Hydrogen[1]

L. Martinu*, A. Raveh, D. Boutard**, S. Houle*, D. Poitras*,
N. Vella*** and M.R. Wertheimer*

Hydrogenerated amorphous carbon (a-C:H) films with diamond-like characteristics have been deposited in dual-mode microwave-radio-frequency discharges in methane or methane-argon mixtures. Comparative measurements by elastic recoil detection and Fourier transform IR spectroscopy have been used to evaluate the amount of chemically bonded (IR-active) and unbonded (IR-inactive) hydrogen in the films. Three categories of structures have been distinguished: *(a)* hard hydrocarbon with hydrogen predominantly bonded; *(b)* hard hydrocarbon with hydrogen predominantly unbonded; and *(c)* a mixture of hard hydrocarbon and polymer-like phases. Film properties such as refractive index (1.8–2.5), resistivity ($10^{12}$–$10^{17}$ $\omega$ cm) and thermal stability (between 25 and 550°C) are correlated with the amount of bonded hydrogen.

*Reference*

[1] L. Martinu, A. Raveh, D. Boutard, S. Houle, D. Poitras, N. Vella and M.R. Wertheimer, *Diamond Rel. Mater.* 2: 673 (1993).

*Groupe des Couches Minces (GCM) and Dept. of Engineering Physics, Ecole Polytechnique, Montreal, Quebec, Canada.

**Laboratoire "Pierre Süe", CEN Saclay, Gif sur Yvette Cedex, France.

***ISTL, Université Montpellier II, Sciences et Techniques du Languedoc, Montpellier Cedex, France.

## Critical Ion Energy and Ion Flux in the Growth of Films by Plasma-Enhanced Chemical Vapor Deposition[1]

L. Martinu*, J.E. Klemberg-Sapieha*, O.M. Küttel**,
A. Raveh and M.R. Wertheimer*

Ion bombardment which occurs simultaneously with plasma-enhanced chemical vapor deposition (PECVD) of a growing film, enhances the material's characteristics such as density and adhesion, and enables the preparation of high quality films at low substrate temperature. In the present work, a dual-mode microwave (MW)/radio frequency (RF) plasma was used to control independently the energy and flux of the impinging ions. The samples are placed on an RF-biased (13.56 MHz) electrode, while being simultaneously exposed to the principal MW (2.45 GHz) discharge. We have determined critical average ion energy values, $E_{i,c}$, and critical ion/condensing-atom flux ratios, $(\phi_i/\phi_n)_c$, which are evaluated from transitions in the films' structure-related characteristics, *e.g.* density, microhardness, internal stress, resistivity, and dielectric loss. Different $E_{i,c}$ and $(\phi_i/\phi_n)_c$ values have been found for the various metals investigated, these being amorphous hydrogenated silicon dioxide [$SiO_2$, $E_{i,c}$ ~ 70 eV, $(\phi_i/\phi_n)_c$ ~ 0.26], silicon nitride [SiN, $E_{i,c}$ ~ 170 eV, $(\phi_i/\phi_n)_c$ ~ 0.60], and carbon with diamond-like properties [a–C:H, $E_{i,c}$ ~ 80 eV, $(\phi_i/\phi_n)_c$ ~ 0.28]. These results are interpreted in terms of a growth process model involving surface mobility of precursor species, and subplantation in hydrogen-rich surfaces. Ion bombardment at energies above $E_{i,c}$ has been found to account for a large portion of hydrogen in the films which is not chemically bonded.

*Reference*

[1] L. Martinu, J.E. Klemberg-Sapieha, O.M. Küttel, A. Raveh and M.R. Wertheimer, *J. Vac. Sci. Technol.* (1994, in press).

## Fourier Transform Infrared Photoacoustic Spectroscopy of Amorphous Carbon Films[1]

A. Raveh, L. Martinu*, A. Domingue*, M.R. Wertheimer* and L. Bertrand*

Phase Fourier Transform Infrared Photoacoustic Spectroscopy (PHAS-FTIR/PAS) can distinguish between surface and bulk chemical structure. In the present work, PHAS-

*Groupe des Couches Minces (GCM) and Dept. of Engineering Physics, Ecole Polytechnique, Montreal, Quebec, Canada.

**Dept. of Physics, University of Fribourg, Fribourg, Switzerland.

FTIR/PAS was applied to the study of hydrogenated amorphous carbon (a-C:H) films deposited in a dual microwave/radio-frequency plasma. It was found that spectra correlate well with the physico-chemical properties of a-C:H films.

*Reference*

[1] A. Raveh, L. Martinu, A. Domingue, M.R. Wertheimer and L. Bertrand, in: Photoacoustic and Photothermal Phenomena III. Springer Series in Optical Sciences. D. Bicanic [Ed.] (Berlin, Germany: Springer-Verlag, 1992), vol. 69, p. 151.

## Growth and Characterization of Ti:Sapphire[1]

A. Cohen, S. Biderman, M.P. Dariel, A. Horowitz,
M. Nahmani, M. Weiss and A. Ben-Amar

High quality Ti:Sapphire crystals of $\phi$ 32 x 150 mm were grown using a modified commercial Czochralski puller. The modifications included: a chamber compatible with high temperature (>2000°C) growth; and gas sealing of the puller in order to enable inert growth conditions. Post annealing in a reducing ambience was required to reduce further the residual $Ti^{4+}$ in order to obtain high quality Ti:Sapphire laser rods. Laser rods of $\phi$ 9 x 15 mm with Brewster angles were fabricated according to strict specifications.

Mechanical and optical characterizations were performed on the laser rods. Lasing experiments served as the ultimate test for quality of the Ti:Sapphire. The Ti:Sapphire rods were pumped longitudinally both by a copper-vapor laser and by a frequency doubled Nd:YAG laser. Pumping with a copper-vapor laser produced an output power of 3 W with a total efficiency of 25%. Pumping with the Nd:YAG laser produced an output energy of 20 mJ with a total efficiency of 35%.

*Reference*

[1] A. Cohen, S. Biderman, M.P. Dariel, A. Horowitz, M. Nahmani, M. Weiss and A. Ben-Amar, *Bull. Isr. Phys. Soc.* 39: 147 (1993).

## Copper Grain-Growth in Thin Film Cu-Cr Multilayers[1]

U. Admon, I. Dahan, M.P. Dariel, G. Kimmel, J. Sariel,
A. Shtechman, B. Yahav, L. Zevin* and D.S. Lashmore**

Copper-chromium multilayers with a 25 nm repeat distance were prepared by dual gun sequential magnetron sputtering. The mutual immiscibility of the two elements ensures that no interdiffusion or reaction takes place at the deposition temperature. High temperature X-ray diffraction runs were carried out in the 370-630°C temperature range, at constant time intervals. At elevated temperature, the Cu (*111*) reflection showed increasing intensity and decreasing line-width as a function of time. Analysis of the line narrowing as a function of the annealing time and temperature allowed us to deduce an activation energy, 0.41±0.05 eV/atom, associated with the atom mobility involved in the copper grain growth.

*Reference*

[1] U. Admon, I. Dahan, M.P. Dariel, G. Kimmel, J. Sariel, A. Shtechman, B. Yahav, L. Zevin and D.S. Lashmore, Submitted to *J. Thin Solid Films*.

## Critical Questions in Searching for Acceptable Margins against Failure[1]

Y. Katz

Establishing safety margins for high-risk structures has become a long-term goal associated with intensive efforts. Possible complexities emerged under different circumstances and life history, including various situations that raise critical questions and further concerns. The current study reviewed some aspects related to pressure vessel integrity with emphasis on the fracture mode transitions. Recent activities centered on the Ductile-Brittle Transition were described along with theoretical/experimental interfaces. Different origins for such transitions were illuminated by including temperature, plastic constraint, radiation or aggressive environmental effects. Generally, a physical view was adopted by means of crack tip dislocation activity models in high or low symmetry crystal structures. Systematic programs actually revealed the role of constitutive plastic properties and microstructure features. Deterministic and probabilistic aspects were analyzed, highly reflecting on fracture assessment methods. These were considered further mainly in the framework of elastic/plastic fracture mechanics.

*Ben-Gurion University of the Negev, Beer-Sheva.
**National Institute of Standards and Technology, Gaithersburg, MD, USA.

*Reference*
[1] Y. Katz, *ASME–Pressure Vessel and Piping Conf.* (Denver, CO, USA, July 1993).

## Shear-Like Transformation in Dilute U-W Alloys[1]

D. Dayan, O. Beeri, B. Herrmann, A. Landau,
A. Zahavi, Z. Livne and G. Kimmel

The uranium-rich side of the U-W binary system was studied using a conventional technique of optical microscopy, X-ray powder diffractometry, scanning electron microscopy and electron probe analysis. The solubility of tungsten in γ-uranium at 1060°C was found to be 1.0 at.% W. Uranium alloy containing 1.0 at.% W allows the retention of the γ-uranium structure at room temperature. In contrast to the U-Mo and U-Nb systems, the retention of γ-phase in the uranium-tungsten needs a smaller atomic percent which affects slightly its lattice parameter. A smaller addition of the order of 0.43 at.% W allows the retention of the β-uranium at room temperature as a metastable structure. The β-uranium decomposes by a complex martensite-like β→α transformation with isothermal characteristics into a strained but not distorted variant of the α-uranium structure.

*Reference*
[1] D. Dayan, O. Beeri, B. Herrmann, A. Landau, A. Zahavi, Z. Livne and G. Kimmel, *J. Alloys Compounds* (1994, in press).

## Enhancing XRPD Pattern Quality with Line-Profile-Fitting in Multiphase Systems[1]

G. Kimmel, J. Sariel, I. Dahan, S. Nathan and U. Admon

In the past, powder diffraction data were presented as d-I sets as obtained experimentally and systematic errors were utilized only for the derivation of the unit cell parameters. This attitude was justified by the fact that the major work of XRPD was done by a Debye-Scherrer camera and it was assumed that most users would obtain the same systematic errors. Today, diffractometry has taken over and the diffractometers have lower systematic errors, which can be minimized by calibration. Thus, they are now preferred. There are many phases which can be used as standards, but only four were selected, namely, Si, Ag, W, and mica (FP), which can easily be obtained as pure substances, have a limited number of diffraction lines, and a

good distribution of intensities along 2θ. The calibration is done by fitting a polynomial which correlates the standard experimental peak positions *vs* the expected (calculated) values. The more peaks which are used, the better the fit which can be achieved; on the other hand, using a standard with many peaks increases the probability of interference with the examined specimen peaks. Thus, it was decided to determine each line position by line profile fitting as recommended elsewhere. Similar methods have been used for structure analysis. In order to derive real observed data, we do not link the diffraction lines between themselves by global structural or line shape parameters. Thus, local variations in line profile parameters are treated. With the method suggested here, the final structural details (atomic positions) are not required. It was found that using the suggested method yields accurate unit cell parameters for each individual phase in the polyphase mixture. Several systems will be demonstrated in this work.

The given examples include phases which have high quality PDF files (ZnO and Ga). The results obtained in the current work are in very good agreement with these files. In the case of Ga, even though the peak positions found are in a good agreement with those in the PDF-file, the calculated cell parameters are somewhat different from those given in the PDF-file, and the current work modifies them. For the three other compounds, $EuGa_4$, $Al_4U$ and $Al_3U$, both the calibrated data and the cell parameters were modified significantly.

The method is fast and reliable. There is a potential to prepare accurate patterns, to determine unit cell parameters for new standards, and to revise inaccurate data.

*Reference*

[1] G. Kimmel, J. Sariel, I. Dahan, S. Nathan and U. Admon, *Adv. X-Ray Anal.* 37: (1994, in press).

## Characterization of TiN Film by XRD and XRF[1]

G. Kimmel, L. Politi* and T. Wieder**

TiAlN is a protective coating for cutting and reshaping tools, since it reduces wear, increases the cutting velocity of cutting tools, and extends the lifetime of reshaping tools. Thus, many investigators have studied the structure and properties of thin TiN films. Due to the complicated geometry of the tools, the coating thickness may vary at different locations on a tool. For quality assurance, thickness measurements are necessary. In this work – as a first step – only a simple geometry was considered. Using several methods to measure the TiN thickness allowed us to obtain an excellent cross-check of the results. Referring to the average values from XRD and XRF, both show linear growth of TiN *vs* sputtering time.

*Ben-Gurion University of the Negev, Beer-Sheva.

**FH Furtwangen, IIT, VS-Schwenningen, Germany.

The XRD film's thickness (between 0.6 and 3.0 mm) was higher than determined by XRF (0.4–2.0 mm). The film widths estimated from the metallography were closer to the XRD results, but the XRF results were more reproducible and smoother around the linear line. The fluctuations in the XRD results could be explained by the sensitivity to texture. The shift in the thickness values obtained from the XRF shows some systematic error. This could be due to sample displacement resulting in higher take-off angle. The correction factor for this displacement (up to 41%) can close most of the gap between XRF and XRD results.

*Reference*

[1] G. Kimmel, L. Politi and T. Wieder, *Adv. X-Ray Anal.* 37: (1994, in press).

# V

# CHEMISTRY

# Kinetics of the $B_2H_6/O(^3P)$ System at Room Temperature[1]

G. Gal and E. Bar-Ziv

An experimental study was made of the kinetics of the $B_2H_6/O(^3P)$ system at room temperature. Modeling was based on a multiple-parameter fitting process to a complex kinetic mechanism. The aim of the study was to propose and evaluate a preferred set of elementary reactions which might be important for the oxidation of boron-hydrides. In this study relative concentration-*vs*-time profiles of the radicals OH and $BO_2$ were measured in a low-pressure flow reactor, by the technique of laser-induced fluorescence. A range of almost two orders of magnitude in the initial fuel-to-oxygen ratio was covered, while the residence times of the gases in the reactor were up to 1 s. A comprehensive kinetic mechanism was constructed from the available measured and estimated data in literature. After the fitting process and dropping all of the reactions with negligible contribution, a 46 elementary reactions mechanism was obtained. In this mechanism, 27 reactions were not measured and their rate coefficients were used as the free parameters of the fitting process. Good agreement was obtained among all of the measured and calculated profiles. By sensitivity analysis it was found that only a limited group of these reactions contributes appreciably to the calculated concentrations of OH and $BO_2$. With only the strongly contributing reactions and all the oxygen-hydrogen reactions which are measured and relatively well known, a 30 elementary reactions mechanism was obtained. In this mechanism only 13 reactions are not measured and the agreement between the measured an the calculated profiles is still reasonable. To demonstrate the possible usefulness of the proposed mechanism, the rate coefficient of the reaction $B_2H_6+OH \rightarrow B_2H_5+H_2O$, which was not measured before, was directly measured in our experimental setup. The rate coefficient that was obtained in the direct measurement is $(3.3\pm1.1) \times 10^{11}$ $cm^3mol^{-1}s^{-1}$, in excellent agreement with the predicted one by the multiple-parameter-fitting process, which was $2\times10^{11}$ $cm^3mol^{-1}s^{-1}$.

*Reference*

[1] G. Gal and E. Bar-Ziv, Submitted to *Int. J. Chem. Kinet.*

# Observation of Non-Uniform Shrinkage and Activation of Highly Porous Chars during Combustion in an Improved Electrodynamic Chamber[1]

Y. Weiss*, D. Baum* and E. Bar-Ziv

The combustion of single particles of highly porous synthetic char was investigated in an electrodynamic chamber (EDC). The main reasons for using the EDC to study high temperature kinetics of single particles are: *(a)* the ability to sustain the particle without moving at all times at a known point; *(b)* to eliminate heat and mass transfer limitations; *(c)* to observe particle-to-particle differences; *(d)* the ability to characterize fully the particle prior to combustion; and *(e)* to monitor the important properties of the single particle through its entire combustion history. In this device the particle is heated radiatively by a focused laser ($CO_2$) beam to the desired temperature. During the heating the particle should not move by more than 1% of its diameter, since the waist of the beam is comparable to the particle diameter. A strong proportional–integral–derivative (PID) position controller was developed to maintain the particle at the center of the EDC with position stability better than 0.6% of its diameter. Further development of the EDC included real-time measurement of the particle shape and diameter with a temporal resolution of 0.1 ms, and infrared optical pyrometry with wide spectral bands that enabled us to determine the particle temperature to within ± 10 K. Oxidation of synthetic char particles (Spherocarb) was studied in the EDC at temperatures around 900 K. Transients of the particle weight, size, shape, temperature, and position of the particle were measured in real-time. Using the present EDC, the following phenomena were observed: (i) Prior to conversion, there was a stage at which mass loss or size change did not occur. This is attributed to activation of the char and was found to depend on the particle temperature. (ii) Non-uniform shrinkage during combustion: the initially spherical particles were consumed non-uniformly in all of the numerous experiments conducted. Eventually the spherical particle turned into a disk.

*Reference*

[1] Y. Weiss, D. Baum and E. Bar-Ziv, submitted to *Combust. Flame*.

*Ben-Gurion University of the Negev, Beer-Sheva.

## Processes in Highly Porous Chars under Kinetically Controlled Conditions: I. Evolution of Pore Structure[1]

I. Kantorovich* and E. Bar-Ziv

We present a model that describes the evolution of the pore structure of highly porous chars during oxidation under kinetically controlled conditions. A random pore structure, representing the pores by finite volumes, is applied. Two types of pores were considered: macropores and micropores. Macropores were represented by empty cylinders with distributions of finite lengths and radii. The micropore structure is the result of a highly dense network of solid microcrystals which are represented by microrods of cylindrical shape. These microrods are of equal radius and with a distribution of lengths. Reaction was assumed to occur mainly in the joints of the microrods. Three mechanisms for the evolution of the pore structure were considered: (i) The network of the solid microrods remains unchanged during reaction except for changes in the dimensions of the microrods. The microrods are shortened due to break-restoration of the interrod joints. (ii) Continuous coalescence and replacement of all microrods during reaction. (iii) The subskeleton of large microrods does not change during reaction except for the change in dimensions of their links; however, coalescence takes place for small microrods. Using these models, expressions for the apparent density, microrod dimensions, total surface area, and porosity were developed. Comparison with available experimental data validated mechanism (iii). Shrinkage is explained by the continuous process of break and restoration of the internal joints of the subskeleton of large microrods.

*Reference*

[1] I. Kantorovich and E. Bar-Ziv, *Combust. Flame* (1994, in press).

## Processes in Highly Porous Chars under Kinetically Controlled Conditions: II. Pore Reactivity[1]

I. Kantorovich* and E. Bar-Ziv

Most of the existing models do not deal with the change in the intrinsic reactivity during the evolution of the pore structure. Reactivity is believed to be in the micropores and it was usually assumed that the density of active sites on the internal surface does not change with time, *i.e.*, the intrinsic reaction rate is independent of conversion. The objective of the present work was to model the reactivity of the porous medium and to show the mutual influence of

*Ben-Gurion University of the Negev, Beer-Sheva.

the reactivity and the pore structure. Based on a previous study, reported in part I, above, a model for the change in concentration of the active sites is developed. Coalescence of the microcrystals of the porous network is considered to be the cause for this change. After every coalescence event, the number of active sites is assumed to increase stepwise. The influence of the history of the microcrystals on the generation factor of active sites is taken into account. The change in the density of the active sites located near the edges of microrods and at their circumferential surface is considered independently. The model calculations show the monotonic increase of the intrinsic reaction rate during conversion. The model successfully reconstructs the available experimental data on the consumption rates of highly porous chars.

*Reference*

[1] I. Kantorovich and E. Bar-Ziv, *Combust. Flame* (1994, in press).

## Influence of Acetate Ion on the Formation Reactions of Organochromium(III) Species. A Rapid-Scan and High-Pressure Pulse-Radiolysis Study[1]

W. Gaede*, A. Gerhard*, R. van Eldik*, H. Cohen and D. Meyerstein**

A UV/VIS rapid-scan technique was employed to study the formation of organochromium(III) species that are characterized by absorbance maxima at 321 and 412 nm. The effect of acetate on this formation reaction was studied, and spectral measurements demonstrated that it is mainly the monomeric chromium(II) acetate species that react with the alkyl radical, no involvement of the dimeric species being found. A high-pressure pulse-radiolysis technique was employed to study the effect of pressure on the formation of such complexes. The observed volumes of activation exhibit a decrease from +5.7 to -7.4 $cm^{-3}$ $mol^{-1}$ on increasing the acetate concentration from 0 to 0.27 mol $dm^{-3}$. Similar measurements in the presence of phosphate did not indicate any significant effect on the observed volume of activation for the formation of the metal-carbon bond. This difference can be interpreted in terms of the pressure dependence of the dimerization of chromium(II) acetate complexes, which was measured independently and exhibits a reaction volume of $+38 \pm 4$ $cm^3$ $mol^{-1}$. It is concluded that the mechanism of the formation of chromium carbon $\sigma$ bonds is not affected by anions such as acetate and phosphate.

*Reference*

[1] W. Gaede, A. Gerhard, R. van Eldik, H. Cohen and D. Meyerstein, *J. Chem. Soc., Dalton Trans.* 2065 (1993).

*Institute for Inorganic Chemistry, University of Witten/Herdecke, Witten, Germany.

**Ben-Gurion University of the Negev, Beer-Sheva.

## Anion-Catalyzed Heterolysis of Chromium-Carbon σ Bonds: Effect of Different Anions, Temperature, and Pressure[1]

W. Gaede*, R. van Eldik*, H. Cohen and D. Meyerstein**

The anion-catalyzed heterolysis reaction of $(H_2O)_5CrC(CH_3)_2OH^{2+}$ was studied as a function of anion concentration, temperature, and pressure for a series of ten different organic and inorganic oxy anions, for which the $pK_a$ values range between 0 and 7. The rate data indicate that the catalytic effect increases with basicity of the anion. The volumes of activation for the catalyzed heterolysis reactions were all significantly positive and supported the operation of a dissociatively activated heterolysis mechanism.

*Reference*

[1] W. Gaede, R. van Eldik, H. Cohen and D. Meyerstein, *Inorg. Chem.* 32: 1997 (1993).

## Free Radical-Induced Cleavage of Organic Molecules Catalyzed by Copper Ions: An Alternative Pathway for Biological Damage[1]§

S. Goldstein***, G. Czapski***, H. Cohen and D. Meyerstein**

Free radicals are responsible for many deleterious effects in biological systems. Several studies indicate that free radical reactions are involved in numerous diseases. However, little is known on the exact mechanisms by which free radicals cause damage in biological systems. The ability of oxy-radicals and aliphatic free radicals to damage biological molecules has been demonstrated by exposure of various metabolites to high energy radiation. Nevertheless, radiolysis is not the major source of free radicals produced *in vivo*, except under extreme circumstances, *e.g.* intentional and accidental exposure to high X-ray doses or to a high level of radioactivity. Four major types of free radicals are formed in biological systems: hydroxyl ($OH^{\cdot}$), superoxide ($O_2^{\cdot-}$), aliphatic ($R^{\cdot}$) and aliphatic-peroxo ($RO_2^{\cdot}$) radicals.

*Institute for Inorganic Chemistry, University of Witten/Herdecke, Witten, Germany.

**Ben-Gurion University of the Negev, Beer-Sheva.

§This work was supported by the GSF, Forschungszentrum für Umwelt Gesundheit, GmbH; the Israel Academy of Sciences and Humanities; and the Israel Atomic Energy Commission.

***Hebrew University of Jerusalem, Jerusalem.

Aliphatic free radicals of the type $^{-}CR^1R^2CR^3R^4X$ ($X = OH, CO_2^-, NH_3^+, OPO_3^{2-}$) react with both copper (II) and copper (I) complexes to form transients with copper-carbon σ-bonds. The copper (I) complexes are considerably more reactive towards aliphatic free radicals than copper (II) complexes.

The main route for the decomposition of these transient complexes occurs *via* β elimination of $X^-$, which ultimately causes the degradation of the aliphatic residue. The specific rates of the β-elimination processes depend on the nature of L, R and X. The results suggest that the rates are correlated to the C-X bond strength.

We suggest that analogous processes are responsible for some of the radical–induced deleterious effects found in biological systems in the presence of copper complexes.

*Reference*

[1] S. Goldstein, C. Czapski, H. Cohen and D. Meyerstein, in: *Bioorganic Chemistry of Copper*. K.D. Karlin and Z. Tyeklár [Eds.] (New York, NY: Chapman & Hall, 1993), p. 222.

## Effect of *N*-Alkylation on the Rate of β-Amine Elimination from Transients with $Cu^{II}$-Carbon σ Bonds[1]

S. Goldstein*, G. Czapski*, H. Cohen, D. Meyerstein** and S. Shaik*

The rates of β-amine elimination from $Cu^{II}-CH(CH_2NH_3)_2^{3+}$ and $Cu^{II}-CH_2CH_2NH_3^{2+}$ were found to be about two orders of magnitude lower than those from $Cu^{II}-CH[CH_2N(CH_3)_2H]_2^{3+}$ and $Cu^{II}-CH_2CH_2N(C_2H_5)_2H^{2+}$ in aqueous solutions. The results indicate that *N*-alkylation increases the rate of β-amine elimination, whereas previous results demonstrated that *O*-alkylation decreases the rate of β-elimination of HOR' from $(H_2O)_5Cr^{III}-CH_2CH_2OR'^{2+}$ (R' = H, $C_2H_5$). These opposite trends are in accord with expectations based on the assumption that the rate of β elimination of $X^-$ from $L_mM^{(n+1)}-CR^1R^2CR^3R^4X^{n+}$ is correlated with the C–X bond strength. A mechanism of activation from the reaction is formulated, based on the Shaik-Pross curve-crossing model. The model provides a basis for the assumption of bond strength controlled rates.

*Reference*

[1] S. Goldstein, G. Czapski, H. Cohen, D. Meyerstein and S. Shaik, *J. Chem. Soc. Faraday Trans.* 89: 4045 (1993).

*Hebrew University of Jerusalem, Jerusalem.

**Ben-Gurion University of the Negev, Beer-Sheva.

## β-Elimination and Related Reactions of Chromium(III)-Alkyl Complexes in Aqueous Solutions: Mechanistic Information from High Pressure Kinetic Measurements[1]

H. Cohen, R. van Eldik*, W. Gaede*, A. Gerhard*, S. Goldstein**, G. Czapski** and D. Meyerstein***

A systematic study of the effect of pressure on the decomposition rates of chromium(III)-alkyl complex *via* β-elimination was undertaken. It was found that the elimination of OR (R = H or alkyl) is characterized by a negative volume of activation, whereas the elimination of $NH_3$ exhibits a positive volume of activation. These values are interpreted in terms of early and late transition states, respectively. In addition, the decomposition *via* spontaneous heterolysis of $[(H_2O)_5Cr^{III}-CH_2CH(OH)_2]^{2+}$ and $[(H_2O)_5Cr^{III}-H]^{2+}$ was studied. The results, when compared with literature data, indicate that the volumes of activation for heterolysis also depend strongly on the intimate nature of the mechanism.

*Reference*

[1] H. Cohen, R. van Eldik, W. Gaede, A. Gerhard, S. Goldstein, G. Czapski and D. Meyerstein, submitted to *Inorg. Chem.*

## Ligand Interchange Controls Many Oxidations of Divalent First Row Transition Metal Ions by Free Radicals[1]

R. van Eldik*, H. Cohen and D. Meyerstein**

The volumes of activation of a series of reactions of the free radicals $\cdot CH_3$, $CO_2\cdot^-$, $Br_2\cdot^-$ and $(SCN)_2\cdot^-$, with several Mn(II), Fe(II) and Co(II) complexes, were determined. Previous data indicate that all the reactions studied proceed *via* the inner sphere mechanism. The results show that indeed the $\Delta V^{\#}$ values are similar to those reported for solvent exchange and complex formation reactions of these metal cations. Thus the results indicate that, mechanistically, these free radicals can be considered as nucleophilic attacking ligands. The $\Delta V^{\#}$ for the homolysis of the metal-carbon $\sigma$ bond in $(NTA)Mn^{III}-CH_3^-$ and $(NTA)Fe^{III}-CH_3^-$ is -4.0 and -0 $cm^3 mol^{-1}$, respectively. When compared with the $\Delta V^{\#}$'s for

*Institute for Inorganic Chemistry, University of Witten/Herdecke, Witten, Germany.
**Hebrew University of Jerusalem, Jerusalem.
***Ben-Gurion University of the Negev, Beer-Sheva.

analogous homolysis processes reported previously, the results suggest that the $\Delta V^{\#}$'s depend strongly on the metal-carbon bond strength.

*Reference*

[1] R. van Eldik, H. Cohen and D. Meyerstein, submitted to *Inorg. Chim. Acta.*

## Spectroscopic and Electrochemical Response to Nitrogen Monoxide of a Cationic Iron Porphyrin Immobilized in Nafion-Coated Electrodes or Membranes[1]

J. Hayon, D. Ozer, J. Rishpon* and A. Bettelheim

Nafion membranes containing immobilized Fe(III) tetrakis(N-methyl-4-pyridyl)porphyrin show spectroscopic changes in the UV/visible range after being exposed to gaseous NO, indicating the formation of a nitrosyl complex. Electroreduction of NO is mediated by this metalloporphyrin when immobilized in Nafion-coated glassy carbon electrodes. The use of these film electrodes for the amperometric determination of NO in aqueous solutions has also been demonstrated.

*Reference*

[1] J. Hayon, D. Ozer, J. Rishpon and A. Bettelheim, Submitted to *J. Chem. Soc., Chem. Commun.*

## Codeposition of Free Silicon during Chemical Vapor Deposition of Silicon Carbide

J. Yeheskel and M.S. Dariel

An experimental study was made of the factors influencing the concentration and distribution of elemental silicon codeposited during Chemical Vapor Deposition (CVD) of SiC from MTS ($CH_3SiCl_3$) and hydrogen diluted by argon. The experiments were in both hot- and cold-wall reactors at 1383–1423 K at atmospheric pressure. Codeposition of free silicon was detected even at very low excess hydrogen, contrary to the prediction of thermochemical calculations. In the hot-wall reactor, under conditions of high exchange rate of the feed gases, deposits of uniform composition were obtained, containing 0-90% free silicon, depending upon feed gas composition. The deposits of pure silicon carbide consisted

*Tel-Aviv University, Tel Aviv.

of β-SiC with a microhardness of 2400 kg/mm$^2$ at a typical formation rate of 30 μm/h. Microhardness decreased to 800 kg/mm$^2$ with increasing silicon concentration.

In the cold-wall reactor, under impinging gas flow conditions, non-uniform deposition occurs: a local gradient of Si/SiC is obtained with free silicon concentrations varying gradually between 0 and 35%.

Si/SiC ratios in the deposits were determined by a combination of XRD (X-ray diffractometry), scanning AES (auger electron spectroscopy) and SMP.

## One-Electron Oxidation Reactions of Azide Radicals with Some Purines in Aqueous Solutions: Guanine and Derivatives

M. Faraggi, J.B. Trent*, F. Broitman and M.H. Klapper*

Guanine, guanosine, deoxyguanosine and 5' GMP are oxidized by the $N_3^{\cdot}$ radical with rate constants (in $M^{-1}s^{-1}$) of ~ $3x10^9$ at pH > 11 and ~ $5x10^7$ $M^{-1}s^{-1}$ at pH 7. The kinetics of these radicals was followed. Guanine radical decays in a second-order rate constant. However, nucleosides and nucleotide radicals have shown at all pHs two consecutive processes (first order followed by a second order). The first order reaction is pH-dependent. Formation of a new transient was observed at pH ≥ 9 for guanosine, pH ≥ 11 for deoxyguanosine, and pH 13 for 5' GMP. The observed new transient spectra were similar to the spectrum observed for the guanine radical. This finding implies that the radiation-induced base release from nucleosides in alkaline solution is due to reaction of the nucleoside with $O^{-\cdot}$ rather than a $OH^-$-induced base release from the base oxidized radical.

## Application of Ionically Conductive Polymers of Perfluorosulfonic Acid Coatings and Membranes in Solid-State Electrochemistry[1]

R. Harth, D. Ozer, J. Hayon, R. Ydgar and A. Bettelheim

Electrochemistry in the absence of a contacting electrolyte solution, using ionically conductive polymeric perfluorosulfonic acid (Nafion) coatings and membranes, was reviewed. Various types of reference electrodes, including a polymer Ag/AgCl electrode and Ag directly sputtered on the Nafion membrane, were used. Voltammetry of model redox couples, such as potassium ferricyanide and various ferrocenes, was conducted in a solid-state configuration and compared with that obtained in aqueous solution. Dioxygen reduction catalyzed by an

*Dept of Chemistry, Ohio State University, Columbus, OH, USA.

electropolymerized metalloporphyrin with a Nafion film serving as a solid polymer electrolyte, shows similar features as observed using the modified electrode concept. However, catalysis of $O_2$ reduction in the presence of the cobalt (II) ammoniacal complex is more effective in the solid-state configuration. Dioxygen reduction in this case occurs 800 mV more positive than obtained in aqueous solution. New applications of solid-state electrochemistry are described in the fields of electrodeposition, monitoring of acidic gases and corrosion measurements.

*Reference*

[1] R. Harth, D. Ozer, J. Hayon, R. Ydgar and A. Bettelheim, Submitted to *Curr. Top. Electrochem.*

## On the Structure of Protonated Diamines and Polyamines[1]

Z. Karpas, S.E. Bell*, Y.-F. Wang*, M. Walsh* and G.A. Eiceman*

The reduced mobilities in air, at 200°C, of six isomeric $C_7H_{18}N_2$ protonated diamines, two triamines (caldine and spermidine) and two tetramines (thermine and spermine) were measured by ion mobility spectrometric (IMS) techniques. The results indicated that all these polyamines undergo proton-induced cyclization, with the proton forming a bridge between two amino groups. It appears that the favored configuration of the protonated polyamines involves a six- or seven-membered ring, rather than a bridge between the terminal amino groups. It is believed that in the tetramines the cyclic structure is formed between the two central, more basic, secondary amine sites.

*Reference*

[1] Z. Karpas, S.E. Bell, Y.-F. Wang, M. Walsh and G.A. Eiceman, *Struct. Chem.* (1994, in press).

## Ion Structure from Ion Mobility Measurements[1]

Z. Karpas, G.A. Eiceman*, M. Walsh*, Y.-F. Wang* and S.E. Bell*

The mobility of ions in the drift region of an IMS (ion mobility spectrometer) is affected by their mass, structure and internal charge distribution. Thus, mobility measurements are helpful in deducing inferences on ion structures. Polyamines are strong bases that readily protonate in the source of the IMS to form stable quasi-molecular ions. The mobility of six

*Dept. of Chemistry, New Mexico State University, Las Cruces, NM, USA.

protonated $C_7H_{18}N_2$ isomers indicates that they undergo proton-induced cyclization. Upon protonation, some naturally occurring triamines and tetramines were observed to favor formation of 5-, 6- or 7-membered rings over a structure that bridges the terminal amino-groups.

*Reference*

[1] Z. Karpas, G.A. Eiceman, M. Walsh, Y.-F. Yang and S.E. Bell, *Second Int. Workshop on Ion Mobility Spectrometry* (Québec, Canada, Aug. 1993).

## Towards Standard Reduced Mobility Measurements[1]

G.A. Eiceman*, Z. Karpas and C.S. Harden**

Compounds that readily form stable positive or negative ions were selected for an interlaboratory study, in order to compile a short list of the most suitable reference compounds for reduced mobility measurements. The best positive ion precursors were aromatic amines (substituted pyridine) and organophosphorus compounds. For negative ions, nitroaromatics were most suitable, as were halogenated compounds. Use of such reference compounds improves the reproducibility of reduced mobility measurements.

*Reference*

[1] G.A. Eiceman, Z. Karpas and C.S. Harden, *Second Int. Workshop on Ion Mobility Spectrometry* (Québec, Canada, Aug. 1993).

## Patent Documentation for an Ion Mobility Spectrometer[1]

R. Avida, M. Friedman, A. Matmor, Z. Karpas and O. Shahal

In an ion mobility spectrometer comprising a spectrometer tube with an ion shutter, an ionization source within a reaction chamber, and a drift chamber, the improvement comprises providing in or around the said drift tube a plurality of conducting segments, across which an electric field is applied, the said conducting segments being separated from one another by

*Dept. of Chemistry, New Mexico State University, Las Cruces, NM, USA.
**US Army Edgewood Chemical Research, Development and Engineering Center, Aberdeen Proving Ground, MD, USA.

insulating spacers, wherein the ratio between the width of the insulating spacers to the width of the conducting segments is between 2:1 and 1:1, preferably about 1.5:1.

*Reference*

[1] R. Avida, M. Friedman, A. Matmor, Z. Karpas and O. Shahal, *U.S. Patent No. 5,235,182* (1993).

## Ion Distribution Profiles in the Drift Region of an Ion Mobility Spectrometer[1]

Z. Karpas, G.A. Eiceman*, R.G. Ewing*, A. Algom*, R. Avida, M. Friedman, A. Matmor and O. Shahal

The radial distribution of ions at atmospheric pressure in the drift region of two ion mobility spectrometers of dissimilar dimensions was determined using a concentric ring detector, a detector with annulus design, and metallic and non-metallic blocking rings. The radial density profile of ions at the detector plate exhibited a maximum off-center beyond which ion density declined rapidly. The intensity at the center was roughly 40% less than the maximum, which to some extent reflects the ion density profile in the source. A hole in the detector plate center with diameter of 3 mm or less did not measurably affect ion intensities measured at the detector, while incremental enlargement of the hole caused a considerable decline in intensity. Finally, the radial broadening of the ions throughout their transit in the drift region suggested that diffusion alone could not account for the observed results.

*Reference*

[1] Z. Karpas, G.A. Eiceman, R.G. Ewing, A. Algom, R. Avida, M. Friedman, A. Matmor and O. Shahal, *Int. J. Mass Spectrom. Ion Process.* 127: 95 (1993).

## On the Structure of Water–Alcohol and Ammonia–Alcohol Protonated Clusters[1]

Z. Karpas, G.A. Eiceman*, C.S. Harden** and R.G. Ewing*

Collision-induced dissociation (CID) of protonated ammonia–alcohol and water–alcohol heteroclusters was studied using a triple quadrupole mass spectrometer with a corona

*Dept. of Chemistry, New Mexico State University, Las Cruces, NM, USA.

**US Army Edgewood Chemical Research, Development and Engineering Center, Aberdeen Proving Ground, MD, USA.

discharge atmospheric pressure ionization source. CID results suggested that the ammonia–alcohol clusters had $NH_4^+$ at the core of the cluster and that hydrogen-bonded alcohol molecules solvated this central ion. In contrast, CID results in water–alcohol clusters showed that water loss was strongly favored over alcohol loss and that there was a preference for the charge to reside on an alcohol molecule. The results also indicate that a loose chain of hydrogen-bonded molecules was formed in the water–alcohol clusters and that there appeared to be no rigid protonation site or a fixed central ion for clusters with eight or fewer molecules.

*Reference*

[1] Z. Karpas, G.A. Eiceman, C.S. Harden and R.G. Ewing, *J. Am. Soc. Mass Spectrom.* 4: 507 (1993).

## Qualitative and Quantitative Response Characteristics of a Capillary Gas Chromatograph/Ion Mobility Spectrometer to Halogenated Compounds[1]

Z. Karpas, Y.-F. Wang* and G.A. Eiceman*

The response of a capillary column gas chromatograph/ion mobility spectrometer (GC/IMS) system to chlorinated and brominated alkanes and alkenes in nitrogen, air and nitrogen/$CO_2$ mixtures was studied. Product ions were formed through dissociative electron capture processes or charge transfer reactions, yielding chloride or bromide ions. The quantitative response was shown to depend on the composition of the carrier gas in which atmospheric pressure ionization processes occurred as well as on the IMS cell temperature. Large variations in the quantitative response of the GC/IMS to different halogenated compounds were observed. The results were compared with those reported for the doped electron capture detector. Practical implications of the GC/IMS system as a monitor and detector for halogenated aliphatic compounds were considered.

*Reference*

[1] Z. Karpas, Y.-F. Wang and G.A. Eiceman, *Anal. Chim. Acta* 282: 19 (1993).

# Poly (Naphtho [2,3–*c*] Thiophene): Chemical Preparation and Nonlinear Optical Properties

B. Zinger, P. Shaier, Z. Kotler and A. Fein

Poly (naphtho [2,3–*c*] thiophene) was prepared in a three-step reaction from 2,3-dimethylnaphthalene through 1,3-dihydronaphtho [2,3–*c*] thiophene. The last step was oxidative polymerization. Several oxidants, such as ferric chloride, $NOBF_4$ and DDQ, were used as the polymerization agents. The polymers were characterized in their reduced (insulating) and oxidized (conducting) states. The polymers in their reduced state were soluble in common organic solvents. The oxidized polymers were soluble only in polar high-boiling-point solvents (DMF and N-methylpyrrlidinone). This indicates low-molecular-weight materials. The nonlinear optical transmission characteristics of polymer suspensions were studied at 532 *nm* and 1064 nm. The NLO activity in the shorter wavelength was found to be stronger.

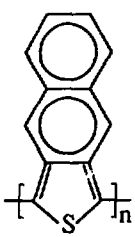


Fig. 1: Poly (naphtho [2,3–*c*] thiophene)

# *VI*

# *ENVIRONMENTAL STUDIES AND RADIOPHARMACEUTICALS*

## An Autonomous System for Seismic Sources Discrimination in Israel

G. Leonard, D. Mizrachi*, M. Joswig** and Z. Somer***

Artificial Intelligence (AI) techniques are increasingly incorporated in the management and control of industrialized processes. We introduce an autonomous seismic event classifier system for the discrimination between quarry blasts and microearthquakes in Israel. The essence of the AI approach is to imitate the seismologist's routine of the characterization of various event types by perception and reasoning. This system is an adaptation from the BUG array to a network configuration, integrating between the pattern recognition method and rule-based evaluation.

The new situation of 'stand alone' stations required two major changes from the original version: (i) the selection of independent master-event sets for every single seismographic station; and (ii) the adaptation of the rule-based evaluation to a network layout. The computer code may be used in two alternative modes, automatic or interactive with graphics support. The UNIX-based original version was adapted to an MS-WINDOWS version together with the upgrading of the human interface. The tested data included local seismic events from the Galilee area recorded by a sub-network in the time period May–July 1988.

The results of the pilot test yielded: 5% failure, 85% success and 10% no solution, for all cases where events came from predetermined sources. We found a direct correlation between success or failure and the quality of the signals. It was concluded that even better results could be achieved if the seismographic network were upgraded with respect to resolution, dynamic range and S/N ratio.

## The Use of Aircraft for Environmental Monitoring in Nuclear Accidents[1]

D. Skibin

During a nuclear accident a radioactive cloud is released into the atmosphere. It is transported and dispersed, its shape changes with time and space, and some of the radioactivity is deposited on the ground. These processes result from, and are influenced by,

*Tel-Aviv University, Tel Aviv.

**Lehrstuhl für Messtechnik RWTH Aachen, Germany.

***Tahal Consulting Engineers Ltd., Tel Aviv.

the 3-D dynamic structure of the flow and turbulence in the area; topography and the cloud's properties are additional major influencing factors.

We considered the dynamic evolution of the cloud in the atmosphere, the meteorological data needed for its prediction, and the role and schematic procedures of using aircraft in order to obtain the necessary information (meteorological, radiation and operational). The use of several different airborne platforms was contemplated (*e.g.* from manned aircraft and helicopters, through smaller remotely piloted aircraft, to engine-powered gliders). The relative benefits/disadvantages were considered, and suggestions were drawn up for international cooperation for developing/sharing/using such vehicles.

*Reference*

[1] D. Skibin, Presented at *Workshop on the Use of Aircraft in Atmospheric Research* (Braunschweig, Germany, March 1994).

## Applications of Collimated Airborne Monitoring in Radiological Emergency Response[1]

A. Pernick and H. Zafrir

Airborne monitoring is an accepted element of radiological emergency response, which enables tracking and mapping both the radioactive cloud and the ground contamination in real-time, and is of particular importance in the early phase of the response. Data acquired from airborne monitoring can be processed to give information regarding the isotopic composition and geometry of the cloud, which are essential input for real-time hazard prediction models.

The calculation of the source term based on airborne measurement of cloud radiation, necessitates a reliable estimation of plume geometry, as the horizontal and vertical standard deviations of the activity distribution ($\sigma_y$,$\sigma_z$) are parameters in this inverse calculation. Direct measurement of plume geometry is understandably more reliable than a 'handbook' estimation according to the Pasquil-Gifford stability state, due to the range of uncertainty of diffusion parameters and site-specific sensitivity. The limitation of airborne measurements of the plume and ground contamination is their resolution, which is determined by the relation between the angular range of the detector and the width of the activity distribution. An analysis was conducted of the efficiency of collimated airborne monitoring in the determination of the plume's geometric parameters ($\sigma_y$,$\sigma_z$), and in the determination of the ground contamination pattern.

The plume's geometric parameters ($\sigma_y$,$\sigma_z$) were determined as a function of the degree of detector collimation, height of flight relative to the cloud axis, atmospheric stability, and

downwind distance from emission. Calculations were performed for the isotopes Kr88, I131, Cs137 and Bal40, which were selected on the basis of release rates, photon energies and peak separations. The release rates of these isotopes are based on published estimations for the continuous release phase of the Chernobyl accident (Kr88, 9.8e+5 Bq/sec; I131, 3.94e+05 Bq/sec; Cs137, 1.57e+06 Bq/sec; Bal40, 7.14e+05 Bq/sec).

Peak (unscattered) photon fluxes arriving at the airborne detector were calculated by a computed program which stimulates the aircraft flight relative to the radioactive plume. The integral contribution of the plume to the measured photon flux for a given detector position on the flight line was calculated by a Monte Carlo method. The standard deviations of the plume activity distributions in the horizontal and vertical directions ($\sigma_y$,$\sigma_z$) were determined by fitting the calculated photon fluxes along the flight path to a normal distribution by the Levenberg-Marquardt non-linear regression method.

*Principal Results*

1. Uncollimated evaluation of $\sigma_y$ is sensitive to aircraft height, and there is a significant error for narrow activity distributions, characteristic of high atmospheric stability and relatively short distances from the emission. For example, there is a 50% error in the determination of $\sigma_y$ for the F stability state at a downwind distance of 2 km.
2. The horizontal crosswind activity distribution can be determined reliably by a collimated detector within a 200 m height range above the plume's upper edge. For an opening angle of $20^0$, higher flight heights result in a reduction of the photon flux to background levels, and for an opening angle of $45^0$, in decreased resolution and an overestimation of $\sigma_y$.
3. At downwind distances greater than a few kilometers, there is no significant resolution error in the evaluation of $\sigma_y$, due to the increased activity distribution width. However, the corresponding increase in vertical distribution imposes a limitation of non-penetration and necessitates exaggerated flight heights. Thus, the application of the airborne technique for determination of plume geometry is limited to a downwind range in which relatively narrow activity distributions necessitate collimation.
4. Evaluation of the vertical activity distribution ($\sigma_z$) by collimated monitoring and an ascending or descending flight path at a constant horizontal distance from the plume axis, was also found to be achievable within a 200 m range from the plume's edge. This evaluation is more limited to higher atmospheric stability and short downwind distance, due to the non-penetration criterion and the generally larger horizontal dimensions of the radioactive plume.

*Reference*

[1] A. Pernick and H. Zafrir, *American Nuclear Society Topical Meeting on Environmental Transport and Dosimetry* (Charleston, SC, USA, Sept. 1993).

## 'Winter Racing' of Upper Troughs in Summer[1]

D. Skibin and R. Newman

The beginning of September is considered summer in Israel. The Persian trough (at the low levels) and the subtropic high pressure ridge are the dominant systems. In the authors' experience, it is preferable to use the 700 mb chart (3 km height) to represent the upper level systems, rather than the 500 mb (5.5 km) map, during the summer. Using a fine-scale analysis of the 700 mb map, we discovered an astonishing effect. The upper air troughs moved at a very high speed, faster even than the usual speed during the winter. Such a case (5-8 September 1993) was analyzed. The trough moved 5-9 degrees longitude in 12 h (at 40°N latitude); the average travel speed was more than 12 m/s (approximately 45 km/h).

It is recommended to the forecasters to use a fine-scale analysis (10–20 m height interval and 1–2 degrees temperature interval) in order to follow the upper air structure, movement and changes during late spring, summer and early autumn (May–October) in the Middle East.

*Reference*

[1] D. Skibin and R. Newman, *Annual Meeting of the Israeli Meteorological Organization* (Shefayim, Israel, March 1994).

## Oxidation-Correlated Emission of Low-Molecular-Weight Organic Gases during Ambient Temperature Storage of Coal[1]

K. Sokolov*, S.L. Grossman*,**, S. Davidi* and H. Cohen

Israel started the burning of coal in power plants 13 years ago. Today *ca* 5.5 million metric tons of coal per annum are consumed. Bituminous coals are imported from South Africa, USA, Colombia and Australia. Stocks are kept at three storage facilities; two adjacent to power stations, and a third at the Ashdod Coal Terminal. The Port of Ashdod serves for the unloading of coal destined for the Ashkelon Power Station. The strategic piles hold *ca* 1,200,000 tons. Under storage the coal tends to undergo autogenous heating due to low temperature oxidation resulting in a loss in calorific value and weight, and the emission of fire-hazardous substances like carbon monoxide, low-molecular-weight hydrocarbons, molecular hydrogen, etc.

*Ben-Gurion University of the Negev, Beer-Sheva.

**National Coal Supply Corp., Tel Aviv.

The emission of organic gases and its correlation to the low temperature (55-95°C) oxidation processes were studied. The emission of methane was found to occur both in inert and oxidative (air) atmosphere. However, in air, there is an initial rapid process which is oxidation-correlated. All the other organic gases are not produced in inert atmosphere (argon) and are evolved in air. Two distinct processes were observed: (i) in the presence of oxygen a rapid reaction is involved; (ii) after all oxygen has been consumed, there is a much slower reaction. Ethylene emission involves only one reaction, and it occurs only in the presence of oxygen.

*Reference*

[1] K. Sokolov, S.L. Grossman, S. Davidi and H. Cohen, submitted to *9th Annual Symp. of the Israeli Section of the Combustion Institute* (Beer-Sheva, Israel, Dec. 1994).

## Emission of Fire-Hazardous Gases during Low-Temperature Oxidation of Coal Stored under Atmospheric Conditions[1]

H. Cohen, S. Davidi* and S.L. Grossman*,**

Large stockpiles of bituminous coal are stored under atmospheric conditions and undergo low-temperature oxidation resulting in a continuous loss in calorific value and weight. The main reactions occurring are oxygen chemisorption, formation of surface oxides and the emission of carbon dioxide to the environment. Coal stockpiles also tend to heat up in an autocatalytic process which promotes the emission of carbon monoxide, low-molecular-weight organic compounds and dihydrogen. Simulation studies in the laboratory showed that hydrocarbons and olefins up to $C_5$ are produced. A detailed investigation was concluded in which it was observed that, upon heating, all the coals studied (from South Africa, Colombia, Germany, Australia and USA) emitted the above organic products and dihydrogen. It was proved that the dihydrogen and ethylene are produced by an oxidation (chemisorption)-correlated process, whereas the saturated light hydrocarbons like methane and ethane are produced by a prepyrolysis ('sweating') process. The evolved gases may cause severe safety problems in confined spaces like ship holds and silos.

*Reference*

[1] H. Cohen, S. Davidi and S.L. Grossman, *Fuel* 73 (1994, in press).

*Ben-Gurion University of the Negev, Beer-Sheva.

**National Coal Supply Corp., Tel Aviv.

## Explosion Risks *via* Evolution of Molecular Hydrogen as a Result of Bituminous Coal Storage in Confined Spaces[1]

S.L. Grossman*,**, S. Davidi* and H. Cohen

Bituminous coals under low-temperature oxidation conditions (50-150°C) produce carbon dioxide and surface oxides. In addition, appreciable amounts of low-molecular-weight pollutant gases are produced by accompanying side-reactions. It has been observed that molecular hydrogen is one of these gases. The reaction producing the molecular hydrogen was investigated in detail. Labeling experiments showed that the source of the dihydrogen is C-H bonds within the structure of the coal macromolecule, and not moisture. A few possible reactions could be envisaged as the source of the molecular hydrogen produced. The amounts of hydrogen evolved are linearly correlated with the amount of oxygen consumed by the coal samples. The coal's ash content may serve as a catalyst for decomposition of some surface oxides to produce the dihydrogen at relatively low temperatures (> 50°C). The nature of the surface oxides which may, upon decomposition, lead to the emitted hydrogen as well as other possible reactions, was considered. The process of $H_2$ evolution was observed to be a general process accompanying the low-temperature oxidation of bituminous coals. In confined spaces the emission of hydrogen can increase appreciably the risks of explosions. Coal storage in confined spaces occurs in coal mines, ship holds, silos, etc.

*Reference*

[1] S.L. Grossman, S. Davidi and H. Cohen, in: *Energetische und Stoffliche Nützung von Reststoffen und Nachwachsenden Rohstoffen* (Welden, Germany: DGMK, 1994).

## Metribuzin and Metabolites in Wisconsin (U.S.A.) Well Water[1]

J.R. Lawrence***, M. Eldan and W.C. Sonzogni***

Metribuzin is a commonly used pesticide in Wisconsin and elsewhere, although contamination of groundwater by metribuzin has received little attention. A technique using solid phase extraction and high performance liquid chromatography was optimized to allow measurement of metribuzin and its major metabolites – deaminated metribuzin (DA),

*Ben-Gurion University of the Negev, Beer-Sheva.

**National Coal Supply Corp., Tel Aviv.

***Wisconsin Laboratory of Hygiene and Civil and Environmental Engineering (Water Chemistry Program), University of Wisconsin, Madison, WI, USA.

diketometribuzin (DK) and deaminated diketometribuzin (DADK). Percent recoveries and precision of metribuzin and DA analyses were good. Recoveries and reproducibility of DADK were acceptable (approximately 65%). However, the recoveries for DK were low (approximately 35%; the precision of the analysis was good, however). Overall, accuracy and precision were as good as, or better than, reported in the literature. Metribuzin and metribuzin metabolites were found in most of the groundwater samples analyzed from a number of wells located in sandy soil areas of Wisconsin. The parent metribuzin compound was found at concentrations ranging from not detected to 10.2 μg/*l*, while metabolite concentrations ranged from not detected to nearly 2 μg/*l*. Metabolites, which have been rarely reported to occur in water, were found in most of the samples even when the parent compound was absent.

*Reference*

[1] J.R. Lawrence, M. Eldan and W.C. Sonzogni, *Water Res.* 27: 1263 (1993).

## Changes in the Ascent Rate of the Pilot Balloon[1]

D. Skibin, E. Doron and R. Newman

Helium-filled pilot balloons are released within the framework of a study of the atmospheric boundary layer. The purpose is to supply data on the wind profile, and also as a carrier of a minisonde, that gives the temperature profile. During the preliminary phase of the research, a series of balloons were released and tracked using two remotely positioned theodolites. This method enables one to determine the balloon height accurately, without the need to assume a constant ascent rate.

The results of this series indicate that the average ascent rate does not agree with the equation appearing in the literature, which is routinely used in Israel. Preliminary analysis showed that the ascent rate changes within 0.9–1.3 relative to this equation. The ascent rate appears to change with the thermal stability of the surface layer. At night, the equation gives a reasonable fit to the data. During unstable, daytime conditions, the measured ascent rate is up to 30% higher than that measured by the equation.

A scheme is suggested in order to determine the average ascent rate that will enable the use of a single theodolite for pilot balloon tracking, with improved accuracy.

*Reference*

[1] D. Skibin, E. Doron and R. Newman, *Annual Meeting of the Israeli Meteorological Organization* (Shefayim, Israel, March 1994).

## Development of Radiation-Sterilized Mannitol Salt Agar Dip Slide Kits[1]

A. Stotland*, J. Bahar*, E. Eisenberg and S. Rubinfeld

Mannitol salt agar (MSA) used for isolation of pathogenic staphylococci was sterilized by gamma radiation, using a radiation dose of 15 kGy. The radiation-sterilized medium, modified by adding cysteamine, catalase and additional phenol red, performed as well as the commercial formulation prepared in the conventional way, when tested with different *Staphylococcus* species. Radiosterilized dip slide kits, containing MSA, functioned as well as those prepared by an aseptic filling process.

*Reference*

[1] A. Stotland, J. Bahar, E. Eisenberg and S. Rubinfeld, *J. Radiat. Steril.* 1: 5 (1992).

## $^{99m}$Tc-Teboroxime as an Alternative to $^{201}$Thallium for Myocardial Perfusion Imaging: Preliminary Study

J. Weininger, D. Friemark**, V. Guetta** and P. Chouraqui**

$^{99m}$Technetium teboroxime ($^{99m}$Tc-BATO) is a novel neutral lipophilic myocardial imaging agent. It is extracted by the myocardium with greater efficiency than $^{201}$Tl-chloride and $^{99m}$Tc-sestamibi over a broad range of flow rates. $^{99m}$Tc-BATO enjoys rapid myocardial uptake, and therefore myocardial visualization can be performed as soon as 1 minute post-injection. Myocardial washout is also rapid, about 6% per minute, so that a second imaging, after reinjection, can be performed without being affected by residual activity as early as 30 minutes after the first imaging.

Preliminary clinical studies have suggested that this tracer yields similar image quality to $^{201}$Tl, providing the images were taken rapidly enough after injection. With the goal of certifying $^{99m}$Tc-BATO as an alternative to $^{210}$Tl as a cardiac perfusion agent, a prospective study was undertaken in patients suspected or known to have coronary artery disease (CAD). A $^{99m}$Tc-BATO preparation developed by Soreq-NRC in lyophilized form, as a single vial kit with a one-year shelf-life, was used in this study. The contents of the vial were reconstituted and labeled by addition of up to 250 mCi $^{99m}$Tc-pertechnetate in 1–2 ml 0.9% sodium

*Hy Laboratory, Qiryat Weizmann, Rehovot.

**Heart Institute, Sheba Medical Center, Tel Hashomer.

chloride and heating in a boiling water bath for 15 minutes. Quality assurance testing showed high labeling efficiency (>95%). Since the labeled complex is stable for 6 h, the contents of one kit could provide both rest and exercise doses for three patients.

The patients were injected with 15–28 mCi $^{99m}$Tc-BATO followed by 20 ml of normal saline solution flush. The total amount of $^{99m}$Tc-BATO injected for both rest and stress activity per patient did not exceed 60 mCi. The continuous SPECT technique utilized in our protocol starts within 60 sec following injection for rest, 90 sec for effort imaging, and completion of imaging in the following 8 minutes.

In all patients standard $^{201}$Tl stress-reperfusion and rest and stress-reinjection $^{99m}$Tc-BATO SPECT imagings using a dynamic step and shoot acquisitions were performed within a 2-week interval using a single-detector camera. All patients successfully completed both studies without any significant side effects after radionuclide administration, and demonstrated concordant symptoms and ECG findings in the $^{201}$Tl and $^{99m}$Tc-BATO studies.

For $^{99m}$Tc-BATO imaging, the rest study preceded by 30–60 min either treadmill or dipyridamol stress and reinjection. Three complete studies were accomplished within 1.5–2 h. Comparison of findings between $^{201}$Tl and $^{99m}$Tc-BATO with respect to the presence and location of CAD showed concordance between the two sets of studies on a patient-by-patient basis in 16/17 patients. Both examinations independently detected an equal number of normal (10) and abnormal (6) images. There were two equivocal studies with both Tl and BATO in determining whether there was or was not CAD. There was no significant difference between the two agents in classifying lesions as ischemic, infarct and mixed anatomia (ischemia and infarction).

$^{99m}$Technetium-BATO SPECT imaging is clinically useful for detecting and evaluating CAD, its major advantage being the very short examination time needed per individual patient study: 8 min SPECT-image and 1–2 h total examination time (as compared with $^{201}$Tl: 20–25 min per examination and 4 h for stress + redistribution study). Overall, there was good correlation between $^{99m}$Tc-BATO and $^{201}$Tl studied for the diagnosis of normal and abnormal myocardial perfusion. $^{201}$Tl image quality was judged by both observers, independently, to be excellent in all 17 patients. With regard to the Tc-BATO images, there was no inter-observer variability as to the ratings for all the patients. However, as opposed to the $^{201}$Tl images, only 10 of 17 studies were rated to have excellent image quality. Of the remaining seven studies, four were judged to be good, two acceptable, and one of poor quality.

## Leukocyte Alkaline Phosphatase and Carcinoembryonic Antigen in Lung Cancer Patients[1]

N. Walach* and Y. Gur

Leukocyte alkaline phosphatase (LAP) scores in peripheral blood and plasma carcinoembryonic antigen (CEA) levels were determined in 58 lung cancer patients and compared with those of 22 healthy persons, who served as controls. In the control group we found LAP scores of 54±28 and CEA levels of 4±3 ng/ml. The 97.7% confidence intervals are: LAP score <110 and CEA level <10. In the patients with limited lung cancer we found LAP scores of 152±36.7 and CEA levels of 22.7±8.3 ng/ml. The 97.7% confidence intervals are: LAP score >78.6 and CEA level >0. In the patients with extensive lung cancer we found LAP scores of 272±49 and CEA levels of 47.5±80.4 ng/ml. The 97.7% confidence intervals are: LAP score >174 and CEA level >0. The sensitivity of each marker is considered, here as percent of false-negative results, denoted PFN, and meaning that with a chosen threshold for the marker level, only PFN% of the patients with a given condition (*e.g.* extensive lung cancer) might have a marker level less than the chosen threshold and could therefore be assumed healthy. The sensitivity of the LAP score is 0.05% PFN for the group of patients with extensive lung cancer, and we conclude that indeed LAP score <110 indicates a very low probability of having extensive malignancy. The sensitivity of the CEA level is 32% PFN. The sensitivity of the LAP score to limited lung cancer is 12% PFN for the group of patients with that condition compared with 40% of CEA. The specificities of both LAP score and CEA levels, expressed as percent of false-positive results in the control group, are fair (2.3%), provided that the common conditions, other than cancer, that elevate LAP score and/or CEA levels are well known and can be eliminated by the physician. It is concluded that the LAP score is considerably more useful than the CEA level as a marker for extensive lung cancer.

*Reference*

[1] N. Walach and Y. Gur, *Oncology* 50: 279 (1993).

## Control System Standards for the Pharmaceutical Industry

M. Arad, S. Milshtein, M. Hollander and J. Oren

A set of standards for control systems processes were developed and defined for Teva Pharmaceutical Industries Ltd. These standards include a set of instructions and definitions

*Assaf Harofeh Medical Center, Zerifin.

for the process designer, and a set of program blocks for the Programmable Logic Controller and the Man Machine Interface computer system. Each block is defined to meet the needs of a determined process block. The standards determine a framework for both the process designer and the control system designer, to simplify and unify the process design and its future maintenance. Standards are of special importance in the pharmaceutical industry, for which the Food and Drug Administration (USA) defines and requires validation and qualification. It is much easier to validate a system, the modules of which have been individually tested and shown to perform as expected.

## The Use of a Microwave Oven for $^{51}Cr$ (CrIII) Complexation Reactions

A. Freud and A. Canfi

$^{51}Cr$-EDTA injection is used in the determination of the glomerular filtration rate. $^{51}Cr$-chromic chloride injection is used for the determination of loss of serum protein in the gastro-intestinal tract. Both preparations are made by reduction of hexavalent $^{51}Cr$ to the trivalent state. The preparation of chromic chloride $^{51}Cr$ involves an overnight reaction at an acidic pH with an average yield of 90%. The latter is further complexed with EDTA to form $^{51}Cr$-EDTA.

This complexation reaction is extremely slow even upon heating. Heating the reaction mixture to 75–100°C for 3–4 h resulted in very poor yields of approximately 45% (ranging from 9.4% to 62.3%). In one experiment, the pH of the reaction mixture was neutralized with $NaHCO_3$ and the complexation yield was increased to 95%. However, this was achieved after boiling the reaction mixture for 4 h and increasing by twofold the molar concentration of the EDTA.

In an attempt to overcome the time-consuming process of heating, we replaced the water bath by a microwave oven (Brother Powerwave ER7341 microwave, 80-700 W, 2450 MHz). Heating was performed at a maximal output of 700 W. Each 'heating', which lasted 1 min, was composed of six 10-sec cycles in order to prevent spilling of the solution as a result of excessive boiling. The results of a typical process are presented herewith:

| Minutes of Heating | % Yield of Complexation |
|---|---|
| 1 | 12.0 |
| 2 | 27.9 |
| 4 | 39.3 |
| 5 | 39.7 |

The results indicate that short-time heating (minutes) results in a similar complexation rate which, formerly, was achieved only after hours of heating.

# VII

# RADIATION EFFECTS, DOSIMETRY AND PROTECTION

## Study of Single-Event-Upsets in PAL16R8[1]

J. Barak, J. Levinson, A. Zentner, D. David,
O. Even, M. Hass*, D. Ilberg and Y. Lifshitz

The susceptibility of an electron device to a single-event-upset (SEU) is a major factor in determining its suitability for space environments. Many devices have already been tested for their SEU vulnerability. The SEU cross-sections *vs* LET and *vs* ion-range of a PAL16R8 device were studied under different operating conditions and analyzed in view of the composite structure of the device. A remarkable difference is observed between inputs of '0's and '1's.

*Reference*

[1] J Barak, J. Levinson, A. Zentner, D. David, O. Even, M. Hass, D. Ilberg and Y. Lifshitz, *NSREC Workshop* (Snowbird, UT, USA, July 1993).

## A Portable Planar $^{90}$Sr Irradiation Setup for Total Dose Testing of Electronic Devices[1]

Y. Lifshitz, J. Levinson, Y. Noter, Y. Shamai, A. Akkerman,
O. Even, A. Zentner, M. Israeli, A. Gibrekhterman* and L. Singer**

A novel portable β irradiation setup (Fig. 1) using a planar $^{90}$Sr (β) source was designed. Calibration procedures, dose calculations and comparative study of $^{60}$Co and $^{90}$Sr irradiations of a specific device were developed.

Total dose effects in electronic devices are usually investigated by $^{60}$Co (γ) sources or by high energy (> 2.5 MeV) electron accelerators. These two irradiation facilities are characterized by a practically constant dose depth profile independent of the device shielding thickness and geometry for aluminum thicknesses of several mm. However, these facilities are very massive and require performance tests at specific sites. The use of a β source where heavy shielding is not required, enables us to overcome this problem. The newly designed non-conventional portable irradiation facility, which employs a planar $^{90}$Sr (β) source, enables testing under irradiation at the manufacturer's site. This approach is important in those cases where the manufacturer's sophisticated and expensive test station must be used.

*Weizmann Institute of Science, Rehovot.
**ISA – Israel Space Agency, Tel Aviv.

Furthermore, the planar $^{90}Sr$ source provides omnidirectional ($2\pi$) irradiation with 0–2.2 MeV electrons which offers a better simulation of the space radiation dose distribution than the conventional $^{60}Co$ sources and electron accelerators.

The present work included: (i) design and construction of the portable irradiation facility; (ii) accurate dosimetry of the irradiation field; (iii) theoretical calculations of the energy spectrum and dose distribution *vs* irradiation parameters (distance from source, depth of absorber); and (iv) comparison of $^{60}Co$ and planar $^{90}Sr$ irradiations of specific devices.

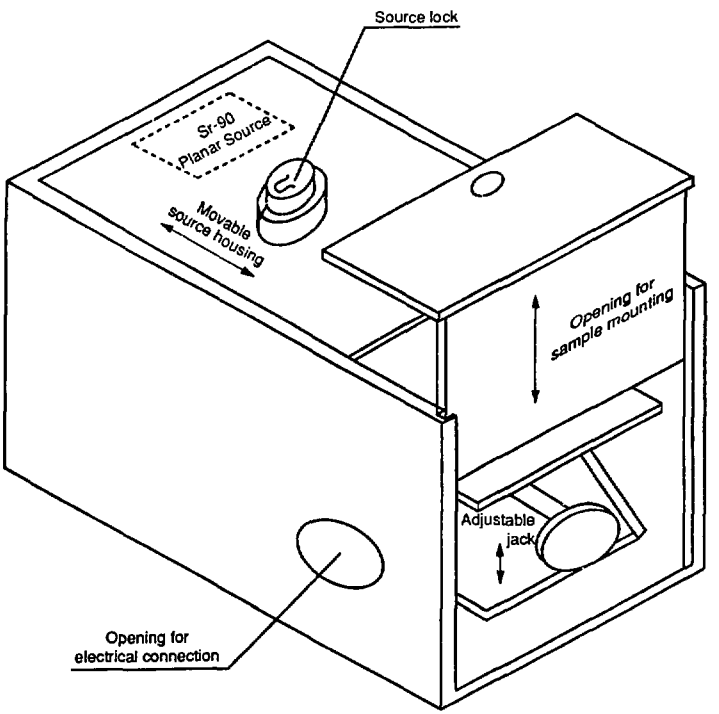


Fig. 1: Schematic description of the portable irradiation setup.

## *Reference*

[1] Y. Lifshitz, J. Levinson, Y. Noter, Y. Shamai, A. Akkerman, O. Even, A. Zentner, M. Israeli, A. Gibrekhterman and L. Singer, *IEEE Trans. Nucl. Sci.* 40: 1388 (1993).

## Radiation Tolerance of the OFFEQ LEO Satellites: Design-Policy, Ground Testing and Flight Data Evaluation[1]

D. Ilberg, Y. Lifshitz, Y. Noter, J. Barak, A. Akkerman,
D. Brand, A. Zentner, D. David and J. Levinson

The susceptibility of the OFFEQ LEO satellites to different radiation effects during passage through the SAA (South Atlantic anomaly) was studied. Design, ground testing and actual flight performance and anomalies were studied. TID (total integrated dose), SEL (single event latchup) (protons and heavy ions) and SEU (single event upset) effects were considered.

The radiation design policy of the first two OFFEQ satellites was defined. In-flight data indicated that the SEU predictions were reasonable but the initial SEL evaluation was too conservative.

Proton fluxes within the Van-Allen belts were found to be the major source of SEU for these LEO satellites. A single measured case of SEU located outside the radiation belts indicates that the probability of heavy ion-induced SEU from galactic particles may be much higher than usually predicted for low altitudes and low inclination angles.

The post-flight detailed SEL cross-section measurements performed by a combination of a heavy ion accelerator and a proton accelerator yielded lower proton induced cross sections than initially assumed, in accord with the actual flight data.

*Reference*

[1] D. Ilberg, Y. Lifshitz, Y. Noter, J. Barak, A. Akkerman, D. Brand, A. Zentner, D. David and J. Levinson, *2nd ESA Electronic Components Conf.* (Noordwijk, the Netherlands, May 1993).

## Study of the Long-Term Stability of Peaks 4 and 5 in TLD-100 Using Computerized Glow Curve Deconvolution (CGCD) and Thermal Peak Isolation Techniques: Correlation with Isothermal Decay Measurements at Elevated Temperatures[1]

Y.S. Horowitz*, B. Ben-Shachar and D. Yossian*

The long-term fading of peak 5 has been studied using four different annealing regimes, in order to isolate the behavior of peak 5 free from interference effects of peaks 2, 3 and 4. Peaks 4 and 5 (separated *via* CGCD) appear to have an exquisitely complex, time-dependent response to ionizing radiation, possibly due to clustering of dipole trapping centers associated

*Ben-Gurion University of the Negev, Beer-Sheva.

with peaks 2 and 3. Peak 4 grows over the first 9 months of storage and only then begins to decay; peak 5, on the other hand, decays rapidly in the first 6 months and then stabilizes or even begins to grow. Peaks (4+5) together, however, fade in a monotonically decreasing manner at a rate of approximately 8% per annum. Using thermal cleaning procedures to isolate the behavior of peak 5, we have determined that the 20°C meanlife of peak 5 is 5.5 ±1 years (1 SD). The meanlife is two orders of magnitude smaller than predicted by the exponential extrapolation of the meanlives measured at higher temperatures by the 'residual' isothermal decay technique and five orders of magnitude smaller than predicted by the exponential extrapolation of meanlives measured *via* peak shape techniques. The discrepancy suggests that the long-term decay of peak 5 is influenced by the precipitation of $Mg^{2+}$ or other forms of decay not associated with charge carrier detrapping and not explainable quantitatively, or in a rigorous manner, with current models.

The short-term fading behavior of peak 5 alone, on the other hand, does appear to be 'well-behaved', at a rate of 3.4 ± 0.8% (1 SD) per month (for the first month) irrespective of annealing routine, or the presence of peaks 2 and 3. This suggests the possibility of universal short-term fading corrections in environmental and personnel dosimetry if only peak 5 is used in dosimetric measurements.

*Reference*

[1] Y.S. Horowitz, B. Ben-Shachar and D. Yossian, *J. Phys., D Appl. Phys.* 26: 1475 (1993).

## RAM I-125[1]

N. Ankry, E. Vulaski, A. Matmor and N. Tal

The use of $^{125}I$ is very common in biological and medical laboratories. In order to detect and measure $^{125}I$ radioactive contamination, a dedicated and unique instrument was developed. The RAM I-125, a microprocessor-based instrument, is provided with friendly software that allows detection of low level contamination by $^{125}I$, while other isotopes do not influence the measurements. The I-125 meter activates an alarm when the threshold value is exceeded. The alarm threshold can be changed by the user, and the last threshold value is saved even after the instrument is turned off. The detection unit is based on a 1" x 1 mm NaI(Tl) scintillator coupled to a photo-multiplier. A Built In Test (BIT) continuously checks both counter and detector, and warns the user of detector failure, exceeding threshold value, reading overflow, or low battery. The Ram I-125 has a fast response time and stable reading.

*Reference*

[1] RAM I-125 Contamination Meter, Operating Manual. 1st ed. (Dec. 1993), Rotem Industries Ltd., Beer-Sheva.

## RAM ION Pressure Response Instrument[1]

N. Ankry, D. Elgad, D. Aharoni, E. Vulaski and N. Tal

RAM ION[1] is a portable ion chamber survey meter, designed for highly stable and accurate measurement of dose rates and integrated doses of gamma, X-ray, and beta radiation. The original RAM ION meter was very sensitive to pressure changes. Two reasons were found to be the cause of this problem. The first is the ion chamber entrance window cover, being made of a very thin and flexible synthetic fabric. Pressure variations caused changes in the tenseness of this thin material, which in turn led to changes in the chamber volume. Consequently these changes were interpreted as radiation field changes, and thus the meter displayed erroneous readings. This problem was solved by adding a wheel-shaped plastic construction on the ion chamber entrance window cover, thus contributing to the chamber strength and to the readings' stability. Another problem was the very short distance between the ion chamber's internal electrode and the chamber cover. Consequently, slight pressure changes brought about instability in the measurement readings. This problem was solved by shortening the electrode length. Eliminating RAM ION's pressure problems improved dramatically the stability of readings.

*Reference*

[1] RAM ION Meter for Wide Range Gamma, X-Ray, and Beta Radiation Measurement, Operating Manual, 2nd ed. (Nov. 1993), Rotem Industries Ltd., Beer-Sheva.

## RAM ION Communication with WRM

N. Ankry, T. Mazor and N. Tal

The Wireless Remote Monitoring (WRM)[1] system is used to collect data from remote dosimeters through a radio transmitter. A spread spectrum radio receiver intercepts status frames from one or more dosimeters, passing them to a laptop computer. A special adapter was developed to connect the RAM ION[2] to the radio transmitter. RAM ION is a portable ion chamber survey meter, designed for highly stable and accurate measurement of dose rates and integrated doses of gamma, X-ray and beta radiations. A dedicated software package was developed and incorporated into the RAM ION software to enable its communication with the WRM system. The latter is able to identify the instrument type and distinguish between the RAM ION meter and remote dosimeters.

*References*

[1] WRM 91 User Manual, Merlin Gerin Inc., Smyrna, GA, USA (1991).

[2] RAM ION Meter for Wide Range Gamma, X-Ray, and Beta Radiation Measurement. Operating Manual, 2nd ed. (Nov. 1993), Rotem Industries Ltd., Beer-Sheva.

## The RAM-R System

T. Mazor, U. Wengrowicz, D. Tirosh, E. Vulaski,
E. Duvniz and M. Ellenbogen

A new version of the RAM-R system was developed to meet the requirements for ruggedized radiation measuring equipment. RAM-R is a portable, simple-to-use device for detection and measurement of radioactive radiation. The basic unit is a microprocessor-based monitor containing an internal detector with two energy-compensated Geiger Muller (GM) tubes (ZP1201 and ZP1301), for wide range gamma field measurements (0.5 μSv/h to 5 Sv/h). Switching between the two GM tubes is controlled automatically by the microprocessor, according to field level. A dedicated communication protocol was developed and incorporated in the monitor to enable sending measured data and RAM-R status to a remote control center.

Three rugged external detectors are included with the RAM-R system: (i) GM-14, an end window GM probe for alpha, beta and gamma surface contamination detection, used also to detect contamination in food and liquids; (ii) GM-34, an energy-compensated GM probe for low level gamma field detection for stationary applications; and (iii) PM-14, a scintillation probe for detection of gamma radiation from a helicopter, which can be used also as a very sensitive food detector. The monitor and its detectors are sturdy and can stand vibrations, shocks and extreme temperature ranges.

A simulator for training personnel, which is part of the system, is a RAM-R-like instrument that includes a radio receiver instead of the internal detector. The simulator receives a code sent by a remote transmitter, and translates it into a specific radiation level, according to a look-up table.

The monitor and its detectors are placed inside an aluminum suitcase for transport.

## Simulator for the A-SMG 90

T. Mazor, U. Wengrowicz, N. Ankry and E. Maiss

The A-SMG 90 is a portable, simple-to-use instrument for detection and measurement of radioactive radiation, developed to meet the Austrian Army requirements as published in the Austrian tender for radiation measuring equipment. An A-SMG 90 simulator was developed, as required, to be used in training instead of the A-SMG 90 instrument itself, in order to avoid user exposure to radioactive sources.

The simulator, an A-SMG 90-like instrument, includes a radio receiver instead of an internal detector. Its RF receiver was developed at Elin, Austria. The simulator receives a code, sent by a remote transmitter, and translates it to a specific radiation level according to a look-up table. The transmitter sends the data by modulating the HF carrier in Pulse-Paused-Code (PPC). Logic levels are defined as follows: logic "1" - 16 cycles of high frequency during 11.7 msec, followed by one cycle of low frequency during 11.7 msec; logic "0" – one cycle of low frequency during 11.7 msec. Data are organized in frames that consist of one start bit and eight information bits each. The start bit is similar to logic "0", which appears after high frequency. The remaining bits include: first bit for alarm ("0" – OK, "1" – alarm), second bit for measuring range ("0" – low range, "1" – high range), six bits that include the measurement code, the decoding of which is based on a look-up table.

Since the transmitter has not been available to us (it was forbidden to remove it from Austrian territory), a dedicated tester was developed to enable testing the A-SMG 90 simulator. Its purpose was to generate artificial data emulating the real transmitted data. The tester includes pulse generators controlled by a microprocessor to generate the required data frames. The tester has been very useful during the integration between the A-SMG 90 simulator and the RF receiver in Austria. The tester output was fed into the RF transmitter and modulated the HF output signal. This RF signal was received, decoded and displayed by the simulator.

## RADTEST

M. Ellenbogen, E. Duvniz, E. Maiss, E. Vulaski and T. Mazor

RADTEST is a portable, light-weight instrument designed to monitor the radioactivity level in samples taken from food or liquids. It consists of a radiation meter, food container, telescopic rod, carrying bag, and battery charger. The detection system is based on a CsI (Tl)

scintillator coupled to a photodiode. The RADTEST identifies four different energy windows: iodine, 271 – 477 keV; cesium, 523 – 880 keV; cobalt, 1030 – 1500 keV; and total, 150 – 1500 keV. It determines the specific contamination, the ambient dose equivalent rate, and the commutative dose of gamma radiation in the sample. A unique algorithm calculates the radioactive contamination per kg according to the food type. Results are displayed in Bq/kg.

The first prototype of RADTEST was developed by French companies. Our team continued the development and design, prepared the production file, and constructed a new prototype. More features were added, such as a telescopic rod with the same detector mounted on the top of the rod, display illumination, and beeper for audible alarms. The electronic hardware was redeveloped using Surface Mounted Devices (SMD). The new design, packaging, and use of SMD devices reduced the instrument weight by approximately 60%.

## BAKNET - Communication Network for Radiation Monitoring Devices

O. Burstein, U. Wengrowicz and D. Tirosh

A communication network for real-time data collection from radiation monitors was developed. The network allows accurate and rapid data collection, requiring minimal personnel. The BAKNET network is a loop-shaped communication network (Fig. 1) that contains the following: RS 485 communication protocol enabling data collection from distant monitors at a baud rate of 9600; a main computer (PC) with an RS 485 board serving as master in the network; and a communication adapter for each radiation monitor serving as slave in the network.

To address output signals of the various radiation monitors, a different type of communication adapter is used for each type of radiation monitor. Two types of adapters were developed: one for radiation monitors with a serial RS 232 output, and the other for radiation monitors with analog data, and digital alarms and threshold outputs. The two types differ in software and in the use of an A/D converter for analog output devices. The adapter's main tasks are to communicate with the radiation monitor using the radiation monitor protocol, and to pass the received information to the main computer, according to a fixed protocol. The adapter's hardware includes: an 8032 processor, RS-232 communication IC to communicate with the radiation monitor, RS 485 communication IC to communicate with the main computer, digit-switches to determine the adapter address and the type of attached radiation monitor. The adapter's software includes the following modules: communication with the radiation monitor for sending a request and receiving data, communication with the PC waiting for a request from the PC and sending back the pre-processed data, information processing of data and alarms, main module, and initialization and digit-switches reading module.

Another possible use for the adapter is for data collection from industrial devices or from any devices located outside of the control room.

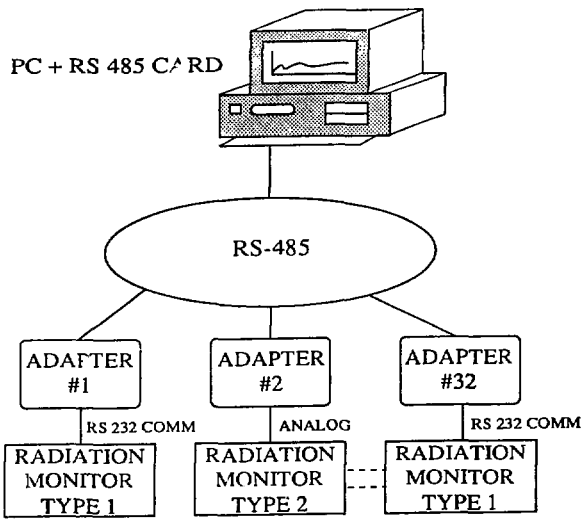


Fig. 1: Overview diagram of the communication network.

## The Israeli Radioactive Monitoring Network[1]

T. Mazor, A. Shuster, Y. Shemesh, Y. Harush and H. Assido

A radioactive area monitoring system[1] has been developed and established for the Israel Ministry of the Environment[2]. The system is aimed to measure the air gamma radiation level and activate an alarm in case of a significant change in the background radiation level. The system includes a Control Center located at the Environmental Research Institute in Tel Aviv, and monitoring stations situated in Haifa, Jerusalem, Tel Aviv, Beer-Sheva and Dimona (see Fig. 1). The control center collects data from the monitoring stations *via* a telephone line. This accumulated data base enables management of alarms and failures diaries, and a measurements archive. The stored data in the archive are used for data processing, graphical display of dose rate values *vs* time, and reports printout. In case of an alarm condition, the monitoring station activates an alarm message that is transmitted *via* a radio frequency

network to a beeper display held by the system manager. The radio alarm is transmitted in parallel to the alarms transmitted by telephone. In case of a telephone communication failure, the radio communication is used as a backup for alarm transmission.

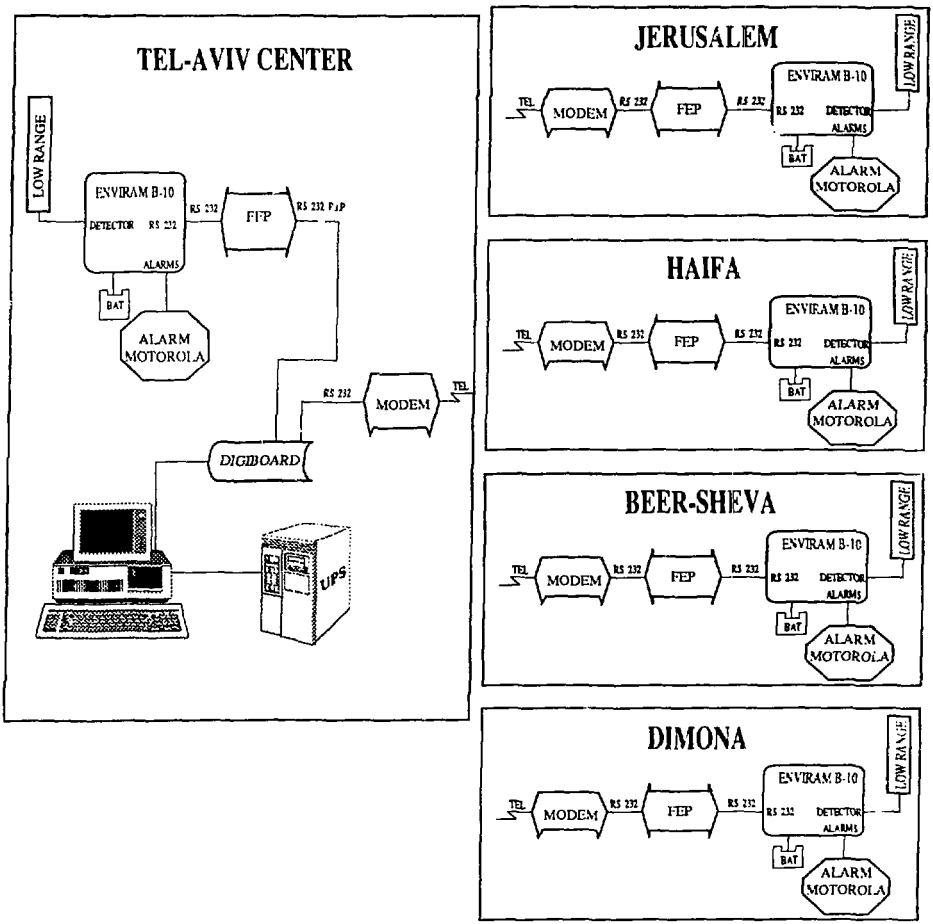


Fig. 1: Radioactive monitoring system network.

*References*


[1] T. Mazor, *IA-1481* (1993), p. 216.

[2] T. Mazor, Proposal, Environmental Radiation Monitoring System (Nov. 19, 1991), Rotem Industries Inc., Beer-Sheva.

# Housing for On-Line Liquids Radioactive Contamination Detection Unit

M. Ellenbogen, E. Duvniz, Y. Shemesh and H. Assido

A housing for on-line radioactive contaminations in liquids was developed, designed, built, installed and tested for a detection unit (see Fig. 1). The detection unit includes the following: a constant flow of liquid sample from the tested reservoir into a container designed as a double wall basin in order to keep the liquid sample at constant volume and with no ripples; an inlet pipe located close to the bottom of the inner basin, the overflow liquid flowing to the outer basin and circulating back to the reservoir through the outlet pipe; and a gas flow proportional detector placed above the sampled liquid, with a special fixture designed to maintain a fixed gap of 6 mm between the liquid surface and the detector. The detector is heated to a temperature of approximately 30°C using a heating tape to prevent water vapor from condensing on the detector surface. A flow of heated air is pumped at low pressure into the gap between the liquid and the detector. The shielding system around the detector and the water sample includes three layers. The main layer consists of 50-mm lead bricks to decrease the influence of cosmic rays and background radiation. Two additional layers are a 1-mm copper inner layer to decrease X-ray radiation from the lead, and a 2-mm aluminum outer layer to prevent operators' contact with the lead. A narrow slice in the shielding, precisely against the gap, allows the operator to insert a calibration source for accurate and rapid calibration.

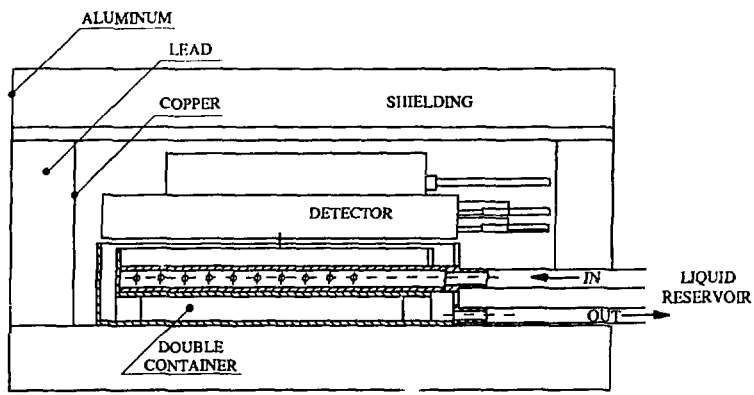


Fig. 1: The shielding system.

The whole detection system is installed in a rack. This unit provides the possibility to measure contamination in liquid reservoirs by using a large area proportional gas-flow detector. The cosmic and background radiation interference is minimal.

*Reference*

[1] H. Assido, S. Piestun, Y. Shemesh, A. Algom and Y. Ronen, *IA-1427* (1987), p. 210.

## Alpha and Beta Radioactivity Contamination Counting System

U. Wengrowicz, D. Tirosh, S. Piestun, Y. Shemesh and H. Assido

A microcontroller-based electronic system for an Alpha and Beta Radioactivity Contamination Counting System (ABRCCS) has been developed and designed to detect and measure radioactive contamination in 'smear samples'. Functional operation and maintenance simplicity were taken into consideration in designing the system. The ABRCCS consists of a pair of proportional detectors: a *smear sample* detector and a *cosmic-ray* detector, a detector's adapter and a microcontroller-based electronic unit that controls, measures, processes and displays the detectors' output signal.

The counting system principle of operation is based on sequential changing of the high voltage supplied to the detectors, while counting first in the alpha mode and then in the alpha + beta mode. Alpha radiation intensity is obtained directly from the counts in the alpha mode, while beta intensity is calculated by subtracting the contribution of alpha counts from the counting result in alpha + beta mode. An anti-coincidence circuitry minimizes the effect of cosmic and background radiation. The system's operation is based on a set of functions selected by two-digit switches in the CPU module front panel, which define the desired operation mode. The controls, display, warning thresholds, and malfunction tests are performed automatically by the ABRCCS microcontroller. Using a maintenance key switch located on the counting system's rear panel, enables calibration of the operating voltage and setting of warning thresholds. As the key switch is turned off, only routine operating modes can be performed without the risk of performing an erroneous setting. Fast and safe system operation modifications and data communication to other systems' softwares are easy to obtain due to the software modular construction. A serial RS232 communication channel with a PC-type computer, enables hard or floppy disk data storage and further data evaluation by a software engineer. The modular Eurocard Standard of the measuring unit eases system failures' detection and maintenance. Each Eurocard Module can be replaced by a similar one without further calibration.

This counting system, which is a new version of a system developed a few years ago[1], is presently working satisfactorily.

*Reference*

[1] S. Levinson, Y. Mazor, A. Matmor and U. Wengrowicz, *IA-1427* (1986), p. 204.

## Training Detector as Simulator of Alpha Detector

J. Paran, D. Tirosh, M. Shmuely, Y. Ronen and H. Assido

Alpha radiation contamination is commonly detected with a proportional cell detector with a large-area thin-mylar entrance window. Since the free path of alpha in air is no more than a few centimeters, the detection is performed by placing the detector very close to the contaminated area. Alpha sources are very rare, with a long half-life, and dangerous to handle from a health physics point of view. For these reasons, there arose the need to develop a special detector for training health physics personnel to use an alpha contamination probe by detecting different isotopes such as gamma sources. This detector should detect a short half-life gamma source like $^{99m}$Tc, which is commonly used, and should act as a proportional detector imitating the alpha-detecting properties.

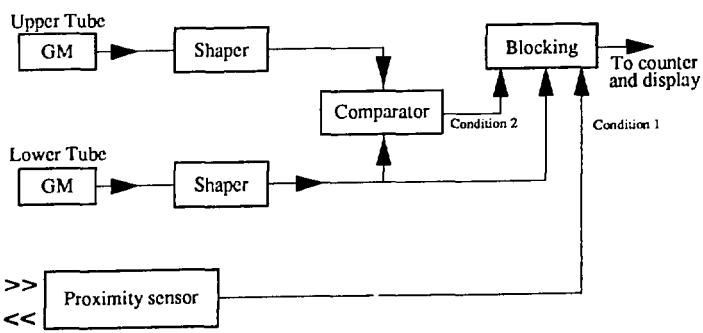


Fig. 1: Training detector block diagram

The developed training detector (Fig. 1) contains two GM tubes, a proximity sensor, two shapers, a comparator and a conditioned blocking circuit. Both GM tubes are located near the detector bottom, one 2 cm above the other. The proximity sensor is located on the bottom as well. The blocking circuit transfers the lower GM pulses to the counter, only if both conditions are '0' logic. Condition 1 means that the detector is less than 10 cm from the tested area, and condition 2 represents a significant difference of the pulse rates between the two GM

tubes. Since the lower GM tube is located closer to the tested area, it produces a higher pulse rate than the upper tube.

The detecting performance of the training detector in a $^{99m}$Tc-contaminated area should be very similar to that of an alpha proportional counter in an alpha-contaminated area. The training detector will stop sending pulses when elevated more than 10 cm above the contaminated area, due to the proximity sensor. However, it will stop sending pulses also if it is located within the 10 cm above the contaminated area but deviated aside from the contamination spot. In this case the geometry of the GM tubes will cause them to produce the same rate, which violates the second condition. This means that the detector will send pulses to the counter only when it is located within 10 cm above the area and right above the contamination spot. A preliminary prototype of the training detector was built and tested successfully, thus encouraging its development into a useful product.

## Detection Limits of Different Measuring Methods for Natural Uranium

O. Pelled, U. German, M. Weinstein, S. Levinson, O. Shimon, R. Kol and E. Naim

The minimum detectable activity (MDA) of natural uranium on filter samples and the activity ranges for different measuring methods were evaluated. The methods were: gamma spectrometry with NaI(Tl) and GeLi detectors, liquid scintillation method, ICP method, laser excitation method, $\alpha$-surface detector (air proportional detector) and $\beta$-surface detector (GM). The $\gamma$ spectrometry method and the $\alpha$ and $\beta$ counting methods measure the radiation emitted from the uranium samples and no chemical preparation is needed. The detector has to be calibrated to the sample geometry. The liquid scintillation, ICP, and laser excitation methods require a solution and the uranium in the sample has to be dissolved first in $HNO_3$. Uranium samples of known activity were measured and counted on the different systems to evaluate the MDA and the activity range of each system. For the direct counting methods, filters with diameters up to 47 mm were used. For the methods in which the uranium is dissolved in $HNO_3$, a volume of 50 cc was used.

The activity ranges for the different measuring systems, based on the limitations mentioned above, are given in Table 1.

Table 1
Ranges of the different systems

| System | MDA (μg/sample) | Upper range (μg/sample)* |
|---|---|---|
| α surface detector | 8 | >100,000 |
| β surface detector | 44 | >100,000 |
| NaI(Tl) | 900 | >100,000 |
| GeLi | 330 | >100,000 |
| Liquid scintillation | 20 | 100,000 |
| ICP | 12.5 | >100,000 |
| Laser excitation | 0.05 | 1 |

*The systems' linearity was checked only up to 100,000 μg/sample.

## A Computerized Data-Base System for Personal Internal Contamination Results

S. Levinson, U. German, Y. Laichter and E. Naim

A data-base system which contains internal contamination results from a whole body counting (WBC) system and a radiotoxicology laboratory, was prepared.

The spectra obtained from a Nucleus-PCA card (Series 2 Personal Computer Analyzer, Nucleus Inc., Oak Ridge, TN, USA) and two 5" Phoswich detectors of the WBC system[1,2] are analyzed, after the accumulation process, by a Quick Base 4.5 software. The various regions of interest of the spectra are compared with the minimum detectable activity (MDA) values. The calculated activities, including remarks for values over investigation levels (IL) and recording levels (RL) according to the ICRP 30, are printed out. The values obtained from the various radiotoxicology measurements are typed in and checked *vs* MDA, IL and RL levels by a Quick Basic 4.5 software.

The two programs save the data as similar records containing also personal details and the counting information (such as counting time, date, activity or MDA level). At present, the data are used as input to a Quick Basic 4.5 program which merges the files, sorts and prints reports. The reports, including the IL, RL, or MDA values, are used for further investigations.

*References*

[1] S. Levinson and Y. Laichter, *IA-1440* (1988), p. 276.

[2] U. German, S. Levinson, R. Kol, E. Naim, S. Piestun, H. Assido and Y. Ronen, *Trans. Nucl. Soc. Isr.* 16: 207 (1990).

# A Quick Quantitative Evaluation of a Specific Radio Nuclide from 'Nucleus PCA' Spectra

S. Levinson, U. German, O. Pelled, M. Weinstein and E. Naim

Pulse spectrum analysis using PCA cards (*e.g. Nucleus PCA* Series 2, Personal Computer Analyzer, Nucleus Inc., Oak Ridge, TN, USA) implemented in a computer system, has become very popular. The PCA software enables spectra analysis using specific programmed functions included in the PCA package. In some routine applications involving quantitative analysis of a large number of samples containing the same radio nuclide, it was found that the process can be made more efficient and simple by using software with direct access to the data of the accumulated spectra.

A program was developed using Quick Basic 4.5 language for samples containing natural uranium. The first stage of the program is the access to the data in the binary spectrum file stored previously by a PC automatic task. The channel counts of the 185 keV peak region then are displayed on the CRT and the operator is required to confirm or to set the appropriate

File Name: Vasl.spm
Elt: 9000 sec
Spec.Start Acquire Date: Jun 24, 1993
Time: 09:48:13 am
ID: Vaseline 1/2 liter

| Ch | Counts | |
|---|---|---|
| 181 | 29 | XXXXXXXXXXXXXXXXXXXXXXX |
| 182 | 36 | XXXXXXXXXXXXXXXXXXXXXXXXXXX |
| 183 | 26 | PPPPPPPPPPPPPPPPPPPP |
| 184 | 35 | PPPPPPPPPPPPPPPPPPPPPPPPPPP |
| 185 | 42 | PPPPPPPPPPPPPPPPPPPPPPPPPPPPPPPPP |
| 186 | 52 | PPPPPPPPPPPPPPPPPPPPPPPPPPPPPPPPPPPPPPPPP |
| 187 | 63 | PPPPPPPPPPPPPPPPPPPPPPPPPPPPPPPPPPPPPPPPPPPPPPPPP |
| 188 | 31 | PPPPPPPPPPPPPPPPPPPPPPPPPPP |
| 189 | 40 | XXXXXXXXXXXXXXXXXXXXXXXXXXXXXXXX |
| 190 | 25 | XXXXXXXXXXXXXXXXXX |
| 191 | 36 | XXXXXXXXXXXXXXXXXXXXXXXXXXXX |
| 192 | 26 | XXXXXXXXXXXXXXXXXXX |
| 193 | 19 | XXXXXXXXXXXXXXX |

Result: Vaseline 1/2 liter sample activity (.0616 mgU) MDA 3sig (.1005 mgU)

Fig. 1: An example of the results' printout.

185 keV peak boundaries. The counting efficiency factors for different geometries are defined in the program and used in the calculations. The appropriate background is subtracted, and the computed activity is compared with the Minimum Detectable Activity.

The computed result, as well as the original pulse height spectrum of the 185 keV peak area, are printed out. An example of the output is given in Figure 1. The program can be easily applied to other radio nuclides.

## A Square 7.5" Proportional Guard Detector

S. Levinson, H. Assido, Y. Shemesh, S. Piestun and U. German

A new version of a square 7.5" proportional guard detector was developed. The main difference between the 'Old' version, used in a microprocessor-based counting system[1], and the 'New' one, is in the anode wiring, which leads to better performance and easier manufacturing and assembly. Both detector versions are built of PVC coated on the inside with an electricity-conducting spray. The anode consists of nine stainless steel spiral wires of 0.002" diameter. Such spiral wires increase the anode length, are resistant to changes in temperature, and are also flexible and easy to mount. The counting gas in both detectors is 90% argon + 10% methane.

The 'Old' detector structure is shown in Figure 1a. The 0.002" stainless steel wires were soldered to two copper poles which are isolated from the PVC housing. The soldering procedure was difficult because of heat transfer problems and possible electrical noise produced by poor solder. In the 'New' version, shown in Figure 1b, the copper poles are replaced by Teflon spacers mounted on an outer slot of the PVC housing. The spacers have a 1 mm hole through which the anode wire is threaded in one strip for the whole detector. Only two solders are done, one inside the detector on the HV connector and the other on the wire's edge. The detector is sealed with RTV silicon adhesive.

In addition to the benefits of easier production and assembly, changing the anode assembly technique improved the detector's response. As shown in Figure 2, the beta plateau of the 'New' version is larger, and as shown in Figure 3 the background is lower for high voltages over 1850 V DC.

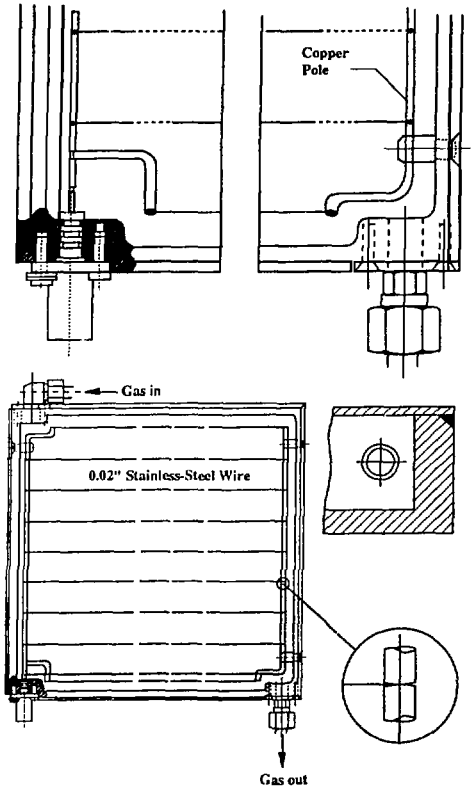


Fig. 1a: 'Old' guard detector version.

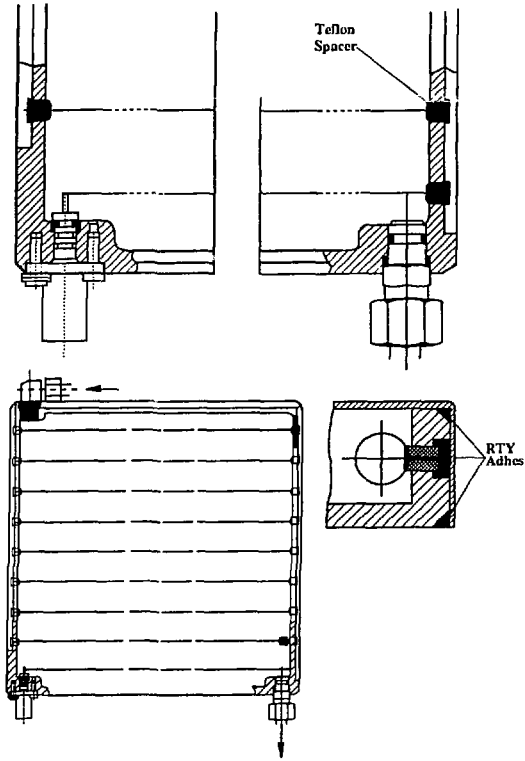


Fig. 1b: 'New' guard detector version.

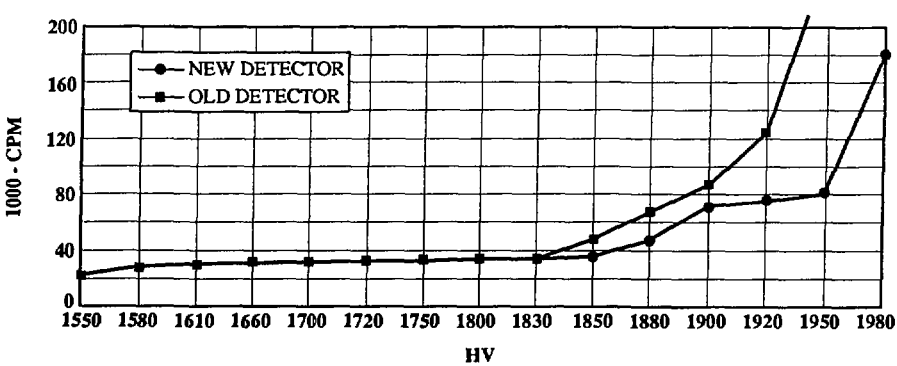


Fig. 2: Beta high voltage plateau.

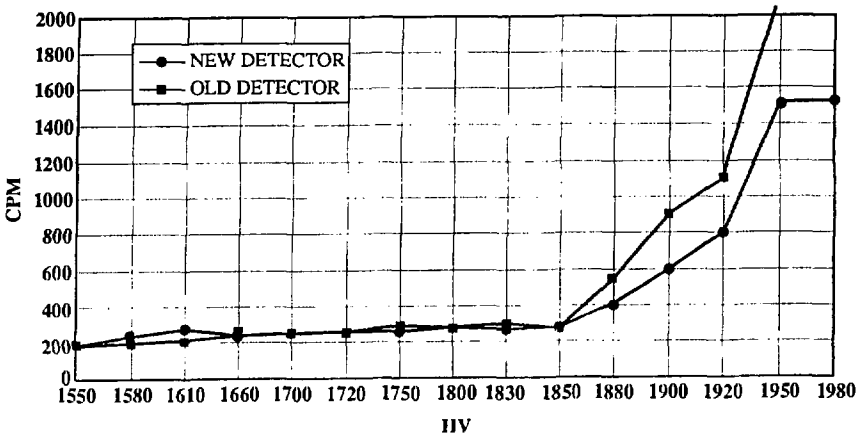


Fig. 3: Background *vs* high voltage (unshielded detectors).

*Reference*

[1] S. Levinson, U. German, I. Mazor, A. Matmor and U. Wengrowicz, *IA-1427* (1987), p. 204.

## A Manual Sample Changer for a 5" Proportional Detector Counting System

S. Levinson, Y. Elbaz, U. German and E. Naim

A manual sample changer was designed for a 5" 2π proportional Argon Methane counter[1] including a Guard detector[2]. The sample changer, shown in Figure 1, was designed for very low background counting, and therefore most of the parts are made of low background copper. Samples are positioned on an aluminum planchette of 4.5" diameter and 1 mm height which is placed on a tray. The tray is inserted manually towards the detectors and is stopped and fixed in place when the sample lies in front of the detectors. In order to increase the counting efficiency, the planchette is lifted automatically towards the detector. A lead shield (5 or 10 cm thick) can be added to the system. The whole assembly can be easily taken apart for repair or decontamination.

The sample changer was designed on a CAD system which enables easy changes for other detector geometry or detector types, such as the 'Sandwich' proportional detector[3].

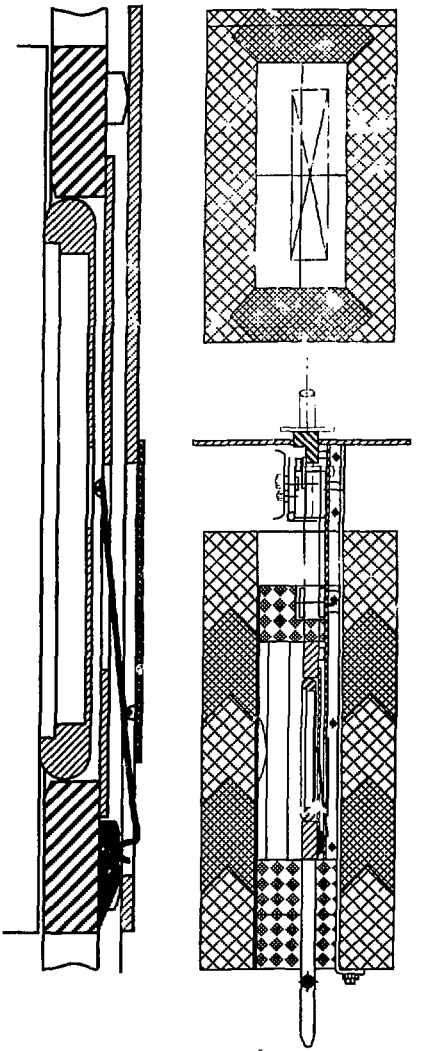

Fig. 1: The sample changer with 5 cm lead shielding.

## *References*


[1] S. Levinson, H. Assido, E. Reich and U. German, *IA-1427* (1987), p. 201.

[2] S. Levinson, H. Assido, Y. Shemesh, S. Piestun and U. German, *IA-1486* (1994), p. 139.

[3] S. Levinson, H. Assido, U. German, Y. Shemesh, S. Piestun, Y. Ronen and E. Naim, *Trans. of the Joint Meeting of the Nuclear Societies of Israel* (Herzliya, Israel, Dec. 1990), p. 95.

# VIII

# INSTRUMENTATION AND TECHNIQUES

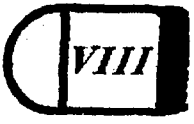

# Industrial X-Ray Computed Tomography

A. Baran, E. Polak, M. Tzabarim, C. Goresnic,
E. Iszak, M.S. Rapaport and A. Gayer

A second generation translate-rotate γ-ray transmission computerized tomography (CT) scanner was described earlier[1]. This scanner utilized a collimated $^{137}Cs$ radiation source (Eγ=662 keV) and BGO scintillators employed in pulse mode counting. The present work modified the scanner design to a double-decker one. The scanner's second level features an X-ray machine (kVp<160) and a detector array containing eight $CdWO_4$ scintillators employed in a mode of current measurement. The main efforts were the design and construction of the front-end electronics that enables measurements of currents between 3.0 pA and 3 nA, computerized data acquisition, and development and application of beam-hardening algorithms.

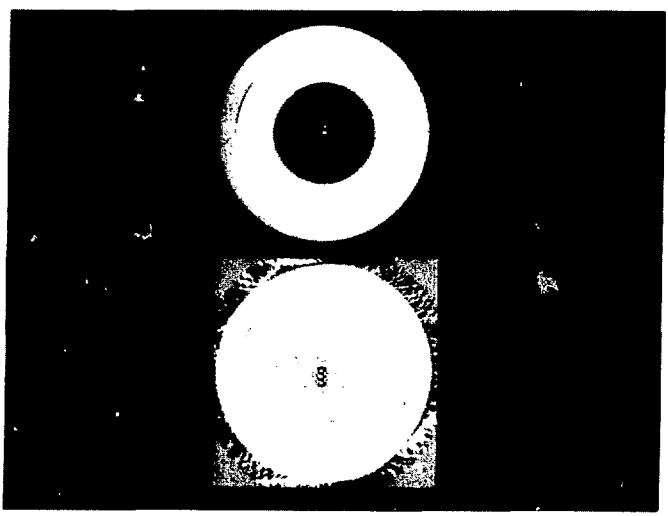

Fig. 1: CT image (original) of test body (top); and image after division by the original image that was computer rotated by 45° (bottom).

Figure 1 (top) presents a CT image of a test body composed of materials such that a 1:1000 radiation attenuation ratio is obtained at E=130 kVp. The test body contains four simulated separations gradually increasing in width from zero to 0.30, 0.46, 0.85 and 1.39 mm, between its two layers. The three larger separations are easily visualized. However, the reconstructed image contains the relevant information of the fourth separation (0.30 mm) as

shown in Figure 1 (bottom). This image is obtained by dividing, pixel by pixel, by the original image that was computer rotated by 45°.

*Reference*

[1] M.S. Rapaport and A. Gayer, *IA-1471* (1992), p. 175.

## Forensic Characteristics of Colored Polyethylene Bags[1]

Y. Nir-El

The inorganic elemental profiles of colored polyethylene bags were determined by X-ray fluorescence spectroscopy. Homogeneity in single bags and reproducibility of bags in a batch were ascertained. The probability of an incorrect matching of two very similar yellow bag batches was found to be $10^{-9}$ to $10^{-8}$, while a bag is attributed to its batch with a relatively high probability of the order of 1. These characteristics can be applied in the forensic examination of the colored polyethylene bags often used in drug abuse. Similar properties are reported for transparent polyethylene (no pigment additives), where the concentration of zinc was 0.6±0.1 ppm.

*Reference*

[1] Y. Nir-El, *J. Forensic Sci.* 39: 758 (1994).

## Determination of Lead in U.S. Dollar Paper Currency by X-Ray Fluorescence Spectroscopy[1]

Y. Nir-El

The aim of the present work was to study lead levels in the printing inks of U.S. dollar paper currency. Paper currency is an object of frequent daily use, and therefore contact with lead due to touching the notes is evident. Specimens were measured non-destructively by the X-ray fluorescence (XRF) method, which was employed due to its many advantages such as high selectivity and sensitivity, broad dynamic range, simultaneous analysis of most elements, and no requirement for preliminary treatment of samples.

It was found that U.S. dollar bills contained lead-based ink driers. Up to and including the printing year 1977, the areal concentration of lead was high compared with later printing years, and found to be of the order of 0.2 $\mu g/cm^2$. In 1981, and throughout the 1980s, the lead

concentration was decreased by a factor of 6. In bills printed in 1990, an additional highly significant decrease was detected, down to a value of approximately 0.8 ng/cm$^2$. This is an extremely low areal concentration, meeting the trend of reducing man's exposure to lead.

*Reference*

[1] Y. Nir-El, *Bull. Environ. Contam. Toxicol.* 52: (1994, in press).

## Nondestructive Testing of Objects Employing the Weighing Method[1]

Y. Nir-El and T. Karpinovitz

The aim of this work was to examine the feasibility of nondestructive testing (NDT) of industrial objects by the weighing method. The NDT technique is supposed to detect a partial or total absence of a critical component in the tested object. An alternative but more expensive method is radiography.

Typical objects are compressed gas containers which serve as gas generators, or pyrotechnic cartridges which contain propellants. In the weighing examination 12 objects were tested. The mean weight and sample standard deviation were 123.28 ± 0.38 g. The weight of the critical component was 1.57 g. We require that in the weighing test, off-spec objects are rejected at a 95% confidence level. Statistical analysis showed that the probability of false rejection of standard objects is greater than 90%, assuming that 10% off-spec critical components are rejected at the 95% confidence level.

It was concluded that the weighing method is not suitable within the framework of the prevailing requirements and that the radiography method is to be preferred. The major advantage of radiography is its capability to image critical components.

*Reference*

[1] Y. Nir-El and T. Karpinovitz, *Eichut* 9(5): 4 (1993) [in Hebrew].

## Base Pressure Calculation from Microwave Data Analysis in SPETC Launcher

R. Alimi, R. Hareuveni, D. Melnik, L. Perelmutter and S. Wald

Integration tests of an advanced Hypervelocity Weapon (HVW) for an Anti Tactical Ballistic Missile (ATBM) were performed recently. The three subunits that comprise the

HVW are a hypervelocity launcher, a miniature interceptor and a fire control system. The launcher, developed at Soreq, was able to fire a 4.9 kg D2-type projectile at a muzzle velocity exceeding 2 km/s.

The experimental set-up includes a high frequency microwave radar operating at 10.525 GHz. The projectile reflects the incoming wave, and the phase shift between the original and the reflected waves is recorded as a function of time. Outside the barrel the Doppler shift is Fourier analyzed and yields the muzzle velocity. In this work an in-bore analysis of the microwave data is performed to extract the time profile of the position, velocity and acceleration of the projectile before launching takes place.

After high-pass filtering the signal is treated by a Hilbert transform to produce a smooth, normalized cosine suitable for a precise interferometry analysis that results in a position *vs* time curve having the same resolution as the original data (namely, 5 μs). The travel curve is expanded over a combined polynomial-exponential basis set for least square fitting. Velocity and acceleration are obtained by analytical derivation. The pressure at the base of the projectile is calculated and compared with a Lagrange approximation estimated from the experimental breech pressure.

The main results were as follows: (i) The maximum value obtained for the acceleration lies around 50 kGee. (ii) There is overall good agreement between the values of the base pressure derived from the acceleration and those obtained from the Lagrange approximation applied to the measured breech pressure. (iii) The Lagrange approximation proved to be the most successful in the last stage of the ballistic process. (iv) Most of the deviations from the Lagrange approximation occur during the rise of the base pressure, when it underestimates the actual base pressure by approximately 20%.

## A Proof of the Need for Self-Consistent Treatment in Capillary Ablative Discharge Modeling[1]

D. Zoler* and R. Alimi

Numerical calculations show that a self-consistent model of a capillary discharge leads to much better agreement between the predicted values for plasma pressure and conductance and the experimental data than the results presented in Ref. [2]. Calculated values of other parameters that characterize the ablative plasma flow, are also provided. Qualitative agreement with experimental measurement is excellent and a good quantitative agreement is also shown. The remaining discrepancies may be due to technical problems in the setup of the experiment and not to inherent faults of the model. The following conclusions can be drawn:

*Tel-Aviv University, Tel Aviv.

(i) In [2], the predicted maximum pressure was less than half of the experimentally measured one. Our calculations predict correctly, within a few percentage points, the maximum value of the pressure. (ii) There is a time delay of approximately 140 μs between the measured and the calculated plasma pressure maxima, probably due to a problem in the pressure gauges calibration as mentioned by Powell and Zielinski[2]. (iii) The plasma conductance we calculated is in excellent qualitative agreement with that predicted in [2]. Our results confirm the slight dependence of the conductance on the pressure. Moreover, our calculations better fit the experiments than the results given in [2].

*References*

[1] D. Zoler and R. Alimi, Submitted to *J. Phys., D.*

[2] D.J. Powell and E.J. Zielinski, *IEEE Trans. Magn.* 29: 591 (1993).

## A Numerical Algorithm for Computing Solid Propellant Form Functions

R. Alimi and U. Onn

A general algorithm for computing the form function of an arbitrary shape of solid propellant was developed. The grain cross-section is mapped on a 2-dimensional matrix. A matrix element is either 1 or 0, if material is present or absent, respectively, at this place. As linear burning occurs, the matrix is updated and the sum over the non-zero elements gives the cross-section area. Slivering – the contact between burning surfaces in multiperforated grains – is automatically taken into account. Simple relations are used from computing the surface grain area from the cross-section. The method was applied successfully to a cylindrical seven-perforated grain and to a hexagonal 19-perforated grain. In the latter case the approximation made for solving the problem analytically has been removed, and an exact form function of this type of propellant is presented and used in a ballistic simulation.

## A Numerical Study of the Plasma Parameters Evolution in an Ablative Capillary Discharge for a Two Pulse Form of the Input Energy

D. Zoler*, D. Saphier and R. Alimi

A study of the spatial and temporal dependence of the all plasma relevant parameters was conducted within the frame of a general quasi one-dimensional model for ablative capillary

*Tel-Aviv University, Tel Aviv.

discharges and for a specific time-dependence of the input energy. Particular attention was given to the effect of a so-called 'second boost of input energy' that leads to a substantial increase in some of the main plasma parameters such as: exit velocity (26%), flux of mass (177%) and flux of energy (exit power) (285%). Calculations and experimental results are in good agreement. Reliability of the model and of the numerical approach is supported by energy conservation condition fulfillment and the critical value of the exit Mach number.

## Development of a New Electrochemical Probe for Atmospheric Corrosion and Surface Reactivity Measurements of Metals

R. Ydgar, N. Mayo, D. Ozer, J. Hayon, A. Raveh and A. Bettelheim

A new atmospheric corrosion probe, based on a solid-state electrochemical cell and a Nafion membrane serving as a solid polymer electrolyte, is introduced. Corrosion potentials and rates for a number of metal specimens, after being exposed to various atmospheric conditions, were measured in a number of solid-state cell versions and compared with electrochemical measurements conducted in aqueous solutions. Reproducibility and efficiency of the solid-state cell in probing changes in chemical reactivity and local surface effects depend on the reference electrode structure and membrane conductivity. Uncompensated resistance can be reduced by increasing relative humidity and applied pressure on the electrode/membrane interface.

## Rotation and Shift Invariant Image Classifier Using a Neural Network

R. Sharon*, R. Zilcha*, H. Guterman* and S. Greenberg

Classification by a Neural Network (NN)-based classifier, of natural images that have been subject to geometric distortions, was done in this work. The proposed method provides a reliable real-time classification method for aerial images. Invariant classification of shifted and rotated real-scene images was shown to be feasible. The invariance is achieved by training a NN with a large number of appropriate distorted scene samples. In this work feed-forward NN has been used as a means for image matching and classification. The performance of the NN classifier is compared with the classical correlation-based techniques.

*Ben-Gurion University of the Negev, Beer-Sheva.

*Reference*

[1] S. Greenberg and H. Guterman, *World Congress on Neural Networks* (Portland, OR, USA, July 1993), Vol. 3, pp. 745-748.

## Classification of Images Using Unsupervised Neural Networks

Z. Vered*, B. Feldman*, H. Guterman* and S. Greenberg

Classification of aerial images using unsupervised neural networks (NNs) was achieved. Automatic classification systems are constructed of three major stages: Preprocessing, features extraction, and classification. In this work we applied supervised and unsupervised NNs for features extraction and classification. This project focuses on the ability of unsupervised NNs based on ART[1] and KOHONEN[2] architectures to classify and extract features from various images. Real images contain noise and geometrical distortions such as shift, rotation and scaling. Upon receiving the distorted images, the system should classify each image into a representative category, invariant to the noise and distortions. The optimal image features which are invariant to the possible distortions or to some of them are used as input to the NN. Some networks (such as the NEOCOGNITRON[3]) are invariant due to their inner architecture. We combine invariant transforms for feature extraction with NNs as an automatic unsupervised classifier.

*References*

[1] G.A. Carpenter and S. Grossberg, *Appl. Opt.* 26: 4919 (1987).

[2] T. Kohonen, *Proc. IEEE* 78: 1464 (1990).

[3] K. Fukushima, S. Miyake and T. Ito, *IEEE Trans. Syst., Man, Cybern.* 13: 826 (1983).

## Application of Neural Networks for Interpretation of Ion Mobility and X-Ray Fluorescence Spectra[1]

Z. Boger and Z. Karpas

Neural networks (NN) have been used successfully to interpret spectral data, and to derive qualitative and quantitative information, from ion mobility spectrometry (IMS) and X-ray fluorescence (XRF). It was shown that components of complex mixtures of up to six aliphatic amines may be automatically identified by NN methods from their mobility spectra, with

*Ben-Gurion University of the Negev, Beer-Sheva.

reasonable accuracy. The ability of NN to identify compounds even under low signal to noise conditions of IMS spectra was demonstrated. The use of the XRF technique for quantitative determination of part-per-million (ppm) amounts of mixtures of Re, Os, Ir and Pt in a polyethylene matrix, which could not be done successfully by conventional methods, was made possible by application of NN, with standard deviations of 3.3, 2.7, 2.4 and 5.8 ppm, respectively. The networks could be trained on a PC machine, in less than 10 minutes, from a surprisingly small data set of training samples (fewer than 10), to perform these tasks.

*Reference*

[1] Z. Boger and Z. Karpas, *Anal. Chim. Acta* (1994, in press).

## Texture Analysis for Target Recognition

B. Israeli*, R. Knol*, I. Rotman* and S. Greenberg

A model for identification and classification of targets in the presence of different background noises enables the detection of identical targets in the background of a variety of scenes. During the last several years an effort was made to find a suitable model among the following: markovian, fractal, cortex transform, or correlation that can be used in order to classify textures[1,2]. The model under development and construction is based on cortex transforms and correlation[3,4]. It includes orientation filters for feature extraction and identification of geometrically distorted targets such as rotation, shifting and up & down scaling. The proposed model is being checked and verified with artificial and natural images, using neural nets for optimal final classification.

*References*

[1] H. Wechsler, *Signal Process.* 2: 271 (1980).
[2] R.M. Haralick, *Proc. IEEE* 67: 786 (1979).
[3] V. Honkonen, T. Jaaskelainen and J. Parkinson, *Proc. SPIE* 1564: 43 (1991).
[4] C. Goresnic and S.R. Rotman, *Graph. Models Image Process.* 54: 329 (1992).

*Ben-Gurion University of the Negev, Beer-Sheva.

# Remote Data Collection Terminal

J. Goldberg, A. Gabovitch and S. Greenberg

An intelligent remote data collection terminal is presented as part of a versatile data collection system called ORLOGIN-2000[1]. The microcomputer-based terminal can be used as an autonomous device and as a remote terminal connected to a host computer. Up to 255 terminals can be linked to the host computer and to each other, *via* an RS-485 serial multidrop communication link. The data collection terminal can be programmed for multi-purpose applications such as: time and attendance, job costing, security access control, shop-floor management and real-time data collection. A dedicated software package was developed for each application.

The data collection terminal consists of a main 80C32-based CPU board, an optical bar-code slot reader, a wand reader as an option, an alphanumeric LCD, and a functional keyboard (Fig. 1). The remote terminal operates as a stand-alone unit, and therefore a communication link failure does not affect its operation.

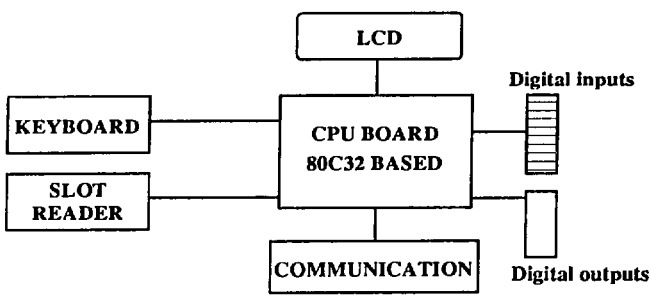


Fig. 1: Remote data terminal.

The terminal software package is responsible for collecting real-time data, validating the data, saving it in the local memory, and acknowledging the user. A special software package establishes the communication protocol with the host, receives downloaded data (tables and instructions) from the host, and sends the appropriate collected data to the computer for further processing. The data collection terminal is designed to be a user-friendly device with a unique man-machine interface.

*Reference*

[1] S. Greenberg, N. Tsouri and A. Gabovitch, *IA-1427* (1992), p. 185.

# Invariant Image Classification Using Composite Filters

S. Greenberg, B. Sarousi, N. Cohen* and Y. Dolev*

Invariant image classification is required in many image processing applications. Correlation is often used as an approach to measure the similarity between a pair of images in order to classify a given image. The classical cross-correlation technique's principal weakness is that its performance deteriorates rapidly when the input image contains geometric distortions. Although correlation methods are invariant to a relatively small shift between images[1], this is not the case when rotation or a combination of rotation and scale is involved. Noisy and distorted real images may mask the correlation peak as well. Different correlation techniques based on orthogonal functions and invariant transformations are being considered. Some transforms such as Zernike moment, Mellin transform and the discrete two-dimensional Gabor transform are considered as space invariant transforms. These methods are not invariant to all possible transformations, require extensive computational preprocessing, and are restricted to a certain type of images such as synthetic images[2].

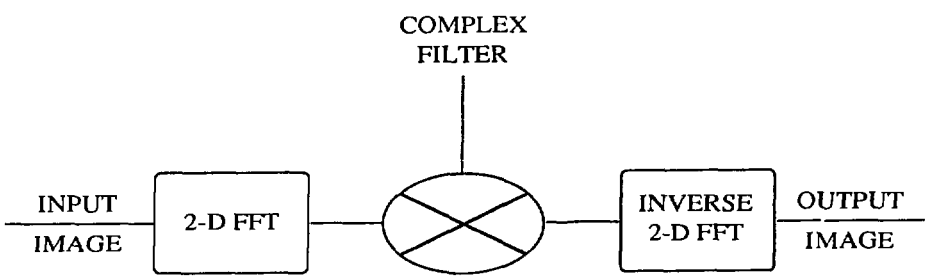


Fig. 1: Matched filter technique.

In the proposed method the invariance of real-world aerial images is achieved by designing a unique composite filter from a large number of appropriate distorted scene samples. Aerial images classification is carried out by using matched filter techniques (Fig. 1) based on Binary Phase Only Filter (BPOF) and Synthetic Discriminant Function (SDF)[3]. The composite filter is obtained essentially by a linear combination of training images, which the filter is programmed to detect. The filter is designed to recognize an object (or a given image) while rejecting all others. The SDF filter increases the performance of the matched filter and the phase filters (POF, BPOF). Using this technique, some degree of distortion

*Ben-Gurion University of the Negev, Beer-Sheva.

invariance is achieved. The invariance is obtained by choosing an appropriate set of geometrical and noisy distorted images. The classical correlation method performance is compared with the SDF complex filter.

*References*


[1] S. Greenberg and H. Guterman, *World Congress on Neural Networks* (Portland, OR, USA, July 1993), Vol. 3, pp. 745-748.

[2] C. Zetzsche and T. Caelli, *Comput. Vis., Graph. Image Process.* 45: 251 (1989).

[3] G.W. Carhart, B.F. Drayer, P.A. Buillings and M. Giles, *Proc. SPIE* 1564: 348 (1991).


## PC-Controlled Telemetry System


A. Cohen, A. Katz, D. Barak and A. Gabovitch


The Telemetry System includes remote-controlled devices that monitor input analog signals in a wide range and communicate *via* twisted pair cables using full duplex RS232 asynchronous communication. The Central Control and Display System (CCDS) developed by us (see Fig. 1) is based on a 486DX 33 MHz IBM PC Compatible Computer. A multi-port RS232 communication board is used to communicate with the remote devices and an analog output board is used to record signals on a strip chart paper recorder. The CCDS continuously monitors and displays input signals on a screen emulated strip chart, and plots them on a local paper recorder.

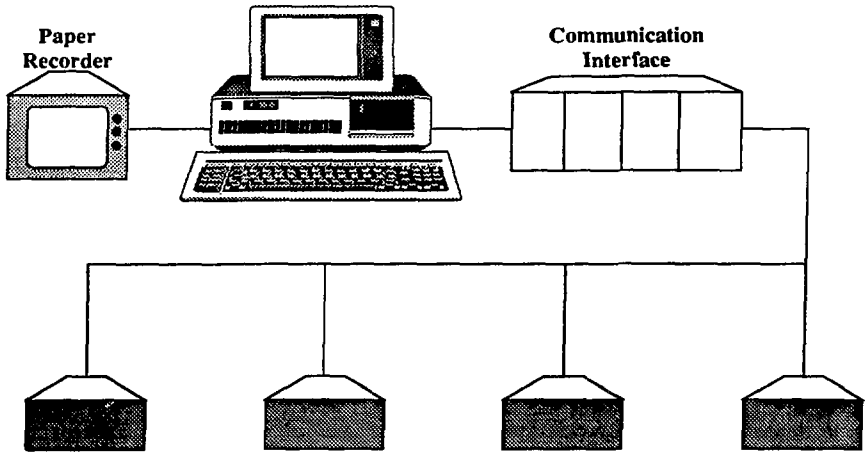


Fig. 1: PC-controlled telemetry system.

fitted to a modified diffusion model, suggesting a bulk diffusion mechanism coupled with a surface reaction. A practical implementation of this stripe structure for infrared light waveguide is being evaluated.

*Reference*

[1] M. Azoulay, M. Sinvani, M. Mizrachi and H. Feldstein, *J. Cryst. Growth* (1994, in press).

## An Observation of Nanotwin Lamellae in $Cd_{0.6}Mn_{0.4}Te$ Crystal by Atomic Force Microscopy[1]

M.A. George*, M. Azoulay, W.E. Collins*, A. Burger* and E. Silberman*

Atomic force microscopy (AFM) is used to examine the structure of freshly cleaved $Cd_{0.6}Mn_{0.4}Te$ surfaces. The present report complements previous results obtained with X-ray diffraction and optical microscopy which showed the existence of microtwins. The AFM analysis was performed under ambient conditions and yielded nanometer scale resolution images of single twin lamellae that ranged between 20 and 100 nm in width. This is a first observation using AFM of such a substructure, which we interpret as evidence for the presence of nanotwins.

*Reference*

[1] M.A. George, M. Azoulay, W.E. Collins, A. Burger and E. Silberman, *J. Cryst. Growth* 130: 313 (1993).

## Micromorphology Study of Mercuric Iodide Crystals by Atomic Force Microscopy[1]

M. Azoulay, M.A. George*, H.N. Jayatirtha*, Y. Biao*, A. Burger*, E. Silberman* and D. Nason**

Atomic force microscopy was used to study the surfaces of mercuric iodide crystals at ambient. Various surface conditions were examined, including as-grown (001), (110), and (013) faces, and cleaved, chemically etched, vacuum etched, and aged (001) surfaces. As-grown (001) faces show a terraced structure and are smoother than as-grown (110) faces.

*Center for Photonic Materials and Devices, Dept. of Physics, Fisk University, Nashville, TN, USA.
**EG&G Energy Measurements Inc., Santa Barbara Operations, Goleta, CA, USA.

have to satisfy some 'compatibility' conditions that will guaranty that they correspond to localization of a smooth function (in addition to the conditions offered by the differential equation itself). Following the guidelines of this general scheme, it is natural to require that the discrepancy will be of the same order to magnitude as the error resulting from the Taylor approximation. Thus, we do not spend unnecessary computational effort on fitting the local expansions with discrepancy smaller than the error we expect for the given grid size and order of expansion. This feature of the new method is an attractive one in comparison with other existing methods, as it enables considerable saving in computation effort in addition to the advantage of specifying the accuracy of the obtained solution. Geometrical flexibility, which enables handling complex boundaries for a large variety of field problems, is another advantage of the proposed scheme.

The NTDM is applied to an irregular grid and, using an averaging process, the number of neighboring nodes may vary. The differential equation may be satisfied locally for each grid-point (the collocation method). An additional algorithm is introduced which enables implementing the differential equation by the method of weighted residuals. These features are introduced as an algorithm names here 'method A'. Another algorithm ('method B') is introduced, which is based on minimizing one target function that combines the requirements of compatibility and local satisfaction of the differential equation. The minimization is done by the Least Squares method in a way similar to that introduced for NTDM approximation of a given function.

The algorithms are implemented as a general purpose computer program applied to nonlinear steady state heat-conduction in two-dimensional space. A few test cases are solved numerically using this program. For the evaluation of the scheme, the results are compared with analytical solutions of one-dimensional cases. The results demonstrate that precision is enhanced when using the method of weighted residuals with an increased number of interrelated points. Two-dimensional examples with complex geometry and boundary conditions are then solved both by the NTDM and by the finite elements method. The results obtained by the two methods agree, and the importance of using various methods for solving the same problem was demonstrated. The results also indicate that the combination of controlled discrepancy between jets and the estimation of the truncation error, lead to improved efficiency. A test case that was solved by both methods A and B was used to evaluate the advantages and disadvantages of each of them, and an optimal order of using the two methods is suggested for achieving an accurate, yet rapid, solution.

*Reference*

[1] E. Kochavi, Ph.D. thesis, Ben-Gurion University of the Negev, Beer-Sheva (1993).

## Modified Algorithms for Nonconforming Taylor Discretization[1]

E. Kochavi, R. Segev* and Y. Yomdin**

Algorithms for solving partial differential equations which extend previous applications of the Nonconforming Taylor Discretization Method (NTDM) were developed. In one modification the number of interrelated grid points is variable, thus enabling additional geometric flexibility. Another modification is the approximation of the governing differential equation using the method of weighted residuals. A simple one-dimensional test case with a known analytic solution was solved using this code. The results demonstrated that precision is enhanced when using the method of weighted residuals with an increased number of interrelated points. The algorithm was applied as a general purpose two-dimensional code for nonlinear steady state heat-conduction. Two-dimensional examples with complex geometry and boundary conditions were then solved both by the NTDM and by the finite elements method, and the results obtained by the two methods were compared.

*Reference*

[1] E. Kochavi, R. Segev and Y. Yomdin, *Comput. Struct.* (1994, in press).

## Digital Stabilizer for Multichannel Analysis

R. Boneh, A. Gabovitch and D. Barak

Measuring isotopic concentrations using a gamma detector and a Multi Channel Analyzer (MCA) has an inherent error caused by the instability of the detector's gain. An inconvenient way to overcome this problem is to recalibrate the detector's MCA system before each measurement. In this work an algorithm (based upon instructions and guidance by Dr. Oded Shachal) with an appropriate computer program for solving the instability problem is presented. During calibration the peak of the measured energy spectrum is observed and noted. In the following measurements, the readings of all the channels are corrected by multiplication with the ratio between the current calculated peak and the reference peak. The results obtained using the computer program with an unstable detector, were practically identical to those obtained with a stable detector and no corrections. Also for a stable detector, no change was observed with or without implementing the correcting program.

*Ben-Gurion University of the Negev, Beer-Sheva.

**Weizmann Institute of Science, Rehovot.

## A Practical Estimation of the Reliability of GM Tubes

J. Paran, Y. Gabay, H. Kornfeld and D. Tirosh

The Mean Time Between Failures (MTBF) of a Geiger Muller (GM) tube was estimated in order to integrate a GM tube in a unique radiation detection alarm system. Since the system is located in a difficult-to-reach area, and has to be maintenance-free and unattended for a long period, an extraordinary demand for 99% reliability was made. Since the system's weakest component in terms of reliability is the GM tube, it was necessary to determine its MTBF as precisely as possible. Generally GM tubes are used in well maintained and frequently checked and calibrated instruments, and therefore the MTBF is usually not so significant. In our case, due to the reliability and long-term maintenance-free requirements, the MTBF had to be carefully estimated.

In order to obtain a dependable value, the MTBF was estimated in three different ways: *(a)* statistical analysis of similar well-known systems working with GM tubes for more than 10 years; *(b)* calculations of the performance of similar components under the same conditions with data taken from MIL HDBK 217E; *(c)* data from the IEEE STD 500 – 1984 handbook. The results of these estimates were very closely correlated. The GM tubes' manufacturer confirmed the results obtained by us according to the recording data they have from testing GM tubes over many years. The estimated MTBF for reliability calculations is: 6.2 failures / $10^6$ hours of operation.

## A Complete Behavior Model for Computer-Controlled Systems

R. Greenberg

A behavior description model for computer-controlled systems was developed. The model is based on Statecharts[1]. A general configuration of feedback systems is used for defining the basic states of the model. Feedback systems are characterized by a strong interaction between a controlling component (computer, in this case) and a controlled plant. The model is an adjustment of Statecharts that enables a representation of system behavior under normal (*nominal*) and failure (*disturbed*) conditions. This means that the *nominal* behavior is a part of our model and from this aspect the model is complete. In particular, incorrect mapping of the plant state into computer memory can be easily modeled. The model can be used for

analyzing systems in a very wide area of applications. It is also very useful in designing systems that must meet particular threshold values of safety, reliability, maintainability, etc.

*Reference*

[1] D. Harel, *Sci. Comp. Program.* 8: 231 (1987).

## Functional Independence in Safety-Critical Software Systems[1]

S. Carmona and R. Greenberg

The issue of independence of software functions in a critical computer-controlled system was considered. The acquisition of this feature is necessary to attain the objectives of high reliability and safety integrity. Two crucial problems were studied: *(a)* incorporation of independence, that is, preventing – as far as possible – a common-cause failure; and *(b)* assessment of independence to ensure that this safety feature is well incorporated. In order to handle these two problems, we envisaged a process based on the use of tools for software analysis, and carried out through the different development stages. A simplified example illustrated the application of this process, using the Decision Table for Transitions, Failure Mode and Effect Analysis (FMEA), and Software Failure Tree Analysis (SFTA).

Following the analytical approach, we considered factors, at the levels of the software functions and of the system components, which may inhibit or promote functional independence. We reviewed the difficulties encountered that are of serious consequence for software, since they may limit its availability to be assigned to the control of critical tasks.

*Reference*

[1] S. Carmona and R. Greenberg, *IAEA Technical Committee Meeting on Reliability of Computerized Safety Systems* (Vienna, Austria, June 1993).

## Strategy for Integrating Software Safety Analysis within the System Safety Analysis[1]

R. Greenberg and S. Carmona

A double phase strategy for conducting software safety analysis was developed. The first phase is aimed to insure that the design is correct from the point of view of safety. The purpose of the second phase is to identify hardware and system failures that may cause the software to issue wrong orders with severe consequences. The aim of the strategy is to overcome the current situation whereby software is treated as a 'black box' that carries out all

expected and required tasks. Moreover, with this strategy the system aspects of the analysis are always the main goal that has to be attained by the cooperation of all subsystems, regardless of their type. The strategy takes into account the unique properties of both the hardware and the software subsystems, as well as their interfaces. This treatment enables a single safety strategy for the entire system with respect to both correctness of safety design and components failures.

*Reference*

[1] R. Greenberg and S. Carmona, *IAEA Technical Committee on Reliability of Computerized Safety Systems* (Vienna, Austria, June 1993).

## Computerized Central Control and Supervision Room

M. Arad, M. Hollander and J. Oren

A high-reliability modern Central Control Room was established for the Nuclear Research Center – Negev (NRCN). A new control and supervision station was designed for easy operation, especially in critical events. Data received from all NRCN sites are processed by a Programmable Logic Controller (PLC) to produce a set of audio video signals, delivered to the operator through a set of synoptic panels on the control station and *via* host computer screens. A unique alarm system was designed to ensure special treatment to each individual alarm. A complex method integrating PLC with hardware circuits was developed to identify possible faults in the lines connecting the field units to the PLC I/O modules. Due to the NRCN high-reliability requirements, the primary PLC is backed up by a secondary PLC. In case the primary PLC fails, it can be easily interchanged with the secondary PLC. Both PLC units are backed up by Uninterruptable Power Supply. A special signal processing method was developed by dividing the PLC scan into several segments, to enable the reception of signals with a much shorter cycle time than normal PLC scan time.

The control system's design flexibility leaves room for future expansion.

## Control Software for the Pharmaceutical Industry

M. Arad, S. Milshtein, M. Hollander and J. Oren

A new chemical process software was designed for the Teva Pharmaceutical Industries Group – Plantex Ltd. Chemical and Pharmaceutical Works. The chemical process that produces gemfibrozil consists of three units: nitrile, gemfibrozil crude and gemfibrozil cryst.

New methods of defining the process were developed with Teva engineers. The process was split into several comprehensible units and a set of rules was defined to communicate among them. The control system configuration includes a Programmable Logic Controller (PLC) type 781 (General Electric) and a Man Machine Interface type WIZCON 4.1 of PCSOFT, and deals with approximately 1000 I/O points, 150 of which are analog ones. Software was designed in a new modular way and special attention was given to simplify the system for easier future maintenance. Complicated analog control loops in cascade configuration were designed for temperature control, pH control, flow control, etc. The software was developed to meet the class 1 DEV II safety standards. In addition, new software methods were developed to meet the requirements of validation of the drug industry, as defined by the Food and Drug Administration of the U.S.A.

# *IX*

# *DOCUMENTATION*

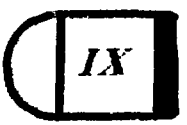

# DOCUMENTATION

The following publications were issued during the period January-December 1993. Asterisks indicate authors affiliated with other institutions.

## IAEC REPORTS

IA-1467

CHOMSKY, D.

Photorefractive effect in semiconductors and spectral effect in photorefractive two-beam coupling. (Ph.D. thesis; Hebrew, with English summary).

IA-1472

SHAFIR, E.

Light coupling between two polarization maintaining fibers. (Ph.D. thesis; Hebrew, with English summary).

IA-1476

LEVI, O.

Comparison between Nd:YLF and Nd:YAG diode pumped lasers. (M.Sc. thesis; Hebrew).

IA-1479

ARENSBURG, A.

Experimental and theoretical study of plasma-water interaction in electrothermal guns. (Ph.D. thesis; Hebrew, with English summary).

IA-1481

RESEARCH LABORATORIES ANNUAL REPORT, 1992.

IA-1482

WERDIGER, M.

Decay of a laser generated shock wave in an aluminum target. (M.Sc. thesis; Hebrew, with English summary).

NRCN-574

GANOR, M.

Manufacturing and properties of a FE-SiC composite material. (Hebrew, with English summary).

NRCN-613

YEHESKEL, J., AGAM, S., EDELSTEIN, D., LEIBOVITZ, O., RON, Y. and DARIEL, M.S.
Coatings for HTR fuel elements: Silicon-carbide and pyrocarbon deposition and fluidized-bed dynamics.

NRCN-614

GAL, G.
Room temperature kinetics of the $B_2H_6/O(^3P)$ system. (Hebrew, with English summary).

NRCN-615

KARP, B.
Sub-millimetric gap width measurement by finite X-ray source. (Hebrew, with English summary).

NRCN-616

KUZNIETZ, M., PINTO, H., ETTEDGUI, H. and MELAMUD, M.
The magnetic phase diagram of the $U(Ni_{1-x}Cu_x)_2Ge_2$ system studied by ac-susceptibility and neutron diffraction of polycrystalline samples.

NRCN(ER)-030

SKIBIN, D. and CALAF, M.
Sampling rate of data loggers in wind energy surveys. (Hebrew, with English summary).

NRCN(LS)-016

RAM, V.
Welding by continuous-wave $CO_2$ laser beam - Literature survey. (Hebrew, with English summary).

NRCN(TN)-142

BEN-SHACHAR, B., GERMAN, U., RACHMIAN, Y. and NAIM, E.
Reassessment of high and intermediate doses by the residual dose and the PTTL. (Hebrew, with English summary).

NRCN(TN)-144

BOGER, Z.
Possible roles of neural networks in developing expert systems for the nuclear industry.

NRCN(TN)-145

BOGER, Z.
The role of neural networks in nuclear power plant safety systems.

NRCN(TN)-146

TAMSUT, S., FEUERLICHT, Y., GANOR, M., KALIR, D. and YEHESKEL, O.

Design and construction of an experimental HIP system comprising in-situ ultrasonic sound wave velocity measurements. (Hebrew, with English summary).

NRCN(TN)-147

HAYON, J., OZER, D., MOR, U., YDGAR, R., MAOR, Y. and BETTELHEIM, A.

The effectiveness of a commercial magnetic and catalytic device in suppressing $CaCO_3$ scale deposition and corrosion rate. (Hebrew, with English summary).

## PAPERS PUBLISHED IN JOURNALS, BOOKS, REPORTS AND CONFERENCE PROCEEDINGS

ACHIAM, Y. and SOUTHERN*, B.W.

Critical dynamics of the alternating bond kinetic Ising model.
*J. Phys., A Math. Gen.* 25 (13), L769-L773 (1992).

AKKERMAN, A., BRESKIN*, A., CHECHIK*, R. and GIBREKHTERMAN*, A.

Secondary electron emission from alkali halides induced by X-rays and electrons.
In: Ionization of Solids by Heavy Particles. NATO Advanced Research Workshop on Ionization of Solids by Heavy Particles (Taormina, Italy, 1-5 Jun. 1992). Proceedings. New York, NY, Plenum, 1993. pp. 359-380.

AKKERMAN, A., LEVINSON, J., ILBERG, D. and LIFSHITZ, Y.

Track effects and their influence on heavy ion energy losses in semiconductor devices.
In: Ionization of Solids by Heavy Particles. NATO Advanced Research Workshop on Ionization of Solids by Heavy Particles (Taormina, Italy, 1-5 Jun. 1992). Proceedings. New York, NY, Plenum, 1993. pp. 431-438.

ALON, U., SHVARTS, D. and MUKAMEL, D.

Scale-invariant regime in Rayleigh-Taylor bubble-front dynamics.
*Phys. Rev., E* 48 (2), 1008-1014 (1993).

ARENSBURG, A., WALD, S. and GOLDSMITH*, S.

X-ray diagnostics of a plasma-jet-liquid interaction in electrothermal guns.
*J. Appl. Phys.* 73 (5), 2145-2154 (1993).

ASHKENAZY, J.

The effect of the external pressure on the internal conditions inside the discharge tube.
*IEEE Trans. Magn.* 29 (1), 539-543 (1993).

AVIDA, R., FRIEDMAN, M., ALGOM*, A., MATMOR, A., KARPAS, Z. and SHAHAL, O.

Spectrometer.
U.S. Patent No. 5,235,182 issued Aug. 10, 1993.

AZOULAY*, A., ATZMONY, U., MINTZ, M.H. and SHAMIR, N.
Oxygen-induced surface segregation of hydrogen in polycrystalline titanium.
*Surf. Interface Anal.* 18 (9), 643-649 (1992).

AZOULAY, M., GEORGE*, M.A., BURGER*, A., COLLINS*, W.E. and SILBERMAN*, E.
Surface morphology study on CdZnTe single crystals by atomic force microscopy.
*J. Vac. Sci. Technol., B* 11 (2), 148-151 (1993).

AZOULAY, M., GEORGE*, M.A., JAYATIRTHA*, H.N., BIAO*, Y., BURGER*, A., SILBERMAN*, E. and NASON*, D.
Micromorphology study of mercuric iodide crystals by atomic force microscopy.
*J. Vac. Sci. Technol., B* 11 (5), 1782-1787 (1993).

AZOULAY, M., RAIZMAN, A., WEINGARTEN, R., SHACHAM, H. and FELDSTEIN, H.
The growth of a cubic, single phase, $Cd_{0.6}Mn_{0.4}Te$ single crystal by the vertical gradient freeze method.
10. International Conference on Crystal Growth (San Diego, CA, USA, 16-21 Aug. 1992).
*J. Cryst. Growth* 128 (1-4), Pt. 2, 588-592 (1993).

BARAM, A., LAST, I. and BAER, M.
Quantum-mechanical cross sections for the $D+H_2$ and $H+D_2$ reactive systems. Application of the negative imaginary potentials within the $j_z$ approximation.
*Chem. Phys. Lett.* 212 (6), 649-653 (1993).

BLAU, P., SMILANSKI, I., GABAY, S. and ROSENWAKS*, S.
Radially and temporally resolved measurements of electron density and gas temperature in a copper-vapor laser.
In: Conference on Lasers and Electro-Optics (Baltimore, MD, USA, 2-7 May 1993). OSA Technical Digest Series 11, pp. 456-458.

BLOCH, J., JACOB*, I. and MINTZ, M.H.
The effect of vacuum annealing on the hydriding kinetics of zirconium.
*J. Alloys Comp.* 191 (2), 179-186 (1993).

BOURDON*, E.B.D., RAVEH, A., GUJRATHI*, S.C. and MARTINU*, L.
Etching of a-C:H films by an atomic oxygen beam.
*J. Vac. Sci. Technol., A* 11 (5), 2530-2535 (1993).

BURSHTEIN, Z., SHIMONY, Y. and LEVY, I.

Refractive-index anisotropy and dispersion in gehlenite, $Ca_2Al_2SiO_7$, between 308 and 1064 nm.

*J. Opt. Soc. Am., A Opt. Image Sci.* 10 (10), 2246-2247 (1993).

BURSHTEIN, Z., SHIMONY, Y., MORGAN*, S., HENDERSON*, D.O., MU*, R. and SILBERMAN*, E.

Symmetry lowering due to site-occupation disorder in vibrational spectra of gehlenite, $Ca_2(AlSi)AlO_7$.

*J. Phys. Chem. Solids* 54 (9), 1043-1049 (1993).

CUPERMAN*, S., ZOLER*, D., ASHKENAZY, J., CANER, M. and KAPLAN, Z.

Consistent treatment of critical plasma flows in high pressure discharge ablative capillaries.

*IEEE Trans. Plasma Sci.* 21 (3), 282-288 (1993).

DEKA*, C., BASS*, M., CHAI*, B.H.T. and SHIMONY, Y.

Optical spectroscopy of $Cr^{4+}$:$Y_2SiO_5$.

*J. Opt. Soc. Am., B: Opt. Phys.* 10 (9), 1499-1507 (1993).

DONG*, X.P., EDWARDS*, H.O., SHAFIR, E. and DAKIN*, J.P.

Broadband sources for gas detection using fluorescent rare-earth-doped fibres pumped by low-cost semiconductor laser source.

In: 9. Optical Fiber Sensors Conference (Florence, Italy, 4-6 May 1993). Proceedings. pp. 209-213.

EGER, D., ORON, M. and KATZ, M.

Optical characterization of $KTiOPO_4$ periodically segmented waveguides for second-harmonic generation of blue light.

*J. Appl. Phys.* 74 (7), 4298-4302 (1993).

EISEN, Y. and POLAK, E.

An array of CdTe detectors for imaging applications.

*Mat. Res. Soc. Symp. Proc.* 302, 487-495 (1993). Symposium on Semiconductors for Room-Temperature Radiation Detector Applications (San Francisco, CA, USA, 12-16 Apr. 1993).

EISENBACH, S., LOTEM, H., HORVITZ, Z., MIRON, G., LANDO, M. and GABAY, S.
Thermally induced window birefringence in high-power copper vapor laser.
In: 8. Meeting on Optical Engineering in Israel: Optoelectronics and Applications in Industry and Medicine (Tel-Aviv, Israel, 14-16 Dec. 1992).
*Proc. SPIE* 1972, 13-26 (1993).

ELIEZER, S., GILATH, I. and GAZIT, Y.
Laser induced shock waves and dynamic damage.
In: Laser Interaction and Related Plasma Phenomena. Ed. by G.H. Miley and H. Hora. New York, NY, Plenum, 1992. Vol. 10, pp. 637-647.

ELIEZER, S. and HENIS, Z.
X-ray lasing in a muon catalyzed fusion system.
In: Laser Interaction and Related Plasma Phenomena. Ed. by G.H. Miley and H. Hora. New York, NY, Plenum, 1992. Vol. 10, pp. 137-149.

ELIEZER, S. and HORA*, H.
The physics of directly driven targets.
In: Nuclear Fusion by Inertial Confinement. A comprehensive treatise. Ed. by G. Velarde, I. Ronen and J.M. Martinez-Val. Boca Raton, FL, USA, CRC Press, 1993. pp. 43-71.

FASTIG, S., BENAYAHU, Y., ENGLANDER, A. and GLASER*, E.
Aerosol density distribution in the boundary layer measured by a scanning LIDAR system.
In: 8. Meeting on Optical Engineering in Israel: Optical Engineering and Remote Sensing (Tel-Aviv, Israel, 14-16 Dec. 1992).
*Proc. SPIE* 1971, 61-67 (1993).

GAEDE*, W., ELDIK*, R. van, COHEN, H. and MEYERSTEIN*, D.
Anion-catalyzed heterolysis of chromium-carbon $\sigma$ bonds. Effect of different anions, temperature, and pressure.
*Inorg. Chem.* 32 (10), 1997-2000 (1993).

GAEDE*, W., GERHARD*, A., ELDIK*, R. van, COHEN, H. and MEYERSTEIN*, D.
Influence of acetate ion on the formation reactions of organochromium(III) species. A rapid-scan and high-pressure pulse-radiolysis study.
*J. Chem. Soc., Dalton Trans.* (13), 2065-2070 (1993).

GEORGE*, M.A., AZOULAY, M., BURGER*, A., BIAO*, Y., SILBERMAN*, E. and NASON*, D.

Optical properties and surface morphology studies of palladium contacts on mercuric iodide single crystals.

*Thin Solid Films* 236 (1/2), 180-183 (1993).

GEORGE*, M.A., AZOULAY, M., COLLINS*, W.E., BURGER*, A. and SILBERMAN*, E.

An observation of nanotwin lamellae in $Cd_{0.6}Mn_{0.4}Te$ crystal by atomic force microscopy.

*J. Cryst. Growth* 130 (1/2), 313-316 (1993).

GIBREKHTERMAN*, A., AKKERMAN, A., BRESKIN*, A. and CHECHIK*, R.

Characteristics of secondary electron emission from CsI induced by X-rays with energies up to 100 keV.

*J. Appl. Phys.* 74 (12), 7506-7509 (1993).

GILATH, I., ELIEZER, S. and BAR-NOY, T.

Hemispherical shock wave decay in laser-matter interaction.

*Laser Part. Beams* 11 (1), 221-225 (1993).

GILATH, I., ELIEZER, S., BAR-NOY, T., ENGLMAN, R. and JAEGER, Z.

Material response at hypervelocity impact conditions using laser induced shock waves.

*Int. J. Impact Eng.* 14 (1-4), 279-289 (1993).

GILATH, I., ELIEZER, S., BAR-NOY, T., ENGLMAN, R. and JAEGER, Z.

Behavior of materials at dynamic stress conditions using laser-induced shock waves.

In: 8. Meeting on Optical Engineering in Israel: Optoelectronics and Applications in Industry and Medicine (Tel-Aviv, Israel, 14-16 Dec. 1992).

*Proc. SPIE* 1972, 343-353 (1993).

GILIBERT, M., BARAM, A., LAST, I., SZICHMAN, H. and BAER, M.

The application of Toeplitz matrices to scattering problems.

*J. Chem. Phys.* 99 (5), 3503-3508 (1993).

GLICK, Y. and STERNKLAR, S.

Angular field of view for Brillouin amplification.
In: 8. Meeting on Optical Engineering in Israel: Optoelectronics and Applications in Industry and Medicine (Tel-Aviv, Israel, 14-16 Dec. 1992).
*Proc. SPIE* 1972, 27-34 (1993).

GOLDSTEIN*, S., CZAPSKI*, G., COHEN, H. and MEYERSTEIN*, D.

Free radical induced cleavage of organic molecules catalyzed by copper ions. – An alternative pathway for biological damage.
In: Bioinorganic Chemistry of Copper. Ed. by K.D. Karlin and Z. Tyeklar. New York, NY, Chapman & Hall, 1993. pp. 222-235.

GOLDSTEIN*, S., CZAPSKI*, G., COHEN, H., MEYERSTEIN*, D. and SHAIK*, S.

Effect of *N*-alkylation on the rate of β-amine elimination from transients with $Cu^{II}$-carbon σ bonds.
*J. Chem. Soc., Faraday Trans.* 89 (22), 4045-4051 (1993).

GREENBERG, S. and GUTERMAN*, H.

Position invariant correlation using a neural network.
In: World Congress on Neural Networks (Portland, OR, USA, 11-15 Jul. 1993). Vol. 3, pp. 745-748.

GREST*, G.S. and MURAT, M.

Structure of grafted polymeric brushes in solvents of varying quality: A molecular dynamics study.
*Macromolecules* 26 (12), 3108-3117 (1993).

GVISHI*, R., REISFELD*, R., BURSHTEIN, Z. and MIRON, E.

New stable tunable solid-state dye laser in the red.
In: 8. Meeting on Optical Engineering in Israel: Optoelectronics and Applications in Industry and Medicine (Tel-Aviv, Israel, 14-16 Dec. 1992).
*Proc. SPIE* 1972, 390-399 (1993).

HAYON, J., RAVEH, A. and BETTELHEIM, A.

Electrocatalytic properties of chemically polymerized films of cobalt, iron and manganese tetrakis (*o*-aminophenyl) porphyrins.
*J. Electroanal. Chem.* 359 (1-2), 209-221 (1993).

HENIS, Z. and ELIEZER, S.

Melting phenomenon in laser-induced shock waves.
*Phys. Rev., E* 48 (3), 2094-2097 (1993).

HOROWITZ, A. and HOROWITZ*, Y.S.

Elimination of the high temperature glow peak in LiF:Cu,Mg,P.
10. International Conference on Solid State Dosimetry (Washington, DC, USA, 13-17 Jul. 1992).
*Radiat. Prot. Dosim.* 47 (1/4), 69-72 (1993).

HOROWITZ*, Y.S., BEN-SHACHAR, B. and YOSSIAN*, D.

Study of the long-term stability of peaks 4 and 5 in TLD-100 - Correlation with isothermal decay measurements at elevated temperatures.
*J. Phys., D Appl. Phys.* 26 (9), 1475-1481 (1993).

JACKEL, S., SHALEV, P. and LALLOUZ, R.

Experimental and theoretical investigation of statistical fluctuations in phase conjugate mirror reflectivity.
*Opt. Commun.* 101 (5/6), 411-415 (1993).

JACKEL, S., SHALEV, P. and LALLOUZ, R.

Experimental and theoretical investigation of statistical fluctuations in phase conjugate mirror reflectivity.
In: 8. Meeting on Optical Engineering in Israel: Optoelectronics and Applications in Industry and Medicine (Tel-Aviv, Israel, 14-16 Dec. 1992).
*Proc. SPIE* 1972, 35-41 (1993).

JAEGER, Z., ANHOLT, M. and MAYER*, A.H.

Impact of fiber composite laminate plates: A percolation view of perforation and spallation.
In: Army Research Office Workshop on Dynamic Response of Composite Structures (New Orleans, LA, USA, 30 Aug.-1 Sep. 1993). pp. 33-34.

JAFFE, I.

Aryl diisocyanide organometallic coordination polymers.
*Rev. Inorg. Chem.* 13 (1), 1-76 (1993).

KAPLAN, Z., SAPHIER, D., MELNIK, D., GORELIC, Z., ASHKENAZY, J., SUDAI, M., KIMHE, D., MELNIK, M., SMITH*, S. and JUHASZ*, A.

Electrothermal augmentation of a solid propellant launcher.

*IEEE Trans. Magn.* 29 (1), 573-578 (1993).

KARPAS, Z., EICEMAN*, G.A., EWING*, R.G., ALGOM*, A., AVIDA, R., FRIEDMAN, M., MATMOR, A. and SHAHAL, O.

Ion distribution profiles in the drift region of an ion mobility spectrometer.

*Int. J. Mass Spectrom. Ion Process.* 127 (Aug. 19), 95-104 (1993).

KARPAS, Z., EICEMAN*, G.A., HARDEN*, C.S. and EWING*, R.G.

On the structure of water-alcohol and ammonia-alcohol protonated clusters.

*J. Am. Soc. Mass Spectrom.* 4 (6), 507-512 (1993).

KARPAS, Z., WANG*, Y.F. and EICEMAN*, G.A.

Qualitative and quantitative response characteristics of a capillary gas chromatograph/ion mobility spectrometer to halogenated compounds.

*Anal. Chim. Acta* 282 (1), 19-31 (1993).

KATZ, Y., KELLER*, R.R., HUANG*, H. and GERBERICH*, W.W.

A dislocation shielding model for the fracture of semibrittle polycrystals.

*Metall. Trans., A* 24 (2), 343-350 (1993).

KOLKA, E., ELIEZER, S. and PAISS, Y.

Inertial plasma confinement in a miniature magnetic bottle induced by circularly polarized laser light.

*Phys. Lett., A* 180 (1/2), 132-136 (1993).

KRUPKIN*, V., THOMPSON*, G., YOGEV*, A. and ORON, M.

Compound parabolical concentrator as pumping device for solid-state solar lasers.

In: 8. Meeting on Optical Engineering in Israel: Optical Engineering and Remote Sensing (Tel-Aviv, Israel, 14-16 Dec. 1992).

*Proc. SPIE* 1971, 400-407 (1993).

KUZNIETZ, M., ANDRE*, G., BOURFE*, F., PINTO, H., ETTEDGUI, H. and MELAMUD, M.

Magnetic structure of the solid solution $UNiCuSi_2$: Neutron diffraction versus ac-susceptibility measurements.

37. Annual Conference on Magnetism and Magnetic Materials (Houston, TX, USA, 1-4 Dec. 1992).

*J. Appl. Phys.* 73 (10, Pt. IIA), 6075-6077 (1993).

KUZNIETZ, M., ANDRE*, G., BOUREE*, F., PINTO, H., ETTEDGUI, H. and MELAMUD, M.

Magnetic properties of $U(Ni_{1-x}Cu_x)_2Si_2$ solid solutions in the vicinity of $x = 0.50$ studied by neutron diffraction and ac-susceptibility.

*Solid State Commun.* 87 (8), 689-693 (1993).

KUZNIETZ, M., PINTO, H., ETTEDGUI, H. and MELAMUD, M.

Magnetic phase diagram of the $U(Ni_{1-x}Cu_x)_2Ge_2$ system studied by ac-susceptibility measurements and neutron diffraction of polycrystalline samples.

*Phys. Rev., B* 48 (5), 3183-3189 (1993).

KUZNIETZ, M., PINTO, H. and MELAMUD, M.

Note on the magnetism of $UCu_2Ge_2$.

*Philos. Mag. B* 68 (2), 195-201 (1993).

KWEI*, T.K., LEVON*, K., TESORO*, G., LIU*, F., MEY-MAROM, A. and MUNUKUTLA*, S.

Molecular composites in thermosets.

In: Polymers for Advanced Technologies. New York, NY, Wiley, 1993. Vol. 4, pp. 537-547.

LANDO, M., EISENBACH, S. and GABAY, S.

Universal presentation of laser gain saturation laws.

In: Symposium on Laser Resonators and Coherent Optics: Modeling, Technology, and Applications (Los Angeles, CA, USA, 18-20 Jan. 1993).

*Proc. SPIE* 1868, 143-149 (1993).

LAST, I., BARAM, A., SZICHMAN, H. and BAER, M.

Three-dimensional reactive quantum mechanical study for the $H+X_2(X=H,D,T)$ systems: Application of negative imaginary arrangement decoupling potentials.

*J. Phys. Chem.* 97 (27), 7040-7047 (1993).

LAVI, R., JACKEL, S., TSADKA, S., LEVI, O. and LALLOUZ, R.

Comparison between Nd:YAG and Nd:YLF laser oscillators, end pumped by high brightness diode laser arrays.

In: 8. Meeting on Optical Engineering in Israel: Optical Engineering and Remote Sensing (Tel-Aviv, Israel, 14-16 Dec. 1992).

*Proc. SPIE* 1971, 326-336 (1993).

LAWRENCE*, J.R., ELDAN, M. and SONZOGNI*, W.C.

Metribuzin and metabolites in Wisconsin (U.S.A.) well water.

*Water Res.* 27 (8), 1263-1268 (1993).

LEMPERT, G.D., LIFSHITZ, Y., ROTTER, S., ARMINI*, A.J. and BUNKER*, S.

Tribological evaluation of hydrogen-free ion beam deposited diamondlike carbon coatings

8. International Conference on Ion Beam Modification of Materials (Heidelberg, Germany, 7-11 Sep. 1992).

*Nucl. Instrum. Methods Phys. Res., Sect. B* 80/81 (Pt. II), 1502-1506 (1993).

LEMPERT, G.D. and TSOUR*, A.

Reduction of static friction between surfaces of Ti–6Al–4V and between surfaces of Ti–6Al–4V and Al-7075.

*Surf. Coat. Technol.* 52, 291-295 (1992).

LEVINSON, J., AKKERMAN, A., VICTORIA*, M., HASS*, M., ILBERG, D., ALURRALDE*, M., HENNECK*, R. and LIFSHITZ, Y.

New insight into proton-induced latchup: Experiment and modeling.

*Appl. Phys. Lett.* 63 (21), 2952-2954 (1993).

LEVRON, D., BAR-SHALOM, A., BURSHTEIN, Z., DAVID, R., HAZAK, G., IVRY, J., LEVIN, L.A., OREG, J. and STRAUSS, M.

Photo flux optimization in three-color multiphoton ionization of uranium atoms.

In: Laser Isotope Separation. Ed. by J.A. Paisser.

*Proc. SPIE* 1859, 69-78 (1993).

LIFSHITZ, Y., LEMPERT, G.D., ROTTER, S., AVIGAL*, I., UZAN-SAGUY*, C. and KALISH*, R.

The influence of substrate temperature during ion beam deposition on the diamond-like or graphitic nature of carbon films.

*Diamond Related Mater.* 2 (2/4), 285-290 (1993).

LIFSHITZ, Y., LEVINSON, J., NOTER, Y., SHAMAI, Y., AKKERMAN, A., EVEN, O., ZENTNER, A., ISRAELI, M., GIBREKHTERMAN*, A. and SINGER*, L.

A portable planar Sr-90 irradiation setup for total dose testing of electronic devices. International Nuclear and Space Radiation Effects Conference, NSREC'93, (Snowbird, UT, USA, 19-23 Jul. 1993).

*IEEE Trans. Nucl. Sci.* 40 (6, Pt. 1), 1388-1392 (1993).

LIFSHITZ, Y., ROUX*, C.D., BOYD*, K., ECKSTEIN*, W. and RABALAIS*, J.W.

Analysis of carbon film growth from low energy ion beams using dynamic trajectory simulations and Auger electron spectroscopy.

*Nucl. Instrum. Methods Phys. Res., Sect. B* 83 (3), 351-356 (1993).

LOTEM, H., PAN*, Z. and DAGENAIS*, M.

Tunable external cavity diode laser that incorporates a polarization half-wave plate.

*Appl. Opt.* 31 (36), 7530-7532 (1992).

LOTEM, H., PAN*, Z. and DAGENAIS*, M.

Tunable dual-wavelength continuous-wave diode laser operated at 830 nm.

*Appl. Opt.* 32 (27), 5270-5273 (1993).

LOTEM, H. and RABINOVITCH*, K.

Penta prism laser polarizer.

*Appl. Opt.* 32 (12), 2017-2020 (1993).

MAHAJNA*, S., YOSSIAN*, D., HOROWITZ*, Y.S. and HOROWITZ, A.

Kinetic trapping parameters in LiF:Mg,Cu,P via "prompt" and "residual" isothermal decay.

10. International Conference on Solid State Dosimetry (Washington, DC, USA, 13-17 Jul. 1992).

*Radiat. Prot. Dosim.* 47 (1/4), 73-77 (1993).

MARTINU*, L., RAVEH, A., BOUTARD*, D., HOULE*, S., POITRAS*, D., VELLA*, N. and WERTHEIMER*, M.R.

Properties and stability of diamond-like carbon films related to bonded and unbonded hydrogen.

*Diamond Related Mater.* 2 (2/4), 673-677 (1993).

MASSALKER*, Y., SEMBIRA, A.N. and BARAM*, J.C.

Characterization of superconducting BiSrCaCuO (2212 and 2223) prepared from amorphous plates by splat quenching.

2. Israeli International Conference on High-Temperature Superconductivity (Eilat, Israel, 4-7 Jan. 1993).

*Physica C* 209 (1-3), 295-300 (1993).

MORENO, D., ABRAMOV, E. and ELIEZER*, D.

A study of the influence of near-surface He concentration on the blistering formation in cube.

*Scr. Metall. Mater.* 27 (8), 1039-1044 (1992).

NAHOR, G., BAER, M., ANHOLT, M., MURAT, M., NOTER, Y., LIFSHITZ, Y., SAAR*, N. and BRAUN*, O.

Degradation of TAUVEX optical system performance due to contamination by outgassed spacecraft materials.

In: 8. Meeting on Optical Engineering in Israel: Optical Engineering and Remote Sensing (Tel-Aviv, Israel, 14-16 Dec. 1992).

*Proc. SPIE* 1971, 288-303 (1993).

NOTER, Y., NAHOR, G., LIFSHITZ, Y., SAAR*, N. and BRAUN*, O.

Contamination control approach for the TAUVEX UV astronomical telescope.

In: 8. Meeting on Optical Engineering in Israel: Optical Engineering and Remote Sensing (Tel-Aviv, Israel, 14-16 Dec. 1992).

*Proc. SPIE* 1971, 276-287 (1993).

NOWIK*, I., JACOB*, I. and MOREH, R.

Mossbauer study of crystallographic and magnetic phase transitions, phonon softening, and hyperfine interactions in $Zr(Al_xFe_{1-x})_2$.

*Phys. Rev., B* 47 (2), 723-726 (1993).

OSTER*, L., HOROWITZ*, Y.S. and HOROWITZ, A.

Glow curve readout of LiF:Mg,Cu,P (GR-200) chips at maximum temperatures between 240°C and 280°C: Elimination of the residual signal.

*Radiat. Prot. Dosim.* 49 (4), 407-411 (1993).

RAVEH, A.

Mechanism of rf plasma nitriding of Ti–6Al–4V alloy.

*Mater. Sci. Eng., A Struct. Mater.* 167 (1/2), 155-164 (1993).

RAVEH, A., BUSSIBA, A., BETTELHEIM, A. and KATZ, Y.

Plasma-nitrided $\alpha$–$\beta$ Ti alloy: layer characterization and mechanical properties modification.

*Surf. Coat. Technol.* 57 (1), 19-29 (1993).

RAVEH, A., MARTINU*, L., DOMINGUE*, A., WERTHEIMER*, M.R. and BERTRAND*, L.

Fourier transform infrared photoacoustic spectroscopy of amorphous carbon films.

In: Photoacoustic and Photothermal Phenomena III. Springer Series in Optical Sciences, Vol. 69. Ed. by D. Bicanic. Berlin, Germany, Springer-Verlag, 1992. pp. 151-154.

RAVEH, A., MARTINU*, L., HAWTHORNE*, H.M. and WERTHEIMER*, M.R.

Mechanical and tribological properties of dual-frequency plasma deposited diamond-like carbon.

*Surf. Coat. Technol.* 58, 45-55 (1993).

RAVID, A., SHER, A., CINADER, G. and ZUSSMAN, A.

Optically pumped laser action and photoluminescence in HgCdTe layer grown on (211) CdTe by metalorganic chemical vapor deposition.

*J. Appl. Phys.* 73 (11), 7102-7107 (1993).

RAVID, A. and ZUSSMAN, A.

Laser action and photoluminescence in an indium-doped n-type $Hg_{1-x}Cd_xTe$ (x=0.375) layer grown by liquid phase epitaxy.

*J. Appl. Phys.* 73 (8), 3979-3987 (1993).

ROSENBERG*, Y., SIEGMANN*, A., NARKIS*, M. and SHKOLNIK, S.

Low dose $\gamma$-irradiation of some fluoropolymers: Effect of polymer chemical structure.

*J. Appl. Polym. Sci.* 45 (5), 783-795 (1992).

ROTMAN*, S.R., EYAL*, A., KALISKY, Y.Y., BRENIER*, A., PEDRINI*, C., BOULON*, G. and HARTMANN*, F.X.

$Tm^{+3}$ decay in chromium-thulium-holmium-doped yttrium aluminum garnet at liquid helium temperatures.

In: 8. Meeting on Optical Engineering in Israel: Optoelectronics and Applications in Industry and Medicine (Tel-Aviv, Israel, 14-16 Dec. 1992).

*Proc. SPIE* 1972, 2-12 (1993).

ROZEN, S., SAPHIER, D. and SHER*, E.

Burning rate of double-base propellant in the presence of plasma.
In: 33. Israel Annual Conference on Aviation and Astronautics (Haifa, Israel, 24-25 Feb. 1993). Collection of Papers. Ed. by A. Burcat. pp. 154-158.

RUPPIN, R.

Optical absorption by a small sphere above a substrate with inclusion of nonlocal effects.
*Phys. Rev., B* 45 (19), 11209-11215 (1992).

SARUSSI*, D., JACOB*, I., BLOCH, J., SHAMIR, N. and MINTZ, M.H.

The kinetics and mechanism of cerium hydride formation.
*J. Alloys Comp.* 191 (1), 91-99 (1993).

SHAFIR, E., SHAKED, N., BEN-KISH*, A. and TUR*, M.

The response of Faraday-effect fiber-optic current sensors to noncentered currents.
In: 9. Optical Fiber Sensors Conference (Florence, Italy, 4-6 May 1993). Proceedings. pp. 435-438.

SHAKED, H., JORGENSEN*, J.D., HUNTER*, B.A., HITTERMAN*, R.L., KINOSHITA*, K., IZUMI*, F. and KAMIYAMA*, T.

Defect structure and superconducting properties of $La_{1.8}Sr_xCa_{1.2-x}Cu_2O_{6-\delta}$.
*Phys. Rev., B* 48 (17), 12941-12950 (1993).

SHAPPIR*, J., ROTER*, T. and LEVINSON, J.

Radiation and high field induced interface state generation in MOS structures with modified nitrided oxide.
8. Biennial Conference on Insulating Films on Semiconductors - INFOS'93 (Delft, the Netherlands, 2-5 Jun. 1993).
*Microelectron. Eng.* 22 (1-4), 219-222 (1993).

SHIMONY, Y.

$Cr^{4+}$ doped crystals for laser applications.
In: 8. Meeting on Optical Engineering in Israel: Optoelectronics and Applications in Industry and Medicine (Tel-Aviv, Israel, 14-16 Dec. 1992).
*Proc. SPIE* 1972, 139-150 (1993).

SHKOLNIK, S. and BARASH, C.

Electrocoating of carbon fibres with polymers: 3. Electrocopolymerization of polyfunctional monomers.

*Polymer* 34 (14), 2921-2928 (1993).

SHKOLNIK, S. and HOCKER*, H.

Electrocoating of carbon fibres with polymers: 2. Electrocopolymerization of monofunctional monomers.

*Polymer* 33 (8), 1669-1675 (1992).

SOUTHERN*, B.W. and ACHIAM, Y.

Critical dynamics of the d = 1 kinetic Ising model.

*J. Phys., A Math. Gen.* 26 (11), 2505-2517 (1993).

SOUTHERN*, B.W. and ACHIAM, Y.

Critical dynamics and universality in kinetic Ising models without translational invariance.

*J. Phys., A Math. Gen.* 26 (11), 2519-2533 (1993).

STEINITZ*, G., VULKAN, U., LANG*, B., GILAT*, A. and ZAFRIR, H.

Radon emanation along border faults of the Rift in the Dead Sea area.

*Isr. J. Earth-Sci.* 41 (1), 9-20 (1992).

STERNKLAR, S.

Double phase conjugate mirror, double colour-pumped oscillator and high-power beam steering by Brillouin four-wave mixing.

*Nonlinear Opt.* 5, 79-87 (1993).

STOTLAND*, A., BAHAR*, J., EISENBERG, E. and RUBINFELD, S.

Development of radiation-sterilized mannitol salt agar dip slide kits.

*J. Radiat. Steril.* 1 (1), 5-10 (1992).

STRAUSS*, H.R., ELIEZER, S., PAISS, Y. and FRUCHTMAN*, A.

Generation of magnetic field by circularly polarized light and thermomagnetic instability in a laser plasma.

In: Laser Interaction and Related Plasma Phenomena. Ed. by G.H. Miley and H. Hora. New York, NY, Plenum, 1992. Vol. 10, pp. 167-170.

TSADKA, S., LAVI, R. and JACKEL, S.

Modeling of diode end pumped CW and Q-switched Nd:YAG laser oscillators.
In: 8. Meeting on Optical Engineering in Israel: Optical Engineering and Remote Sensing (Tel-Aviv, Israel, 14-16 Dec. 1992).
*Proc. SPIE* 1971, 314-325 (1993).

TUR*, M., BEN-KISH*, A., SHAFIR, E. and SHAKED, N.

Faraday-rotation fiber optic current sensor: response to different locations of the conductor.
In: 8. Meeting on Optical Engineering in Israel: Optoelectronics and Applications in Industry and Medicine (Tel-Aviv, Israel, 14-16 Dec. 1992).
*Proc. SPIE* 1972, 324-327 (1993).

WALACH*, N. and GUR, Y.

Leukocyte alkaline phosphatase and carcinoembryonic antigen in lung cancer patients.
*Oncology* 50, 279-284 (1993).

WALACH*, N., GUTERMAN*, A. and GUR, Y.

Leucocyte alkaline phosphatase: A marker for metastatic cancer.
*Harefuah* 124 (5), 270-273 (1993).

WAXMAN, E. and SHVARTS, D.

Second-type self-similar solutions to the strong explosion problem.
*Phys. Fluids A* 5 (4), 1035-1046 (1993).

WEAVER*, R.V., ZEIRI, Y. and UZER*, T.

Competition between adsorbate fragmentation and desorption on laser-heated surfaces.
*J. Chem. Phys.* 98 (6), 5059-5068 (1993).

WEISSMAN, Y.

Optical noise in a coherent LIDAR.
In: 8. Meeting on Optical Engineering in Israel: Optical Engineering and Remote Sensing (Tel-Aviv, Israel, 14-16 Dec. 1992).
*Proc. SPIE* 1971, 337-344 (1993).

WOLF, A., GILL*, R.L., BRENNER*, D.S., BERANT, Z., SCHUHMANN*, R.B. and ZAMFIR*, N.V.

g factor of the $\frac{3^+}{2}$ 93.6 keV level in $^{91}$Sr.

*Phys. Rev., C* 48 (2), 562-565 (1993).

WOLF, A., SCHOLTEN*, O. and CASTEN*, R.F.

F-spin purity of $2_1^+$ states in even-even nuclei.

*Phys. Lett., B* 312 (4), 372-376 (1993).

YASIN*, S., FRIEDMAN, M., GOSHEN, S., RABINOVITCH*, A. and THIEBERGER, R.

Intermittency and phase locking of the Bonhoeffer van der Pol model.

*J. Theor. Biol.* 160, 179-184 (1993).

ZAHAVI*, O., HAZAK, G. and ZINAMON*, Z.

Study of amplified spontaneous emission systems by the ray-tracing technique.

*J. Opt. Soc. Am., B: Opt. Phys.* 10 (2), 271-278 (1993).

## PAPERS PRESENTED AT CONFERENCES

**ANNUAL MEETING OF THE ISRAEL HEALTH PHYSICS SOCIETY ON RECENT ISSUES IN RADIATION PROTECTION, HERZLIYA, ISRAEL, 10 FEBRUARY 1993.**

BIRAN, T., SHAMAI, Y. and MALCHI, S.
[Personal monitoring of radiation workers in Israel - Update and innovation.] (Hebrew) pp. 42-52.

GOLD, B.
[Assessment of internal dose and treatment of internally contaminated persons by radioactivity.] (Hebrew) pp. 54-58.

LITAI, D. and SCHLESINGER, T.
[International basic safety standards for radiation protection.] (Hebrew) pp. 9-21.

SCHLESINGER, T. and LITAI, D.
[Radiation protection infrastructure in Israel - Draft regulations and development of codes of practice.] (Hebrew) pp. 22-41.

**ANNUAL MEETING OF THE ISRAEL CHEMICAL SOCIETY, 58TH, TEL-AVIV, ISRAEL, 17-18 FEBRUARY 1993. (PROGRAM AND ABSTRACTS).**

ABELL*, I.D., FREEDMAN*, F.A., HUTTON*, R.C., KINGSTON*, A., WALDER*, A.J. and PLATZNER, I.
Laser ablation inductively coupled plasma mass spectrometry. Ultra trace analysis with a high resolution ICP-MS and high accuracy isotope analysis with a double focusing ICP-MS. p. L-29.

COHEN, H. and MEYERSTEIN*, D.
Properties of transient complexes with copper-carbon $\sigma$ bonds in aqueous solutions. p. L-41.

HARTH, R., OZER, D., RAVEH, A. and BETTELHEIM, A.
Solid-state electrochemistry using ionically conductive polymers. p. L-91.

**ISRAEL MATERIALS ENGINEERING CONFERENCE, 6TH, IMEC VI, THE DEAD SEA, ISRAEL, 24-25 FEBRUARY 1993. (PROGRAM AND ABSTRACTS).**

ABRAMOV, E.
The effect of trapping and release process on thermonuclear fusion reactors performance. (Abstr. 2.2.2).

ABRAMOV, E., SOLOVIOFF*, G., GRINBERG, Y., LEMPERT, G.D. and ELIEZER*, D.
Hydrogen interaction with nickel pre-implanted with He: the effect of the dose and post-implantation annealing. (Abstr. P2.30).

ABRAMOV, E., YAKOBOVITCH*, N., BERMAN*, E. and ELIEZER*, D.
Simulation of hydrogen isotopes diffusion through metal lattice contains continuous energy traps. (Abstr. 3.1.1).

ADMON, U., DARIEL, M.P., KIMMEL, G., SARIEL, J., STECHMAN, A. and ZEVIN*, L.
Grain growth in copper-chromium multilayers. (Abstr. 1.4.4).

BRILL, M., SHMARIAU, D., ADLER, A., HARUSH, S. and ABRAMOV, E.
Preliminary study on microstructure of Al-Be alloys. (Abstr. P2.31).

DABUSH, A., DAYAN, D., KIMMEL, G., DAHAN, Y. and DARIEL, M.
Texture of uranium alloys due to plastic deformation. (Abstr. P2.34).

HERRMANN, B., MUNITZ, A., GUREVITZ, Y. and COTLER, C.
Corrosion of commercially pure aluminum type A5 1050 during long service at IRR2 reactor. (Abstr. P2.21).

KAHN*, A.H., PHILLIPS*, L.C. and STERN, A.
Electromagnetic monitoring of metal processing. (Abstr. C-2).

KOHN, G., SHNEOR*, Y. and PAPIAR*, R.
The effect of machining parameters on the surface roughness of Ni coated Al mirrors. (Abstr. P2.45).

LOTKER*, D., PELLEG*, J., FUKS*, D., GANOR, M. and YEHESKEL, O.
The influence of a third element on the interface reactions in metal matrix composites (MMC): Al-graphite system. (Abstr. 2.3.3).

MANORY*, R.R. and KIMMEL, G.
Structure of TiN nitrogen rich films. (Abstr. P2.2).

MORENO, D., ABRAMOV, E. and ELIEZER*, D.
A new mathematical approach based on the circular diaphragm to explain the blister effect on implanted metals. (Abstr. 2.2.4).

MORENO, D., ABRAMOV, E. and ELIEZER*, D.
Blisters formation due to helium implantation of copper and its alloys. (Abstr. P2.29).

MORENO, D. and ELIEZER*, D.
The source of fringe contrast observed in the interface between helium bubble and CuBe alloy matrix. (Abstr. P2.43).

MORENO, D. and ELIEZER*, D.
Hydrogen attack on copper and copper-beryllium alloy surface. (Abstr. P2.9).

MUNITZ, A., COTLER, C., NECHAMA, E. and TALIANKER*, M.
Growth of a metastable eutectic in Al-U alloys solidified in a copper mold. (Abstr. P2.24).

MUNITZ, A., COTLER, C., SACHAM, H. and ABERMAN, E.
Microstructure of TIG and electron beam copper-stainless steel welds. (Abstr. P2.23).

MUNITZ, A., SIMCA, F., STECHMAN, A., COTLER, C., TALIANKER*, M. and DAHAN, S.
Tensile properties of neutron irradiated cold-worked aluminum 6063 alloy. (Abstr. P2.22).

MUNITZ, A., ZENOU, V.Y., COTLER, C., ZAHAVI, A. and BARKAI, Z.
Microstructure of Al-U alloys solidified at cooling rates between 0.03-0.5 K/sec. (Abstr. 4.3.4).

NAWI, N., ITZHAK, D., ADMON, U. and DARIEL, M.S.
Study of chemical vapor infiltration process for SiC matrix composites. (Abstr. P1.30).

NIR, E., TUGENDHAFT, I., BORNSTEIN, A. and CROITORU*, N.
The influence of metallic geter on the oxygen impurity in As-Se infrared fiber. (Abstr. P2.35).

RAVEH, A., BETTELHEIM, A., KLEMBERG-SAPIEHA*, J.E., MARTINU*, L. and WERTHEIMER*, M.R.
The effect of frequency in plasma materials processing. (Abstr. P1.40).

RAVEH, A., MARTINU*, L., KLEMBERG-SAPIEHA*, J.E. and WERTHEIMER*, M.R.
Diamond-like carbon films: preparation, microstructure-property relationship. (Abstr. 2.3.4).

SOLOVIOFF*, G., ABRAMOV, E. and ELIEZER*, D.
Hydrogen induced blisters formation and growth in nickel pre-implanted with helium. (Abstr. P2.37).

SOLOVIOFF*, G., ABRAMOV, E., ELIEZER*, D. and LAVERNIA*, E.J.
Hydrogen effects in Al–$Al_3Ti$–SiC. (Abstr. P2.39).

STERN, A., DAHAN, I. and ELIEZER*, D.
Factors affecting the quality of electron beam (EB) welds of Al 1050 end caps to Al 6061 tubes. (Abstr. 1.3.5).

STERN, A., PHILIPS*, L. and CAHN*, A.H.
Electrical resistivity of 3104 Al-alloys. (Abstr. 1.3.1).

TEVET*, O., YEHESKEL, O., ATZMONY, U. and DARIEL, M.P.
In situ quality monitoring technique for a HIP process. (Abstr. P1.18).

VERED, R., NAHOR, G., LEMPERT, G.D., MAROM*, G. and LIFSHITZ, L.
Degradation of polymers by hyperthermal atomic oxygen. (Abstr. 1.1.4).

YEHESKEL, O.
The effect of impurities on the tensile elongation of beryllium. (Abstr. 4.2.1).

YEHESKEL, O., KLIMKER, H., GEFEN, Y. and GANOR, M.
Ultrasonics as a research tool in powder technology. (Abstr. 4.3.1).

ZALKIND, S., ASHKENAZY, R., HARUSH, S., VENKERT, A., MORENO, D., HALPERIN, D. and ABRAMOV, E.
Stress cracking as a result of hydride formation in U-0.1% Cr. (Abstr. P2.32).

**INTERNATIONAL SYMPOSIUM ON COST-BENEFIT ASPECTS OF FOOD IRRADIATION PROCESSING, AIX-EN-PROVENCE, FRANCE, 1-5 MARCH 1993.**

LAPIDOT, M., EISENBERG, E., PADOVA, R., ROSS, I. and KLINGER*, I.
Prevention of foodborne infections by use of ionizing radiation - Safety and economic aspects.

**INTERNATIONAL SEMINAR/WORKSHOP ON TEACHING AND EDUCATION IN FRACTURE AND FATIGUE, MISKOLC, HUNGARY, 12-13 MARCH 1993.**

KATZ, Y.
Changes beside continuation or evolutional approach to fracture/fatigue educational programs.

**THE ISRAEL PHYSICAL SOCIETY ANNUAL MEETING, TEL-AVIV, ISRAEL, 4 APRIL 1993. (PROGRAM AND ABSTRACTS). (*Bull. Isr. Phys. Soc.* 39, 1-150 (1993).)**

ARENSBURG, A. and WALD, S.
Plasma jet-liquid interaction in electrothermal launchers. p. 78.

BEN-AMAR, A., KAGAN, J., LANDO, M., MIRON, E., COHEN, A. and NAHMANI, M.
Efficient copper vapor laser pumped Ti:sapphire laser. p. 135.

BLAU, P.
Electromagnetic modeling of a coaxial, large-bore copper vapor laser. p. 146.

COHEN, A., BIDERMAN, S., DARIEL, M.P., HOROWITZ, A., NAHMANI, M., WEISS, M. and BEN-AMAR, A.
Growth and characterization of Ti:sapphire. p. 147.

CUPERMAN*, S., ZOLER*, D., ASHKENAZY, J., CANER, M. and KAPLAN, Z.
Consistent treatment of critical plasma flows in high pressure discharge ablative capillaries. p. 89.

DRAZNIN*, M., EICHEBAUM*, A., GOVER*, A., PINHASI*, Y., YAKOVER*, Y., SOKOLOWSKI*, J., MANDELBAUM*, B., ROSENBERG*, A., SHILOH*, Y., HAZAK, G., LEVINE, L.M. and SHAHAL, O.
Status report of the Israeli Tandem-FEL project. p. 148.

FINKENTHAL*, M. and ROSENBLUM, M.
SARIT: A possible Israeli magnetic confinement fusion project. p. 2.

KALISKY, Y. and SHIMONY, Y.
$Cr^{4+}$ solid state passive Q-switch for pulsed Nd:YAG laser. p. 142.

LOTEM, H.
Free spectral range in a diffraction-grating Littrow cavity. p. 145.

LOTEM, H. and DAGENAIS*, M.
High resolution mini-spectrograph. p. 144.

MITNIK*, D., MANDELBAUM*, P., SCHWOB*, J.L., BAR-SHALOM, A. and OREG, J.
Calculation of inner-shell 3d-4l excitation-autoionization effect on ion abundance balance in hot coronal plasmas. p. 97.

POMYALOV*, A.V., LAULICHT*, I. and BARAK, J.
Effect of thickness quantimization on subsidiary absorption spectra. p. 51.

WEISSMAN, Y.
Coherence effects in optical networks. p. 131.

**EUROPEAN UNION OF GEOSCIENCES CONFERENCE, 7TH, EUG VII, STRASBOURG, FRANCE, 4-8 APRIL 1993.**

STEINITZ*, G., VULKAN, U., LANG*, B., GILAT*, A. and ZAFRIR, H.
Temporal variation of radon flux along the northwestern corner of the Dead Sea, Dead Sea Rift.

**ANNUAL MEETING OF THE ASSOCIATION OF ISRAELI CHEMICAL ENGINEERS, 29TH, RAMAT AVIV, ISRAEL, 7-8 APRIL 1993.**

COHEN, H., DAVIDI*, S. and GROSSMAN*, S.L.

Emission of fire hazardous gases during low temperature oxidation of coal stored under atmospheric conditions.

GROSSMAN*, S.L., DAVIDI*, S. and COHEN, H.

Explosion risks in via evolution of molecular hydrogen as a result of bituminous coal storage in confined spaces.

GROSSMAN*, S.L., DAVIDI*, S. and COHEN, H.

Emission of toxic and fire hazardous gases from atmospheric stockpiled coal.

LUZZATTO*, E., COHEN, H. and MEYERSTEIN*, D.

Acetaldehyde as the product of reaction of the free radical $\cdot CH_2CH_2NH_3^+$ with Fe(II) complexes. An alternative mechanism for the formation of carbonyl groups in metal catalyzed oxidations of amines.

**MATERIALS RESEARCH SOCIETY SEMI-ANNUAL MEETING, SAN FRANCISCO, CALIFORNIA, USA, 12-16 APRIL 1993.**

SARIEL, J., CHEN*, H., JONGSTE*, J.F. and RADELAAR*, S.

Time resolved X-ray diffraction study of the transformation kinetics of $TiSi_2$–C49 in amorphous Si/Ti multilayers.

**AMERICAN NUCLEAR SOCIETY TOPICAL MEETING ON NUCLEAR PLANT INSTRUMENTATION, CONTROL AND MAN-MACHINE INTERFACE TECHNOLOGIES, OAK RIDGE, TENNESSEE, USA, 18-21 APRIL 1993.**

BOGER, Z.

Large scale neural networks - possible applications in nuclear power plants.

**JOURNEES DES ACTINIDES, 23EMES, SCHWARZWALD, GERMANY, 20-23 APRIL 1993. (PROGRAMME AND ABSTRACTS).**

KUZNIETZ, M., ANDRE*, G., BOURÉE*, F., PINTO, H., ETTEDGUI, H. and MELAMUD, M.

Neutron diffraction and AC-susceptibility studies of the magnetic phase diagram of the $U(Ni_{1-x}Cu_x)_2Si_2$ system. (Paper 06.1).

**SOCIETY OF VACUUM COATERS ANNUAL MEETING, 36TH, DALLAS, TEXAS, USA, 25-30 APRIL 1993.**

LEROUX*, P., RAVEH, A., KLEMBERG-SAPIEHA*, J.E. and MARTINU*, L.

Mechanical properties of plasma deposited functional coatings determined by microscratch measurements.

## Processes in Highly Porous Chars under Kinetically Controlled Conditions: I. Evolution of Pore Structure[1]

I. Kantorovich* and E. Bar-Ziv

We present a model that describes the evolution of the pore structure of highly porous chars during oxidation under kinetically controlled conditions. A random pore structure, representing the pores by finite volumes, is applied. Two types of pores were considered: macropores and micropores. Macropores were represented by empty cylinders with distributions of finite lengths and radii. The micropore structure is the result of a highly dense network of solid microcrystals which are represented by microrods of cylindrical shape. These microrods are of equal radius and with a distribution of lengths. Reaction was assumed to occur mainly in the joints of the microrods. Three mechanisms for the evolution of the pore structure were considered: (i) The network of the solid microrods remains unchanged during reaction except for changes in the dimensions of the microrods. The microrods are shortened due to break-restoration of the interrod joints. (ii) Continuous coalescence and replacement of all microrods during reaction. (iii) The subskeleton of large microrods does not change during reaction except for the change in dimensions of their links; however, coalescence takes place for small microrods. Using these models, expressions for the apparent density, microrod dimensions, total surface area, and porosity were developed. Comparison with available experimental data validated mechanism (iii). Shrinkage is explained by the continuous process of break and restoration of the internal joints of the subskeleton of large microrods.

*Reference*

[1] I. Kantorovich and E. Bar-Ziv, *Combust. Flame* (1994, in press).

## Processes in Highly Porous Chars under Kinetically Controlled Conditions: II. Pore Reactivity[1]

I. Kantorovich* and E. Bar-Ziv

Most of the existing models do not deal with the change in the intrinsic reactivity during the evolution of the pore structure. Reactivity is believed to be in the micropores and it was usually assumed that the density of active sites on the internal surface does not change with time, *i.e.*, the intrinsic reaction rate is independent of conversion. The objective of the present work was to model the reactivity of the porous medium and to show the mutual influence of

*Ben-Gurion University of the Negev, Beer-Sheva.

**INTERNATIONAL ASTRONOMICAL UNION (IAU) COLLOQUIUM 147, "EQUATION OF STATE IN ASTROPHYSICS", ST. MALO, FRANCE, 14-18 JUNE 1993.**

ROSENFELD, Y.

Onsager-molecule approach to screening potentials in strongly coupled plasmas.

**INTERNATIONAL PULSED POWER CONFERENCE, 9TH, ALBUQUERQUE, NEW MEXICO, USA, 21-23 JUNE 1993.**

KANTER, M., CERNY, R., SHAKED, N. and KAPLAN, Z.

Repetitive operation of an XRAM circuit.

**INTERNATIONAL ATOMIC ENERGY AGENCY TECHNICAL COMMITTEE MEETING ON RELIABILITY OF COMPUTERIZED SAFETY SYSTEMS, VIENNA, AUSTRIA, 21-25 JUNE 1993.**

CARMONA, S. and GREENBERG, R.

Functional independence in safety-critical software systems.

GREENBERG, R. and CARMONA, S.

A strategy for integrating software safety analysis within the system safety analysis.

RODNIZKI, J., GREENBERG, R. and BRAND, D.

Experience with "two version" programming.

**INTERNATIONAL MEETING ON ATOMIC AND NUCLEAR CLUSTERS, 20TH, SANTORINI, GREECE, 28 JUNE-2 JULY 1993.**

LAST, I. and GEORGE*, T.F.

Theoretical study of small $Ar_n^*$ clusters in low lying electronic states.

**AIAA THERMOPHYSICS CONFERENCE, 28TH, ORLANDO, FLORIDA, USA, 6-9 JULY 1993.**

GENKIN, L., BAER, M. and FALCOVITZ*, J.

Gasdynamic approach to small plumes computation.

**SPIE INTERNATIONAL SYMPOSIUM ON OPTICAL AND OPTOELECTRONIC APPLIED SCIENCE AND ENGINEERING, 38TH, SAN DIEGO, CALIFORNIA, USA, 11-16 JULY 1993.**

BOEHM, L., VAGISH, Z., FRISCHAT*, G.H. and BECKE*, A.

Tellurium based chalcogenide glass-ceramics for IR applications.

RABINOVITCH*, A., THIEBERGER, R. and FRIEDMAN, M.

Bonhoeffer-van der Pol oscillator under pulse-train forcing.

**LOS ALAMOS NATIONAL LABORATORY CRYOGENIC ENGINEERING CONFERENCE AND INTERNATIONAL CRYOGENIC MATERIALS CONFERENCE, ALBUQUERQUE, NEW MEXICO, USA, 12-16 JULY 1993.**

BUSSIBA, A. and KATZ, Y.

*On dislocation-crack tip model in cyclic Al-Li alloy.*

**ANNUAL INTERNATIONAL NUCLEAR AND SPACE RADIATION EFFECTS CONFERENCE, 30TH (NSREC'93), SHORT COURSE AND RADIATION EFFECTS DATA WORKSHOP, SNOWBIRD, UTAH, USA, 19-23 JULY 1993. (TECHNICAL PROGRAM AND ACTIVITIES).**

BARAK, J., LEVINSON, J., ZENTNER, A., DAVID, D., EVEN, O., HASS*, M., ILBERG, D. and LIFSHITZ, Y.

Study of single-event upsets in PAL16R8.

**AMERICAN SOCIETY OF MECHANICAL ENGINEERS PRESSURE VESSEL AND PIPING CONFERENCE, DENVER, COLORADO, USA, 25-29 JULY 1993.**

KATZ, Y.

Critical questions in searching for acceptable margins against failure.

**ANNUAL DENVER CONFERENCE ON APPLICATIONS OF X-RAY ANALYSIS, 42ND, DENVER, COLORADO, USA, 2-6 AUGUST 1993.**

KIMMEL, G., POLITI, L. and WIEDER*, T.

Characterization of (Ti,Al)N film by XRD and XRF.

**AMERICAN ASSOCIATION FOR CRYSTAL GROWTH ANNUAL MEETING, BALTIMORE, MARYLAND, USA, 5-9 AUGUST 1993.**

AZOULAY, M., SINVANI, M., MIZRACHI, M. and FELDSTEIN, H.

Stripe structure of CdTe-CdZnTe-CdTe in a bulk single crystal.

GEORGE*, M.A., AZOULAY, M., JAYATIRTHA*, H.N., BIAO*, Y., BURGER*, A. and SILBERMAN*, E.

Atomic force microscopy of lead iodide crystal surfaces.

**INTERNATIONAL WORKSHOP ON ION MOBILITY SPECTROMETRY, 2ND, QUEBEC CITY, QUEBEC, CANADA, 15-18 AUGUST 1993.**

EICEMAN*, G.A. and KARPAS, Z.

Towards standard reduced mobility measurements.

KARPAS, Z., EICEMAN*, G.A., WALSH*, M., WANG*, Y.F. and BELL*, E.

Ion structure from ion mobility measurements.

**INTERNATIONAL SYMPOSIUM ON PLASMA CHEMISTRY, 11TH (ISPC 11), LOUGHBOROUGH, ENGLAND, 22-27 AUGUST 1993.**

REINKE*, P., RAVEH, A., KLEMBERG-SAPIEHA*, J.E. and MARTINU*, L.

Modification of interfaces in the growth of diamond by MW/RF plasma.

**INTERNATIONAL BOTANICAL CONGRESS, 15TH, YOKOHAMA, JAPAN, 28 AUGUST - 3 SEPTEMBER 1993.**

DEGANI, N. and PLATZNER, I.

Fractionation of stable calcium isotopes in tissues of acacia (*Acacia retinodes*).

**AMERICAN NUCLEAR SOCIETY TOPICAL MEETING ON ENVIRONMENTAL TRANSPORT AND DOSIMETRY, CHARLESTON, SOUTH CAROLINA, USA, 31 AUGUST - 3 SEPTEMBER 1993.**

PERNICK, A. and ZAFRIR, H.

Applications of collimated airborne monitoring in radiological emergency response.

**RARE EARTH RESEARCH CONFERENCE, 20TH, MONTEREY, CALIFORNIA, USA, 12-17 SEPTEMBER 1993. (PROGRAM AND ABSTRACTS).**

KUZNIETZ, M., PINTO, H., ETTEDGUI, H. and MELAMUD, M.

Neutron diffraction study of the magnetic structure of $(U_{0.5}Tb_{0.5})Co_2Ge_2$. (Paper P.V.5). p. 52.

KUZNIETZ, M., PINTO, H. and MELAMUD, M.

Comparison of magnetic ordering properties of the $RM_2X_2$ and $UM_2X_2$ compounds. (Paper P.V.6), p. 53.

**EUROPEAN CONFERENCE ON RADIATIONS AND THEIR EFFECTS ON COMPONENTS AND SYSTEMS, 2ND (RADECS 93), ST. MALO, FRANCE, 13-16 SEPTEMBER 1993. (ABSTRACTS).**

LEVINSON, J., EVEN, O., ADLER, E., HASS*, M., ILBERG, D. and LIFSHITZ, Y.

Single event latchup (SEL) in IDT 7187 SRAMs - Dependence on ion penetration depth. (Abstr. PF-1).

**INTERNATIONAL CONFERENCE ACTINIDES-93, SANTA FE, NEW MEXICO, USA, 19-24 SEPTEMBER 1993. (FINAL PROGRAM AND ABSTRACTS).**

KUZNIETZ, M., ANDRE*, G., BOURÉE*, F., PINTO, H., ETTEDGUI, H. and MELAMUD, M.

Neutron diffraction and AC-susceptibility studies of the $U(Ni_{1-x}Cu_x)_2Si_2$ system. (Paper P-74).

KUZNIETZ, M., PINTO, H. and MELAMUD, M.

Magnetic phase diagrams of the $U(M,M')_2X_2$ systems (M,M'=Co,Ni,Cu;X=Si,Ge). (Paper P-154).

**EUROPEAN CONFERENCE ON DIAMOND, DIAMOND-LIKE AND RELATED MATERIALS, 4TH (DIAMOND FILMS'93), ALBUFEIRA, ALGARVE, PORTUGAL, 20-24 SEPTEMBER 1993. (ABSTRACTS)**

LIFSHITZ, Y., LEMPERT, G.D., ROTTER, S., AVIGAL*, I., UZAN-SAGUY*, C., KALISH*, R., KULIK*, J., MARTON*, D. and RABALAIS*, J.W.

The effect of ion energy on the diamondlike/graphitic ($SP^3/SP^2$) nature of carbon films deposited by ion beams. (Abstr. 9.054).

**CONFERENCE ON APPLICATIONS OF SURFACE AND INTERFACE ANALYSIS, 5TH (ECASIA 93), CATANIA, SICILY, ITALY, 4-8 OCTOBER 1993. (ABSTRACTS).**

VERED, R., MATLIS, S., NAHOR, G., LEMPERT, G.D., GROSSMAN, E., MAROM*, G. and LIFSHITZ, Y.

Degradation of polymers by hyperthermal atomic oxygen. (Abstr. RA-14).

**INTERNATIONAL SUMMER SCHOOL AND WORKSHOP ON NUCLEAR FUSION AND PLASMA PHYSICS, HEFEI, CHINA, 4-17 OCTOBER 1993. (ABSTRACTS).**

WERDIGER, M., MOSHE, E., ARAD, B., GAZIT, Y., ELIEZER, S. and MAMAN, S.

2 dimensional effects of laser induced shock waves in aluminium. (Abstr. B-8).

**EXPERIMENTAL CHAOS CONFERENCE, 2ND, ARLINGTON, VIRGINIA, USA, 6-8 OCTOBER 1993.**

THIEBERGER, R., FRIEDMAN, M. and RABINOVITCH*, A.

Simple model of excitable systems.

**INTERNATIONAL ATOMIC ENERGY AGENCY SPECIALISTS' MEETING/WORKSHOP ON "DEMONSTRATION AND REVIEW OF EXPERT SYSTEM PROTOTYPES USED IN THE NUCLEAR INDUSTRY", TEL-AVIV, ISRAEL, 11-15 OCTOBER 1993.**

BEN-HAIM, M.

Corrosion knowledge acquisition by neural network modeling.

BOGER, Z.

The status of artificial neural networks applications in the nuclear industry.

**INTERNATIONAL UNION OF THEORETICAL AND APPLIED MECHANICS (IUTAM) SYMPOSIUM ON IMPACT DYNAMICS, BEIJING, CHINA, 11-15 OCTOBER 1993. (PROGRAM AND ABSTRACTS).**

GILATH, I. and ELIEZER, S.

Impulsive loading of materials using laser induced shock waves. pp. 55-56.

**THE ISRAELI METALLURGICAL SOCIETY CONGRESS ON ADVANCED TECHNOLOGIES IN WELDING AND NONDESTRUCTIVE EXAMINATION, KIBBUTZ SHFAIM, ISRAEL, 18-19 OCTOBER 1993. (PROGRAM AND ABSTRACTS).**

ADDESS, S. and MAGAL, O.

[Evaluation of a crack in a pressure vessel and its repair by welding.] (in Hebrew). (poster). p. 38.

BENAIM, P., ELIEZER*, D., ABRAMOV, E., DAHAN, I. and STERN, A.

Weld characterization of new metastable beta-21S titanium alloy. pp. 41-42.

DAHAN, I., ELIEZER*, D. and STERN, A.

Electron beam welding aluminium 1050 to 6061. p. 31.

STERN, A., MAGAL, O., DAHAN, Y., ZILBER, T. and SHILOH, K.

[Characterization of defects in aluminum 1050 joints welded by the GTAW process.] (in Hebrew). (poster). p. 40.

**1993 U.S. WORKSHOP ON THE PHYSICS AND CHEMISTRY OF MERCURY CADMIUM TELLURIDE AND OTHER IR MATERIALS, SEATTLE, WASHINGTON, USA, 19-21 OCTOBER 1993. (EXTENDED ABSTRACTS).**

ARIEL*, V., GARBER*, V., BAHIR*, G., SHER, A. and CINADER, G.

Investigation of P-p CdTe/HgCdTe heterojunctions by capacitance - voltage profiling.

**INTERNATIONAL WORKSHOP ON LASER INTERACTION AND RELATED PLASMA PHENOMENA, 11TH, MONTEREY, CALIFORNIA, USA, 25-29 OCTOBER 1993.**

ELIEZER, S., HENIS, Z. and PAISS, Y.

Phase transitions in subnanosecond laser induced shock waves.

ELIEZER, S., KOLKA, E. and PAISS, Y.

Confinement of plasma in a magnetic bottle induced by circularly polarized laser light.

WERDIGER, M., ARAD, B., GAZIT, Y., ELIEZER, S., MOSHE, E. and MAMAN, S.

2 dimensional effects of laser induced shockwaves in aluminum.

**INTERNATIONAL THERMAL CONDUCTIVITY CONFERENCE, 22ND, TEMPE, ARIZONA, USA, 7-10 NOVEMBER 1993.**

SHAI*, I. and HAIM, M.

High thermal conductivity measurement using the internal heat source method.

**LDEF POST-RETRIEVAL SYMPOSIUM, 3RD, WILLIAMSBURG, VIRGINIA, USA, 8-12 NOVEMBER 1993.**

SIMON*, C.G., BUONAQUISTI*, A.J., BATCHELOR*, D.A., HUNTER*, J.L., GRIFFIS*, D.P., MISRA*, V., RICKS*, D.R., WORTMAN*, J.J., BROWNLEE*, D.E., BEST*, S.R., CRUMPLER*, M.S., ARAD, B., ELIEZER, S., MOSHE, E., MAMAN, S. and GILATH, I.

Secondary ion mass spectrometry analysis of hypervelocity micro-particle impact sites on LDEF surfaces.

**INTERNATIONAL SOCIETY FOR LASER SURGERY AND MEDICINE CONGRESS, 10TH, AND INTERNATIONAL YAG LASER SYMPOSIUM, 7TH, BANGKOK, THAILAND, 12-17 NOVEMBER 1993. (PRELIMINARY PROGRAM).**

GABAY, S.

New optical technique for corneal refractive surgery.

**CONFERENCE ON MAGNETISM AND MAGNETIC MATERIALS, 38TH, MINNEAPOLIS, MINNESOTA, USA, 15-18 NOVEMBER 1993. (ABSTRACTS).**

KUZNIETZ, M., PINTO, H. and MELAMUD, M.

Magnetic ordering in $UCoNiSi_2$ and $UCoCuSi_2$, studied by AC-susceptibility and neutron diffraction measurements. (Paper HQ-15).

**1993 ANNUAL CONFERENCE OF THE ISRAELI ASSOCIATION FOR CRYSTAL GROWTH, REHOVOT, ISRAEL, 16 NOVEMBER 1993. (PROGRAM AND ABSTRACTS).**

AZOULAY, M., GEORGE*, M.A. and BURGER*, A.

A study of the morphology of single crystalline surfaces by means of atomic force microscopy. p. 32.

FELDSTEIN, H.

Growth and characterization of CdTe and CdZnTe crystals. p. 5.

KIMMEL, G., SARIEL, J., DAHAN, I., NATHAN, S. and SARUSI, B.

Derivation of accurate unit cell parameters in powder diffraction in multiphase systems. p. 34.

YEHESKEL, O., LEVI, M., KALIR, D., VENKART, A., BEN-AMAR, G., GOLDSTEIN*, A. and FISHER*, R.

Transparent $Y_2O_3$ produced by powder technology route. p. 17.

**INTERNATIONAL ATOMIC ENERGY AGENCY INTERREGIONAL SEMINAR ON RESEARCH REACTOR CENTRES - FUTURE PROSPECTS, BUDAPEST, HUNGARY, 22-26 NOVEMBER 1993.**

NAGLER, A., HIRSHFELD, H. and DAGAN, R.

Fuelless hosts of control rods in a swimming pool reactor.

# X

# AUTHOR INDEX

# Author Index


Abramov, E. 73,78,80
Achiam, Y. 9,10
Admon, U. 87,88
Aharoni, D. 127
Akkerman, A. 71,72,123,125
Algom, A. 104
Alimi, R. 147-149
Alurralde, M. 71
Andre, G. 54,55,57
Anholt, M. 69
Ankry, N. 126,127,129
Arad, B. 23,26
Arad, M. 118,161
Aragones, J.M. 21
Ariel, V. 47
Assido, H. 131,133-135,139
Avida, R. 103,104
Avigal, I. 68
Azoulay, M. 47-51

Baer, M. 3-7
Bahar, J. 116
Bahir, G. 47
Bar-Noy, T. 25
Bar-Sagi, J. 29
Bar-Shalom, A. 32
Bar-Ziv, E. 93-95
Barak, D. 155,158
Barak, J. 123,125
Baram, A. 3-5,7
Baran, A. 145
Baruch, M. 81
Basiev, T.T. 51
Bass, M. 30
Bass, M.A. 51
Batchelor, D.A. 23
Baum, D. 94
Beeri, O. 88
Bell, S.E. 102
Ben-Amo.. A. 35,86
Ben-Kish, A. 27,28
Ben-Shachar, B. 125
Berant, Z. 62
Bertrand, L. 85
Best, S.R. 23
Bettelheim, A. 100,101,150
Biao, Y. 48,50
Biderman, S. 86
Blau, P. 36,42
Boehm, L. 30
Boger, Z. 151
Boneh, R. 158
Bornstein, A. 26
Bourdon, E.B.D. 83
Bouree, F. 52,54.55,57
Boutard, D. 84
Boyd, K. 67
Brand, D. 125
Brenner, D.S. 62
Breskin, A. 71
Broitman, F. 101
Brownlee, D.E. 23
Buonaquisti, A.J. 23
Burger, A. 48,49,50,51
Burshtein, Z. 31,32
Burstein, O. 130

Canfi, A. 119
Carmona, S. 160
Casten, R.F. 62,63
Chai, B.H.T. 30,51
Chechik, R. 71
Chouraqui, P. 116
Cinader, G. 47

Cohen, A. 35,86,155
Cohen, H. 96-99,112-114
Cohen, N. 154
Collins, W.E. 48,49,51
Crumpler, M.S. 23
Czapski, G. 97-99

Dagenais, M. 38,39
Dahan, I. 87,88
Dariel, M.P. 86,87
Dariel, M.S. 100
David, D. 123,125
David, R 32
Davidi, S. 112-114
Dayan, D. 88
Deka, C. 30,51
Dolev, Y. 154
Domingue, A. 85
Doron, E. 115
Doroshenko, M.E. 51
Duvniz, E. 128,129,133

Eckstein, W. 67
Eger, D. 17,19
Eiceman, G.A. 102-105
Eisenberg, E. 6,116
Elbaz, Y. 141
Eldan, M. 114
Eldik, R. van 96,97,99
Elgad, D. 127
Eliezer, D. 73,74,77,78,80
Eliezer, S. 19-26
Ellenbogen, M. 128,129,133
Ettedgui, H. 53-55,57
Even, O. 123
Ewing, R.G. 104

Falcovitz, J. 3
Falquina, R. 20
Faraggi, M. 101
Fein, A. 29,106
Feldman, B. 151
Feldstein, H. 47
Fraenkel, M. 22
Freud, A. 119
Friedman, M. 8,9,103,104
Friedman, Y. 26
Friemark, D. 116

Gabay, S. 42,43
Gabay, Y. 159
Gabovitch, A. 153,155,158
Gaede, W. 96,97,99
Gal, G. 93
Garber, V. 47
Gayer, A. 145
Gazit, Y. 26
Genkin, L. 3
George, M.A. 48-51
Gerhard, A. 96,99
German, U. 136-139,141
Gibrekhterman, A. 71,123
Gilath, I. 23-25
Gilibert, M. 3,5,6
Gill, R.L. 62
Goldberg, J. 153
Goldstein, S. 97-99
Goresnic, C. 145
Green, F. 22
Greenberg, R. 159,160
Greenberg, S. 150-154
Grest, G.S. 70
Griffis, D.P. 23
Grossman, E. 69
Grossman, S.L. 112-114
Guetta, V. 116
Gujrathi, S.C. 83
Gur, Y. 118
Guterman, H. 150,151

Harden, C.S. 103,104
Hareuveni, R. 147
Harris, I.R. 75
Harth, R. 101
Harush, Y. 131
Hass, M. 71,123
Hayon, J. 100,101,150
Hazak, G. 13,14,32
Henderson, D.O. 31
Henis, Z. 22
Henneck, R. 71
Herman, R. 26
Herrmann, B. 88
Hirnak, S. 51
Hitterman, R.L. 59
Hollander, M. 118,161
Honrubia, J.J. 21
Hora, H. 21,22
Horowitz, A. 86
Horowitz, Y.S. 125
Houle, S. 84
Hunter, B.A. 59
Hunter, J.L. 23

Ilberg, D. 71,72,123,125
Israeli, B. 152
Israeli, M. 123
Iszak, E. 145
Ivry, J. 32
Izumi, F. 59

Jackel, S. 29
Jaeger, Z. 69
Jayatirtha, H.N. 48,50,51
Jorgensen, J.D. 59
Joswig, M. 109

Kagan, J. 35
Kahane, S. 59,60
Kalish, R. 68
Kalisky, Y. 35
Kamiyama, T. 59
Kantorovich, I. 95
Karpas, Z. 102-105,151
Karpinovitz, T. 147
Katz, A. 155
Katz, M. 17,19
Katz, Y. 87
Kimmel, G. 87-89
Kinoshita, K. 59
Klapper, M.H. 101
Klemberg-Sapieha, J.E. 85
Knol, R. 152
Kochavi, E. 156,158
Kol, R. 136
Kolka, E. 19,22
Kornfeld, H. 159
Kotler, Z. 29,106
Kulik, J. 67,68
Küttel, O.M. 85
Kuznietz, M. 52-55,57

Laichter, Y. 137
Landau, A. 88
Lando, M. 35
Lashmore, D.S. 87
Last, I. 3-5,7
Lavernia, E.J. 80
Lawrence, J.R. 114
Lempert, G.D. 67-69,79
Leonard, G. 109
Levin, L.A. 32
Levinson, J. 70-72,123,125
Levinson, S. 136-139.141
Levron, D. 32
Levy, I. 31
Liepmann, M.J. 30
Lifshitz, Y. 67-69,71,72,123,125
Livne, Z. 88
Loesch, H.J. 4

Lotem, H. 36,38,39
Loutts, G.B. 51
Lowry, S. 26

Maiss, E. 129
Maman, S. 23,26
Marom, G. 69
Martinez-Val, J.M. 21
Martinu, L. 83-85
Marton, D. 67,68
Matlis, S. 69
Matmor, A. 103,104,126
Mayer, A.H. 69
Mayo, N. 150
Mazor, T. 127-129,131
Melamud, M. 52-55,57,61
Melnik, D. 147
Meyerstein, D. 96-99
Milshtein, S. 118,161
Minguez, E. 20,21
Miron, E. 35
Misra, V. 23
Mizrachi, D. 109
Mizrachi, M. 47
Moreh, R. 60,61
Moreno, D. 73-75,77-79
Morgan, S. 31
Moshe, E. 23,26
Mu, R. 31
Murat, M. 70

Nahmani, M. 35,86
Nahor, G. 69
Naim, E. 136-138,141
Nason, D. 48,50
Nathan, S. 88
Newman, R. 112,115
Nir, E. 26
Nir El, Y. 146,147
Noter, Y. 123,125

Onn, U. 149
Oreg, J. 32
Oren, J. 118,161
Oron, M. 17,19
Ozer, D. 100,101,150

Paiss, Y. 19,20
Pan, Z. 38,39
Paran, J. 135,159
Peled, A. 26
Pelled, O. 136,138
Perelmutter, L. 147
Perlado, J.M. 21
Pernick, A. 110
Piera, M. 21
Piestun, S. 134,139
Pinto, H. 52-55,57,61
Poitras, D. 84
Polak, E. 145
Politi, L. 89

Rabalais, J.W. 67,68
Rabinovitch, A. 8,9
Rabinovitch, K. 36
Rapaport, M.S. 145
Raveh, A. 83-85,150
Ricks, D.R. 23
Rishpon, J. 100
Ron, S. 6
Ronen, Y. 135
Rosenfeld, Y. 7,8
Rosenwaks, S. 42
Roter, T. 70
Rotman, I. 152
Rotter, S. 68
Roux, C.D. 67
Rubinfeld, S. 116

Saphier, D. 149
Sariel, J. 87,88

Sarousi, B. 154
Scholten, O. 63
Schuhmann, R.B. 62
Segev, R. 158
Shafir, E. 27,28
Shahal, O. 103,104
Shaier, P. 29,106
Shaik, S. 98
Shaked, H. 59,61
Shaked, N. 27,28
Shamai, Y. 123
Shappir, J. 70
Sharon, R. 150
Shemesh, Y. 131,133,134,139
Sher, A. 47
Shimon, O. 136
Shimony, Y. 30,31,35,51
Shmuely, M. 135
Shtechman, A. 87
Shuster, A. 131
Sigachev, V.B. 51
Silberman, E. 31,48-51
Simon, C.G. 23
Singer, L. 123
Sinvani, M. 47
Skibin, D. 109,112,115
Smilanski, I. 42
Sokolov, K. 112
Solovioff, G. 78,80
Somer, Z. 109
Sonzogni, W.C. 114
Southern, B.W. 9,10
Stotland, A. 116
Strauss, H. 20
Strauss, M. 32
Szichman, H. 5,7,22

Tal, N. 126,127
Taragan, E. 11
Thieberger, R. 8,9
Tirosh, D. 128,130,134,135,159
Trent, J.B. 101
Tugendhaft, I. 26
Tur, M. 27,28
Tzabarim, M. 145

Uzan Saguy, C. 68

Vagish, Z. 30
Velarde, G. 21
Velarde, P. 21
Vella, N. 84
Vered, R. 69
Vered, Z. 151
Victoria, M. 71
Villaverde, A.B. 51
Vulaski, E. 126-129

Walach, N. 118
Wald, S. 147
Walsh, M. 102
Wang, Y. F. 102,105
Weininger, J. 116
Weinstein, M. 136,138
Weiss, M. 86
Weiss, Y. 94
Weissman, Y. 26
Wengrowicz, U. 128-130,134
Werdiger, M. 26
Werner, H.J. 4
Wertheimer, M.R. 84,85
Wieder, T. 89
Wolf, A. 62,63
Wortman, J.J. 23

Yahav, B. 87
Yarimi, Y. 26
Ydgar, R. 101,150
Yeheskel, J. 100
Yomdin, Y. 158
Yossian, D. 125

Zafrir, H. 110
Zahavi, A. 88
Zahavi, O. 13
Zalkind, S. 79
Zamfir, N.V. 62
Zamir, R. 11,14
Zeiri, Y. 12
Zentner, A. 123,125
Zevin, L. 87
Zhang, X.X. 51
Zigler, A. 22
Zilcha, R. 150
Zinamon, Z. 13
Zinger, B. 29,106
Zoler, D. 148,149
Zussman, A. 17,19

IA - 1486

Israel Atomic Energy Commission
**RESEARCH LABORATORIES ANNUAL REPORT, 1993**
Jule 1994 206 p.

**This report presents brief summaries of the research carried out at the Israel A.E.C. Laboratories during 1993.**

IA - 1486

Israel Atomic Energy Commission
**RESEARCH LABORATORIES ANNUAL REPORT, 1993**
Jule 1994 206 p.

**This report presents brief summaries of the research carried out at the Israel A.E.C. Laboratories during 1993.**

IA - 1486

Israel Atomic Energy Commission
**RESEARCH LABORATORIES ANNUAL REPORT, 1993**
Jule 1994 206 p.

**This report presents brief summaries of the research carried out at the Israel A.E.C. Laboratories during 1993.**